Università della Calabria

DIPARTIMENTO DI FISICA

Scuola di Dottorato "Archimede"

Curriculum in Fisica e Tecnologie Quantistiche

Ciclo XXV

Tesi di Dottorato

Electronic Excitations of Graphene, Graphene Nickel interfaces, and Carbon Nanotubes

SSD: FIS/03 – Fisica Della Materia

Candidato: Michele Pisarra

SUPERVISORI

Dr. Pierfrancesco Riccardi

Dr. Antonello Sindona

COORDINATORE

Prof. Roberto Fiore

Dicembre 2012

Contents

Chapter 1

Introduction

In the fascinating picture of science, viewed as a constant fight to push forwards the limits of the human knowledge, with a preferred direction singled out by technological applications, whose final goal is to improve human life, our small contribution, subject of this thesis, deals with the analysis of properties related to excitations of carbon based nanostructured materials.

The choice of carbon based materials is justified because in the last decades they are raising as promising materials with a wide range of technological applications, ranging from electronics, where carbon is supposed to replace silicon, to medicine and biology, where carbon represents one of the fundamental building blocks of organic compounds. Actually, carbon based nanostructured materials are usually referred to as strong correlated systems, owing this definition to their particular electronic properties determined by the valence electrons, that are involved in complicated many body excitations. In this work, we analyze in particular the electronic excitation properties of Graphene, both freestanding and adsorbed on metal surfaces, and carbon nanotubes.

This introductory chapter briefly reviews the prominent features of Graphene and carbon nanotubes, postponing a proper introduction, presentation and discussion of results to the following chapters. Throughout the entire work we use atomic units[1], unless otherwise stated. SI units will be occasionally used to improve the readability of data and results. The organization of the entire work is as follows.

Firstly, in chapter 2 we shortly review the Density Functional Theory (DFT) [1, 2], that is not the main topic of this work, but is used as a working tool throughout all the

[1]electron mass $m_e = 1$; reduced Plank constant $\hbar = 1$ elementary charge $e = 1$, Bohr radius $a_0 = 1$.

thesis. We start with the theory based on the Hoenberg-Kohn theorems and give a sketch of how the theory is translated to an application algorithm, the Kohn-Sham procedure. Then, we review the approximation involved in solving a DFT problem, with particular attention on the ones used for our purposes.

In chapter 3 we study the Auger electron emission from single walled carbon nanotubes. We develop a theory for Auger electron emission, based on perturbation theory and the Fermi golden rule (FGR). Then we study the Auger emission lineshape of a $(10, 10)$ single walled carbon nanotube, using as starting points two DFT calculations with different characteristics, namely an all electron calculation on a finite size tube and a pseudopotential calculation on a periodic tube [3]. We include also initial and final state effects to understand the role played by such corrections, that lie outside the FGR approach, in deforming the emission line that is compared to experimentally measured Auger emission data from nanotube bundles [4].

In chapter 4 we analyze the Graphene system adsorbed on a Nickel (111) surface. We present experimental measurements of secondary electron emission [5, 6, 7, 8]. The adsorption of the Graphene layer induces significant modifications on the secondary emission properties of the Nickel surface, reflected, both on the total emission yield and on the emission lineshape. We find the latter to be modified by a series of peaks, showing a remarkable dispersion that we ascribe to the particular density of unoccupied states of the system. We try to analyze the nature of these peaks using a simple approach based on a DFT band structure calculation of Graphene adsorbed on (111)-oriented Nickel slabs of different thicknesses. To validate the approach, we apply first the technique to the case of Graphite, using secondary electron emission data taken from literature [9, 10, 11].

In chapter 5, we study the electron energy loss function of Graphene and Graphene adsorbed on Nickel (111) surfaces. We firstly introduce the physical problem and review how the energy loss function can be calculated, using as starting point a ground state DFT calculation. Then we calculate the energy loss function for freestanding Graphene. We analyze also how the charge carrier density variation modifies the loss function of freestanding Graphene. Then, we calculate the loss function for Graphene adsorbed on a Nickel surface, representing a system characterized by strong interactions between Graphene and the substrate, and compare the result with some experimental measurements.

1.1 Graphene

Graphene is a two-dimensional (2D) honeycomb arrangement of Carbon atoms. It has been widely studied since 60 years for different reasons, even though it was believed that a pure two-dimensional material was impossible to synthesize. At the beginning it was considered an ideal 2D material so it was studied for purely "academic" purposes. Then, its particular electronic structure was studied and applied to study the properties of Graphite, that is a vertical stacking of Graphene sheets with small interlayer interactions. In its adsorbed form on surfaces, Graphene was originally called Monolayer Graphite and it was studied for its low chemical reactivity. The concept of Graphene is also found in studies of low dimensional carbon allotropes, like fullerenes and in particular C60 (discovered in 1985) that is a Graphene sheet projected onto a sphere, resulting from the electronic point of view in a 0-dimensional material, or carbon nanotubes (discovered in 1991) that are obtained by rolling up a Graphene sheet to form a cylinder, which can be interpreted as 1-dimensional materials. Graphene received renewed interest in the lastest years, after its discovery as a freestanding material in 2004, by A. Geim and K. Novoselov [12] who also started to study its electronic properties. Since then, several singular properties and behaviors have been understood leading to a broad field of possible applications, ranging from electronics to medicine and passing trough chemistry and theoretical physics, where the most outstanding and fascinating application concerns the peculiar band structure of Graphene used to test the Dirac theory of the relativistic electron.

As anticipated above, Graphene is a two-dimensional arrangement of carbon atoms. Its structure is formed by two interpenetrated hexagonal carbon sublattices, or by an hexagonal lattice with a basis of two carbon atoms. In figure 1.1, we show the honeycomb lattice, obtained as the "superposition" of the two inequivalent sublattices **A** and **B**; the distance between nearest neighbor carbon atoms is $a = 1.42$ Å; $\mathbf{a}_1$ and $\mathbf{a}_2$ are the translation vectors and the two sublattices are connected by one of the δ vectors. In figure 1.2**A**, we show the unit cell of Graphene, used in our work, and in figure 1.2**B**, the corresponding first Brillouin Zone (BZ) with reciprocal lattice vectors $\mathbf{b}_1$ and $\mathbf{b}_2$ and high symmetry points $\mathbf{\Gamma}$, **K** and **M**; the yellow path is usually considered in band structure plots, and encloses the irreducible high symmetry zone.

Most of the peculiar properties of Graphene are connected with its band structure [13]. In our work, we are concerned with electronic properties so we will stress mostly this point. In particular, with a simple Tight Binding approach [14], it is possible to determine one of

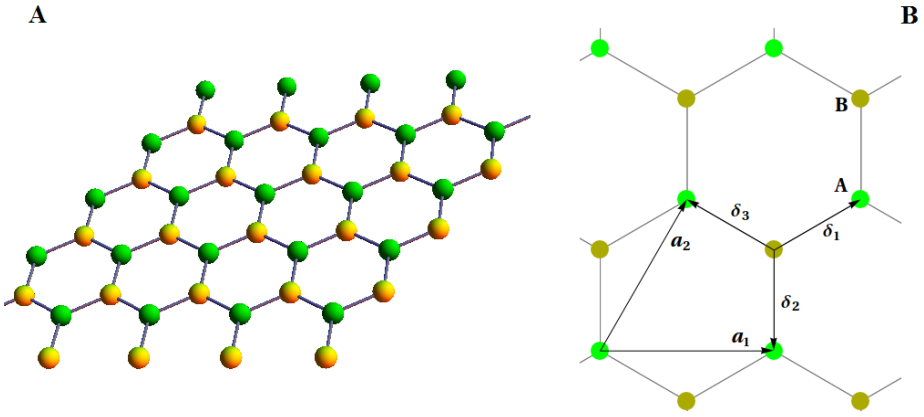

Figure 1.1: Honeycomb Graphene lattice obtained as sum of two triangular sublattices.
A: Tri-dimensional view;
B: The two sublattices in detail; $\mathbf{a}_1$ and $\mathbf{a}_2$ are the primitive translation vectors, δ_1, δ_2, or δ_3 allow to go from the sublattice **A** to the sublattice **B**.

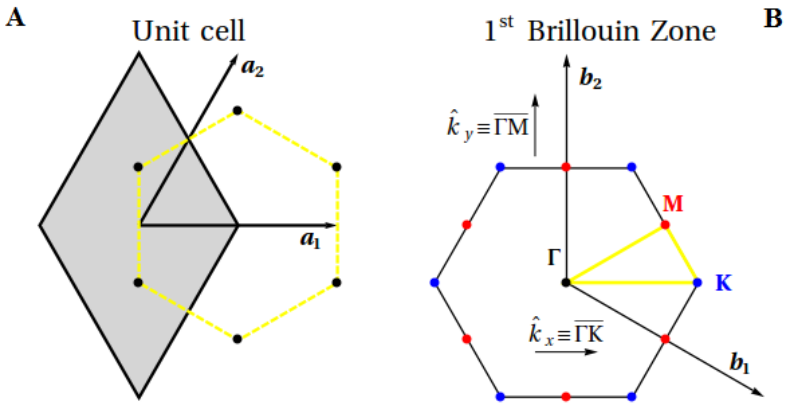

Figure 1.2: Unit cells:
A: Two possible choices of the unit cell for the Graphene lattice, each with two atoms.
B: Reciprocal lattice primitive vectors $\mathbf{b}_1$ and $\mathbf{b}_2$ corresponding to the direct lattice vectors of panel **A**, and the 1st BZ, with the high symmetry points **Γ**, **K** and **M**, singled out as black, blue and red points, respectively; the yellow line draws the path along which the band structure is usually plotted, it also encloses the irreducible part of the BZ, i. e. the part of the BZ that can be used to reproduce the full BZ with symmetry operations.
Useful quantities: $|\mathbf{a}_1| = |\mathbf{a}_2| = 2.46$ Å; $|\mathbf{b}_1| = |\mathbf{b}_2| \approx 2.95$ Å^{-1}; $\overline{\mathbf{\Gamma K}} \approx 1.71$ Å^{-1}; $\overline{\mathbf{\Gamma M}} \approx 1.47$ Å^{-1}.

the peculiar properties of Graphene represented by the π and π^* bands, that are the last occupied and the first unoccupied bands. The Graphene π bands are shown in figure 1.3; the two bands touch at a single point, in correspondence of the six **K** high symmetry

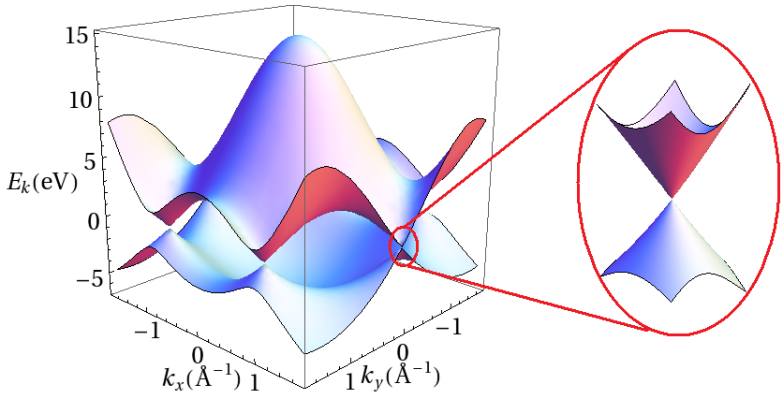

Figure 1.3: π and π^* Graphene bands obtained with a tight binding calculation [14]; the magnification show the band dispersion around the **K** point and the Dirac cone.

points of the BZ, see figure 1.2**B**. This point is called Dirac point because, as shown in the magnification of figure 1.3, the band dispersion around this point is represented by a cone, so that the electron quasi-momentum may be written $\mathbf{k} = \mathbf{K} + \mathbf{q}$, and the band dispersion is approximated by:

$$E(\mathbf{q}) \approx \pm v_F |\mathbf{q}| \qquad \text{for} \qquad |\mathbf{q}| \ll |\mathbf{K}|. \tag{1.1}$$

This is the same energy dispersion for the Dirac electron in relativistic quantum physics, with v_F the Fermi velocity that is roughly 1/200 the speed of light. The Fermi energy passes through the Dirac point and the density of states is zero at the Fermi energy, so that Graphene can be classified as a 0-gap semiconductor. The relation (1.1) gives to Graphene several interesting electronic properties, connected to electric conduction and electronic excitations, that we are going to investigate throughout this work.

1.1.1 Graphene on Nickel surfaces

The adsorption of a Graphene overlayer on metal surfaces has been studied for 40 years both for its application in catalysis and as a covering material to reduce the chemical reactivity of metals. In last few years the study received renewed interest with the purpose of creating large high quality Graphene samples. To this purpose, several different transition metal surfaces have been used [15], each of them with its peculiar advantages and disadvantages.

In our work we analyze Graphene adsorbed on Nickel (111) surfaces. One of the advantages is the fact that Nickel (111) surface translational vectors have a length roughly

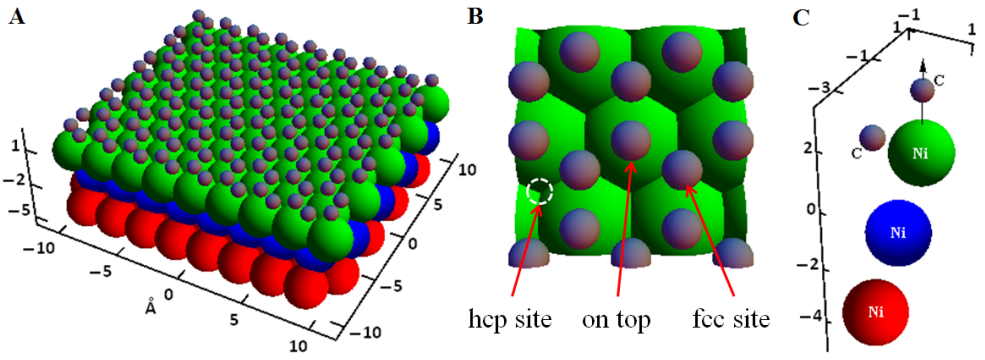

Figure 1.4: Graphene Nickel (111) top-fcc configuration.
A: Graphene adsorbed on a trilayer Nickel (111) slab.
B: Adsorption sites: one of the two inequivalent carbon atoms sits on top of the topmost Nickel layer atoms, the other in the fcc hollow sites of the surface, while the hcp (Hexagonal Close Packed) sites are left empty.
C: Relative position of the carbon and Nickel atoms in the unit cell: one of the carbon atom is on top of the first layer Nickel atom, the other is on top of the third layer Nickel atom; thicker Nickel slabs are obtained repeating the three Nickel atoms in the vertical direction.

equal to the one of Graphene, being 2.49 Å. As a consequence, the geometrical properties of Graphene are preserved, this issue is also reflected on the Low Energy Electron Diffraction pattern that exhibits the same spots for both materials, and can be used to monitor the crystalline quality of the Graphene overlayer during adsorption. On the contrary, the interactions between the Nickel substrate and the Graphene overlayer are quite strong. On the one hand, this is an advantage because the overlayer can be formed easily by different techniques [15], and the formation of bilayer or multilayer of graphite is unfavorable. On the other hand, these strong interactions affect the electronic structure [16], in particular near the Fermi level, that causes Graphene to lose some of its properties.

One of the important issues of the Graphene-Nickel interface from the theoretical point of view is concerned with the Carbon adsorption sites. We recall that the Nickel crystal structure is Face Centered Cubic (fcc). For symmetry reasons, the number of possible adsorption sites for a Carbon atom on a Nickel (111) surface, preserving the LEED pattern, is finite [17, 18]. In our calculation we take advantage of the calculations made by Bertoni et al. [17] and choose as atomic structure for Graphene/Nickel the top-fcc configuration. In such a configuration the two Carbon atoms of the Graphene unit cell are adsorbed on two inequivalent sites: one sits on top of the Nickel topmost layer atoms and the other lies

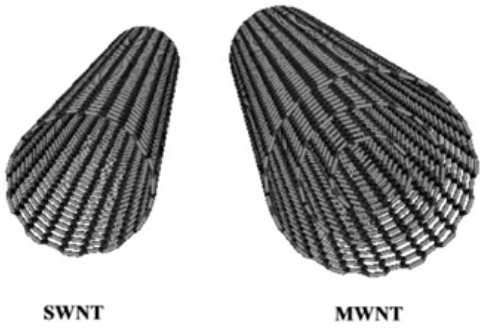

Figure 1.5: Single-walled (SWCNT) and multi-walled (MWCNT) carbon nanotubes.

on the fcc hollow sites of the surface. The direct space primitive vectors and Brillouin zone are the same the one of Graphene (see figure 1.2), apart from length corrections due to the little mismatch between the lattice constants. Figure 1.4 shows the adsorption geometry and the atoms in the unit cell in the case of Graphene adsorbed on the first 3 layers of a Nickel (111) surface.

1.2 Carbon Nanotubes

Carbon Nanotubes (CNTs) are allotropes of Carbon with cylindrical shape. They owe their name to their tube shape with diameter length in the nanometer range. Since their discovery in 1991, CNTs have been extensively investigated for their peculiar properties [14, 19], that are valuable in a vast number of fields, which include electronics, optics, material science, and medicine. As already observed, a CNT may be thought as a Graphene sheet rolled into a cylinder; since there are many different ways of rolling up a Graphene sheet, there also are many different CNTs exhibiting peculiar electronic and geometrical properties. Actually, CNTs are classified according to their properties.

The first big distinction is between single-walled (SW) and multi-walled (MW) CNTs, see figure 1.5. A single walled carbon nanotube is obtained by rolling a single Graphene layer, while a multi-walled CNT is obtained by rolling Graphene multilayers, resulting in a series of concentric single walled carbon nanotubes. All the other properties of SWCNTs are determined by their chirality, that is by how the Graphene sheet is rolled. SWCNTs are usually grouped into armchair, zigzag and chiral classes, see figure 1.6. The nanotube crystal structure, i. e., the unit cell and lattice vector, is determined by a translation vector $\mathbf{T}$ and a chiral vector $\mathbf{C}_h$. The chiral vector connects two carbon atoms in the Graphene

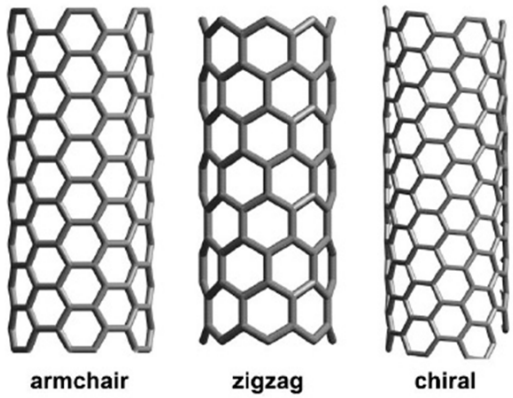

Figure 1.6: Armchair ($n = m$), zigzag ($m = 0$) and chiral (n, m) SWCNT.

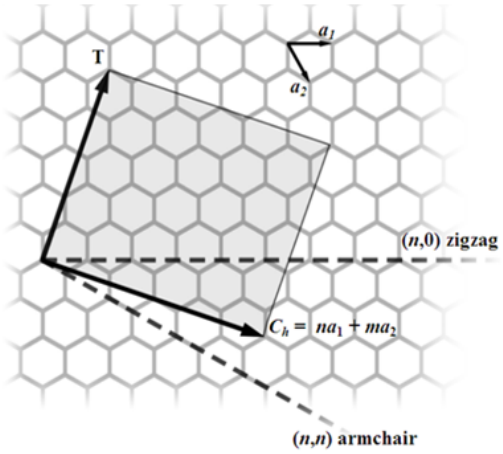

Figure 1.7: A Graphene sheet with the definition of the chiral vector $\mathbf{C}_h$ and the translation vector $\mathbf{T}$.

sheet that coincide after the rolling procedure; the translation vector is perpendicular to the chiral vector on the Graphene sheet, and spans the portion of Graphene that needs to be taken into account for constructing the unit cell of the CNT. Such a vector also represents the translation vector of the 1-dimensional lattice. Both chiral and translation vectors are uniquely determined by two indices (n, m), called chiral indices, see figure 1.7. The chiral $\mathbf{C}_h$ and the translation $\mathbf{T}$ vectors are defined as

$$\mathbf{C}_h = n\mathbf{a}_1 + m\mathbf{a}_2 \tag{1.2}$$

$$\mathbf{T} = \frac{2m+n}{\mathrm{GCD}[2n+m, 2n-m]}\mathbf{a}_1 - \frac{2n+m}{\mathrm{GCD}[2n+m, 2n-m]}\mathbf{a}_2, \tag{1.3}$$

where $\mathrm{GCD}[a, b]$ represent the greatest common divisor between a and b. The electronic

properties of a SWCNT are determined by the chiral indices (n, m). Tight binding calculations [14] show that armchair ($n = m$) CNTs are metallic. Other types of tubes are also metallic if $n - m$ is a multiple of 3, while they are semiconducting otherwise.

Chapter 2

Density Functional Theory

Density functional theory (DFT) is one of the most widely used technique for ab initio calculations of the structure of atoms, molecules, solids, surfaces, together with their properties and interactions. Though DFT is not the main subject of this thesis, it is used as a working tool for the investigations in the following chapters. The aim of this chapter is to shortly review the theoretical basis of DFT and its capabilities of calculating physical and chemical properties of materials, with particular care to electronic-structure related applications. In the following discussion we follow the approaches by Martin [1, Chapters 6 and 7], Payne and coworkers [2].

2.1 Introduction

The most challenging problem in the theoretical study of the properties of physical systems with many electrons is that, whatever the property is, one has to face with a set of equations for large numbers of electrons interacting with one another. The basic idea brought by DFT is to reduce the cumbersome problem of determining the many-body wavefunction of the system at equilibrium to the study its ground state electron density. The Hohenberg-Kohn theorems prove such a function to be the only quantity needed to define the system Hamiltonian and then all the observable properties of the system.

DFT has been very popular in solid state physics since its introduction, around the beginning of the 1970's, while its application to systems of chemical and biological interests has grown more recently, during the early 1990's, with the improved understanding and modeling of the exchange correlation energy and because of the increased computational power. Nowadays it is used both in physics and quantum chemistry to simulate a wide class of systems ranging from the condensed phase to atoms and molecules. Its main usage is devoted to the determination of properties connected to the electronic density, like total and partial energies, charge densities and dipole moments, atomic forces and stress tensors, geometries of molecules, bonds length and vibrations, phonons, and density of states.

Our main interest is the determination of one-electron energies and wavefunctions entering the ground state and excited states of Carbon based nanomaterials. In this chapter, we give a short review on DFT with specific emphasis on the techniques that will be used in the rest of the work. These arguments are organized as follows. In section 2.2, we introduce the many-electron problem and the Hohenberg-Kohn theorems that provide the foundations of DFT. In section 2.3, we shortly sketch the Kohn-Sham (KS) procedure, that is how DFT is used to solve the many-electron problem. Finally in section 2.4, we deal with the typical approximations encountered in formulating and solving the many-electron problem using DFT, paying particular attention to the exchange and correlation functionals, boundary conditions, pseudopotentials and basis sets that will be used in the following chapters.

2.2 Theoretical basis

To set up the problem, let us consider a system composed of N electrons interacting with one another via the Coulomb interaction and being probed by an external potential V_{EXT},

which may be the periodic potential of ion cores in crystalline solids. This system is described by the following Hamiltonian[1]:

$$H = -\frac{1}{2}\sum_{i}^{N}\nabla_i^2 + \sum_{i}^{N}V_{\text{EXT}}(\mathbf{r}_i) + \frac{1}{2}\sum_{i\neq j}^{N}\frac{1}{|\mathbf{r}_i - \mathbf{r}_j|}, \tag{2.1}$$

expressed in atomic units. It is well known that this kind of problem is not exactly solvable. The basic concept of DFT is that all the relevant and observable properties of the ground state of the many electron system are uniquely determined by the ground state electron density.

This kind of approach was first used by Thomas [21] and Fermi [22] who, working independently, established a statistical model in 1927 to approximate the equilibrium distribution of electrons in a many electron atom. In particular, they represented the total electron kinetic energy as a functional of the electron density $n(\mathbf{r})$:

$$T_{TF}[n] = \frac{3^{5/3}\pi^{4/3}}{10}\int d^3r\, n^{5/3}(\mathbf{r}), \tag{2.2}$$

and combined this functional with the classical expressions for the nuclear-electron and electron-electron interactions, which can be both expressed in terms of $n(\mathbf{r})$. By doing so, they first introduced the total energy density functional

$$E_{TF}[n] = T_{TF}[n] + \int d^3r V_{\text{EXT}}(\mathbf{r})n(\mathbf{r}) + \frac{1}{2}\int d^3r_1 d^3r_2 \frac{n(\mathbf{r}_2)n(\mathbf{r}_2)}{|\mathbf{r}_1 - \mathbf{r}_2|},$$

where the second term is the electron interaction with the external potential and the third term represents the classical Coulomb interaction between two charge densities, that is the Hartree energy.

Later on, Dirac [23] added a term to this functional to take into account the exchange interaction between electrons, due to the Pauli exclusion principle. The result was the Thomas-Fermi-Dirac total energy functional:

$$E_{TFD}[n] = E_{TF}[n] - \frac{3^{4/3}}{4\pi^{1/3}}\int d^3r\, n(\mathbf{r})^{4/3},$$

in which the last term is an approximation of the exchange energy.

[1]Regarding the degrees of freedom of the "positively charged" background, responsible for V_{EXT}, we are assuming that they can be viewed as frozen, as in the Born-Oppenheimer approximation [20]; their contribution to the Hamiltonian (2.1) and to the total energy functional (2.4) is indeed an additive, though configuration dependent, constant as long as only the electrons' degrees of freedom are concerned.

The problem with the Thomas-Fermi model is that it relies on approximations that are indeed too crude to get good results also in the case of simple atoms, however their idea of expressing the total energy as a functional of the electron density turned out to be very useful, as we will explain in the following sections.

2.2.1 The Hohenberg-Kohn theorems

DFT is based on two theorems introduced and demonstrated by Hoenberg and Kohn [24]. In their form, the Hohenberg and Kohn (HK) theorems allow the construction of an exact many-body theory applicable to all systems (not only interacting electrons) governed by a Hamiltonian of the form (2.1).

The first HK theorem can be stated as:

Theorem 1: *If the Ground States of two many electron systems, each containing N electrons, one with external potential $V_1(\mathbf{r})$, and the other with external potential $V_2(\mathbf{r})$, have the same ground state electron density $n_0(\mathbf{r})$, then the two external potentials differ only by an additive constant C, that is:*

$$V_1(\mathbf{r}) = V_2(\mathbf{r}) + C. \tag{2.3}$$

In other words, the first HK theorem states that the external potential $V_{\text{EXT}}(\mathbf{r})$, and then the full many body Hamiltonian (2.1), are uniquely determined by the ground state electron density $n_0(\mathbf{r})$. As a consequence, since the Hamiltonian is fully determined, except for a constant energy shift, so are the many-body wavefunctions (ground state and excited states as well). Therefore, at least in principle, all the properties of the system are determined by the ground state electron density $n_0(\mathbf{r})$.

One of the most important consequences of this is that all the observable quantities can be expressed as functionals of the electron density. In particular, the total energy functional $E[n]$ is defined by:

$$E[n] = T[n] + E_{\text{INT}}[n] + \int d^3r\, V_{\text{EXT}}(\mathbf{r})n(\mathbf{r}), \tag{2.4}$$

where we have explicitly represented as functionals the kinetic energy part of the total energy, $T[n]$, and the electron-electron interaction part, $E_{\text{INT}}[n]$.

The second HK theorem establishes a variational principle for the total energy functional:

Theorem 2: *For each external potential V_{EXT}, the total energy functional $E[n]$, defined by* (2.4)*, reaches its global minimum for the ground state density n_0 and the value $E[n_0]$ is the ground state energy of the system.*
The form of the total energy functional allows also the definition of the Universal Hohenberg and Kohn functional $F_{HK}[n]$ as:

$$F_{HK}[n] = T[n] + E_{\text{INT}}[n]. \tag{2.5}$$

By Universal, we mean that (2.5) is the same for all the many electrons system, regardless the external potential acting on them. At this point it is interesting to notice that the two HK theorems and all DFT theory can be applied to all many body problems (not only to many electron problems) provided that the universal functional F_{HK} is changed accordingly.

2.3 Kohn-Sham DFT

As stated above, HK theorems allow the construction of an exact theory for the many electron system; however, the theory is exact in principle but it can not be exploited in practice because the exact HK functional (2.5) is not known. As already observed in the case of the Thomas-Fermi model, the problem lies both in the kinetic energy term $T[n]$ and in the electron-electron interaction term $E_{\text{INT}}[n]$. Regarding the latter, one needs to model the many-body nature of the electron-electron interaction and state it as a functional of the electron density. The kinetic energy term, on the other hand, can be calculated explicitly as a sum of one body terms (see the first term in (2.1)), but it can not be easily expressed as a functional of the electron density.

A way to overcome these two difficulties is given by Kohn and Sham [25]. It consists in replacing the interacting N-electron system with N independent electrons coupled to an effective external potential that depends on the electron density. For this substitution, two assumptions are necessary, which are consistent with the HK theorems:

1. The ground state density of the interacting N-electron system, in the external potential V_{EXT}, is representable by the ground state density of an auxiliary non-interacting system.

2. The non-interacting Hamiltonian H_{AUX} contains the usual kinetic energy operator

and an effective potential V^{σ}_{EFF}, which may depend on spin degrees of freedom σ:

$$H_{\text{AUX}} = -\frac{1}{2}\nabla^2 + V^{\sigma}_{\text{EFF}}(\mathbf{r}), \tag{2.6}$$

With the first assumption, the electron density is given by the sum of the one-electron densities of the auxiliary system, i.e., the squared moduli of the N one-electron wave functions[2]:

$$n(\mathbf{r}) = \sum_{\sigma}\sum_{i}^{N'} |\psi^{\sigma}_i(\mathbf{r})|^2. \tag{2.7}$$

Though we can still write the total energy as a functional of the electron density:

$$E_{KS}[n] = T_s[n] + E_{\text{HARTREE}}[n] + E_{xc}[n] + \int d^3r V_{\text{EXT}}(\mathbf{r})n(\mathbf{r}), \tag{2.8}$$

the complexity of the many electron problem comes back, since to know $n(\mathbf{r})$ we first have to compute the N one-electron wavefunctions ψ^{σ}_i.

The KF functional (2.8) contains the non-interacting kinetic energy [3]:

$$T_s[n] = \sum_{\sigma}\sum_{i}^{N'} |\nabla\psi^{\sigma}_i(\mathbf{r})|^2, \tag{2.9}$$

which is indeed a functional of n because the density dependence is implicit in the one electron wavefunctions, $\psi^{\sigma}_i = \psi^{\sigma}_i[n]$. It also depends explicitly on the classical electron-electron interaction energy:

$$E_{\text{HARTREE}}[n] = \int d^3r_1 d^3r_2 \frac{n(\mathbf{r}_1)n(\mathbf{r}_1)}{|\mathbf{r}_1 - \mathbf{r}_2|}, \tag{2.10}$$

while all the other many-body electron-electron interactions are included in the so called exchange and correlation functional $E_{xc}[n]$.

This new formulation of the problem allows to set up an iterative search of the ground state density $n_0(\mathbf{r})$ in a self-consistent cycle, depicted in the flow chart of figure 2.1. The procedure is illustrated in more details in the following sections, together with the approximations hidden within.

[2] At this point we insert explicitly the spin index σ in the one-electron wavefunction. We must pay attention to the upper extreme of the i-summation running on the occupied one-electron wavefunctions only. For this reason, N is replaced by N', assuming $\sum_i^{N'}\sum_\sigma = N$.

[3] It is worth noticing that the kinetic energy functional $T[n]$ in (2.5) is, in general, different from the non interacting kinetic energy functional $T_s[n]$ defined in (2.9); the difference between the two forms lies in the many-body interactions that are excluded in the independent electron picture; such missed terms must be somehow included in the exchange and correlation part $E_{xc}[n]$.

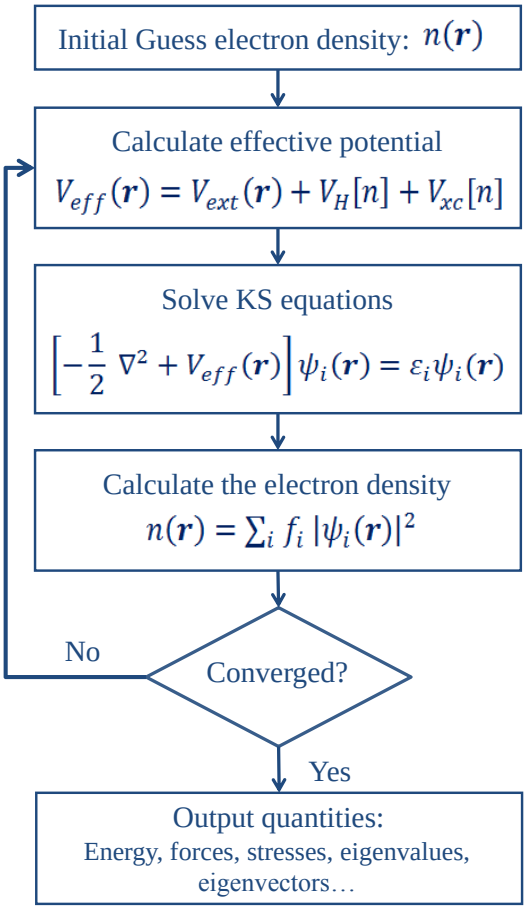

Figure 2.1: Flow chart for the KS self consistent procedure.

2.3.1 Self-consistent KS cycle

The self consistent (SC) KS cycle is quite similar to the Hartree-Fock cycle for calculating the ground state of many electron atoms [26]. The preliminary step of the SC cycle is an initial guess for the total electron density $n(\mathbf{r})$. The initial electron density can then be used to calculate the total energy functional for the first step. At this point the next step would be operating a variation in the electron density that minimizes the total energy. However, as already pointed out, this operation is not possible because it is not possible to have a simple expression of the kinetic part as a density functional. The problem is then transferred to the wave-function using equations (2.9) and (2.7). Now, the minimum

of the total energy can be obtained by equating to zero the variation of the total energy with respect to the wave-functions [4]:

$$\frac{\delta E_{KS}}{\delta \psi_i^{\sigma *}(\mathbf{r})} = \frac{\delta T_s}{\delta \psi_i^{\sigma *}(\mathbf{r})} + \left[\frac{\delta E_{\text{EXT}}}{\delta n(\mathbf{r})} + \frac{\delta E_{\text{HARTREE}}}{\delta n(\mathbf{r})} + \frac{\delta E_{xc}}{\delta n(\mathbf{r})} \right] \frac{\delta n(\mathbf{r})}{\delta \psi_i^{\sigma *}(\mathbf{r})} = 0, \tag{2.11}$$

subject to the orthonormalization condition

$$\langle \psi_i^{\sigma} | \psi_j^{\sigma'} \rangle = \int d^3 r \psi_i^{\sigma' *}(\mathbf{r}) \psi_j^{\sigma}(\mathbf{r}) = \delta_{ij} \delta_{\sigma \sigma'}. \tag{2.12}$$

Equations (2.11) and (2.12) can be put together, using suitable Lagrange multipliers ε_i^{σ} and noticing that

$$\frac{\delta T_s}{\delta \psi_i^{\sigma *}(\mathbf{r})} = -\frac{1}{2} \nabla^2 \psi_i^{\sigma}(\mathbf{r}) \quad \text{and} \quad \frac{\delta n(\mathbf{r})}{\delta \psi_i^{\sigma *}(\mathbf{r})} = \psi_i^{\sigma}(\mathbf{r}), \tag{2.13}$$

to form a Schroedinger-like equation:

$$\left(H_{KS}^{\sigma} - \varepsilon_i^{\sigma} \right) \psi_i^{\sigma}(\mathbf{r}) = 0, \tag{2.14}$$

where the KS Hamiltonian is given by

$$H_{KS}^{\sigma} = -\frac{1}{2} \nabla^2 + V_{KS}^{\sigma} \tag{2.15}$$

and the KS potential V_{KS} is nothing but the effective potential defined in (2.6):

$$V_{KS}^{\sigma} = \frac{\delta E_{\text{EXT}}}{\delta n(\mathbf{r})} + \frac{\delta E_{\text{HARTREE}}}{\delta n(\mathbf{r})} + \frac{\delta E_{xc}}{\delta n(\mathbf{r})} = V_{\text{EXT}}(\mathbf{r}) + V_{\text{HARTREE}}(\mathbf{r}) + V_{xc}^{\sigma}(\mathbf{r}). \tag{2.16}$$

The SC cycle is then structured as follows. The initial guess for the electron density is plugged as input into (2.16) to obtain the KS potential. Then, the KS Hamiltonian is calculated and the KS equation are solved to obtain the one-electron eigenvalues ε_i^{σ} and the eigenfunctions ψ_i^{σ}. These eigen-functions are used to calculate the output electron density $n(\mathbf{r})$ by (2.7), which is used as input for recalculating the KS potential and the KS Hamiltonian. The scheme is iterated self-consistently because the output electron density

[4] Equation (2.11) is obtained by varying E_{KS} with respect to the conjugate wave-functions $\psi_i^{\sigma *}$, as is done in all variational problems of quantum mechanics. This leads to the secular equations (2.14) for the wave-functions ψ_i^{σ}. Varying E_{KS} with respect to the ψ_i^{σ} leads to secular equations that are complex conjugates of (2.14), yielding as solutions the conjugate wavefunctions $\psi_i^{\sigma *}$. This is a consequence of the Hermiticity of the Kohn-Sham Hamiltonian (2.15).

of a given iteration step is necessary to obtain the input KS potential at the following step. This loop is considered to be closed, and the solution achieved, when a certain input and output quantity is similar enough that some convergence criterion is fulfilled. There are a lots of possible choices for input/output quantities in setting up the convergence criterion. For example, one can focus on the total energy, the orbital energies or the density itself. Convergency is reached when differences in the chosen quantities, calculated with the electron densities of two (or more) subsequent steps, are less than some given (small) values. The self-consistent procedure stops either when the convergence criterions is fulfilled, or when a maximum number of iterations has been performed. The last output electron density is the solution of the SCF-cycle and may be used to obtain all the other relevant properties of the system.

2.4 Approximations in solving a DFT "problem"

Up to now we have described some abstract procedures to solve the many electron problem using DFT, without introducing any real approximations. To solve practical problems however some approximations are necessary. This section is devoted to the approximations that will be encountered in the following chapters, discussing briefly the advantages and disadvantages of each one. It is necessary to stress that the topics covered are not exhaustive; for a more detailed discussion see refs.[1, 2].

2.4.1 Exchange and Correlation "Flavor"

The first approximation is the most important from a fundamental point of view, because is the only one that is necessary and is not used to ease the procedure. It concerns the HK functional. As we observed in section 2.3, direct application of the HK theorems in solving the many-electron problem is impractical due to the difficulties in expressing the kinetic energy term as a density functional and in modeling the electron-electron interaction. The KS procedure allows to "simplify" the kinetic energy part, but it keeps untouched the electron-electron interaction part. We recall that the exact HK functional is not known; in the proposed formulation, all the unknown parts of the HK functional are included in the exchange-correlation term, E_{xc}, of the total energy functional (2.8), or in the exchange-correlation potential, V_{xc}, used to define the effective KS potential (2.16).

The exchange-correlation energy is of course a density functional, then we may write:

$$E_{xc}[n] = \int d^3r\, n(\mathbf{r})\varepsilon_{xc}([n], \mathbf{r}) \tag{2.17}$$

where the ε_{xc} is an energy per particle and it is in general a complicated "function" of the position $\mathbf{r}$, the density $n(\mathbf{r})$ and the density gradient $\nabla n(\mathbf{r})$, that can be calculated in principle for all the possible positions $\mathbf{r}$.

Indeed, there are several possible choices for V_{xc}, or equivalently for ε_{xc}; we are not going here to explore all of them. In fact, we do not have a universal exchange-correlation functional, because each different physical situation has its proper approximations and so its "best" exchange-correlation functionals. However the functionals can be grouped into classes according to some of their main features.

One of these is the class of *Local* functionals. A functional is local if ε_{xc} is a function of the position $\mathbf{r}$ and of the electron density (together with its derivatives) calculated at the same position $\mathbf{r}$. Local functionals are, for example, the functionals that use the local density approximation (LDA) [27, 28, 29, 30]:

$$E_{xc}^{LDA} = \int d^3r n(\mathbf{r})\varepsilon_{xc}^{LDA}(n(\mathbf{r}), \mathbf{r}), \tag{2.18}$$

and its generalization to include the dependence of ε_{xc} on the derivatives of the density, called generalized gradient approximation (GGA) [31]:

$$E_{xc}^{GGA} = \int d^3r n(\mathbf{r})\varepsilon_{xc}^{GGA}(n(\mathbf{r}), |\nabla n|, \ldots, \mathbf{r}). \tag{2.19}$$

For non-local functional [32] it is not possible to write a simple expression like (2.18) or (2.19) because the calculation of $\varepsilon_{xc}([n], \mathbf{r})$ includes the evaluation of the density n, and eventually its derivatives ∇n, in $\mathbf{r}$ and at other spatial positions, say $\{\mathbf{r}_i\}$.

Another class of density functional is obtained for exchange-correlation terms depending explicitly on the one-electron orbitals, which is called orbital-dependent functional. Among these, we mention the LDA+U method [33], where an artificial potential term (U) acting only on localized orbitals (like d and f orbitals in transition elements) is added to a standard LDA functional. Finally, in the so called Hybrid functionals [34], a non-local density term is combined with the exact Hartree-Fock exchange term.

2.4.2 Periodic and finite-size calculations

As we stated in the introduction, DFT can be used to study both finite size entities and large bulk materials.

Finite size entities are, for instance, atoms and molecules and in general all systems that are composed by a (fixed) finite number of atoms and then have a finite number of electrons. In this case the cluster of atom is considered isolated in space and the DFT algorithm of Fig. 2.1 can be applied directly.

On the contrary, bulk property of macroscopic materials can be studied, by means of DFT methods, with periodic boundary conditions. A periodic calculation is set up by constructing a fundamental finite size cluster of atoms, called the unit cell. In this way the number of electron in the unit cell is finite. The unit cell is periodically replicated using some displacement lattice vectors $\{\mathbf{R}\}$ to construct the bulk solid, that has infinite size and then is made by indefinite numbers of atoms and electrons. The periodic description allows to apply the Bloch theorem [35] and express the wavefunctions as Bloch states:

$$\psi_{n\mathbf{k}}(\mathbf{r}) = e^{i\mathbf{k}\cdot\mathbf{r}}\, u_{n\mathbf{k}}(\mathbf{r}) \tag{2.20}$$

where the function $u_{n\mathbf{k}}(\mathbf{r})$ has the same periodicity of the lattice[5] and depends on the band index n and on the quasi wavevector $\mathbf{k}$. Moreover the periodic properties of the wavefunctions are reflected in the density that is periodic and may be calculated by summing over the occupied band states that are half the number of the electrons in the unit cell. Indeed, the complexity of infinitely extended systems is recovered because the calculation of the density is made integrating over $\mathbf{k}$. The $\mathbf{k}$ integral however can be replaced by a summation over a finite number of $\mathbf{k}$-points in the first Brillouin zone (BZ). This is indeed an approximation and is usually done by the method of Monkhorst and Pack [36]. The latter consists in sampling the BZ with points that are not connected with one another by symmetry operations, or, equivalently, by sampling the irreducible part of the first BZ, that is the part of the BZ that can be used to construct the full BZ using symmetry operations.

Periodic Supercells

It should be stressed that the distinction between finite size and periodic calculations is not sharp. There exists intermediate situations in dealing, for example, with one or two dimensional objects that can be modeled by periodic structures in reduced dimensions. Typical examples are surfaces and graphene, for two dimensional objects, and nanotubes

[5] The periodicity of $u_{n\mathbf{k}}$ allows to write $u_{n\mathbf{k}}(\mathbf{r}) = \sum_{\mathbf{G}} c_{n,\mathbf{k}+\mathbf{G}}\, e^{i\mathbf{G}\cdot\mathbf{r}}/\sqrt{V}$, where V is the volume of the solid and $\{\mathbf{G} \in \mathbb{R}^3 : \mathbf{G}\cdot\mathbf{R} = 2\pi l, l \in \mathbb{N}\}$ the reciprocal lattice. This makes the plane-wave basis set a natural, but not the only, choice in periodic calculations, see section 2.4.4.

for one dimensional objects. These cases are usually treated by intermediate types of calculations, i. e., using the Bloch's theorem only along the *truly* periodic directions. Such an approach, however, is impossible with plane-wave basis sets (see section 2.4.4), then the problem is handled by means of supercells. The idea is to create a three dimensional lattice and let the translational vectors become very big in the directions in which there is no true periodicity. In this way, we are actually constructing a fictitious periodic system in three dimensions, replicating the system that we want to study in the non-periodic directions. The translational vector lengths have to be large enough to ensure that the system replicas do not see each other.

Supercell approaches are also applied to study defects in three dimensional systems, which break the translational invariance of perfect crystals. The Bloch representation and plane-wave basis sets may be also used, in the same way as outlined above, to study finite size systems, like large atoms and molecules. Ideally, the length of the translation vectors in the non-periodic direction should go to infinity, however it is usually limited by computational costs, due to the increase of the number of atoms and basis functions. Finally, we remark that finite size calculations involving large number of atoms can be used to obtain information on bulk properties, when one wants to avoid a periodic calculation. Such a choice, has inevitable computational costs and practical limitations: the theoretical capability of most commercial and free open-source codes for finite size calculations is of the order of 10^4 atoms, however a large cluster of atoms is generally made of 10^3 entities.

2.4.3 All electron and Pseudo-Potential methods

A way to ease the computational burden and reduce the convergency times of DFT codes is to define suitable pseudo-potentials eliminating inert electrons, which do not participate directly to the process understudy [1, Chapter 11]. The main underlying idea is that, for most purposes, the core electrons can be viewed as tightly bound to the ionic cores and relatively inert. This observation leads to substituting core electrons with an approximately averaged screening influence on the ionic potential that is parametrized by pseudo-potentials. Among the advantages of this procedure we mention the reduced electron number and basis set size, especially in periodic calculations where the sharply peaked core orbitals require large numbers of plane waves to be reproduced.

Construction of a pseudo-potential consists in finding a potential whose eigenfunctions perfectly match the original all electron wavefunctions at electron-nuclear distances r larger

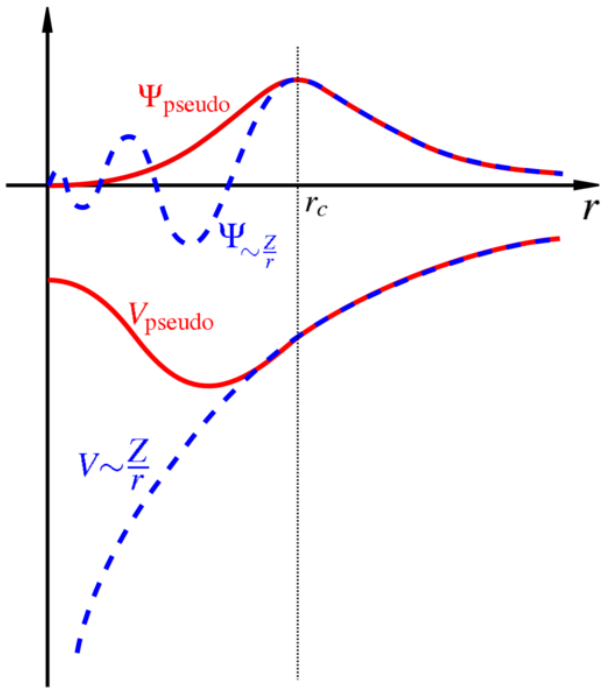

Figure 2.2: Schematic comparison between the Coulomb potential and a possible choice of pseudo-potential; in the picture is also shown the difference between the all-electron and the pseudo-eigenfunctions.

than a given cut-off distance r_{cut}. This usually consists in removing the divergent part of the potential for $r \to 0$, as shown schematically in Fig. 2.2. The main disadvantages are that, on the one hand, no information can be obtained from core electrons, and, on the other hand, the pseudization procedure gives valence wavefunctions with wrong behavior at $r < r_{cut}$; a classical example is the pseudized $2s$ wavefunction of a many-electron atom that has no nodes, while it should have one node.

Choosing of the *correct* pseudo-potential in a DFT calculation is one of the most difficult and important parts and, even in this case, it is not possible to define a perfect pseudo-potential for all situations concerning a given atom. Usually, the pseudo-potentials are tested with available experiments on some measurable quantities. It is worth noticing that there are a numerous standard techniques for pseudo-potential generation. Here, we mention only the two big categories of norm-conserving [37] and ultra-soft [38] pseudo-potentials. Norm-conserving pseudo-potentials enforce the condition to the norm of their eigenfunctions that must equal the norm of the original all-electron eigenfunctions for integrations above r_{cut}. Ultra-soft pseudo-potentials release this condition to further decrease

the size of the basis set.

In some situations the desired output quantities are directly related to core electrons, so the use of pseudo-potential is not possible and all-electron calculations are necessary.

2.4.4 Basis set

In 2.3.1 we saw that at each step of the KS self-consistent cycle we need to solve a time-independent Schroedinger-like problem (2.14), which means to find eigenfunctions and eigenvalues of the KS Hamiltonian (2.15).

A way of easing the procedure is to expand each one-electron wavefunction in components of a suitable basis set $\{\phi_j\}$:

$$\psi_i^\sigma(\mathbf{r}) = \chi_\sigma \sum_j^{N_{basis}} c_j^\sigma \phi_j(\mathbf{r}), \tag{2.21}$$

where the $\{c_j^\sigma\}$ are undefined complex numbers, and χ_σ accounts for the spin part of the electron state. The correctness of the reconstruction of ψ_i^σ depends on the completeness of the basis set. Obviously, a complete basis set is made by an infinite number of basis functions that can not be used in practice, so the number of basis components N_{basis} is a compromise between the computational cost and the "fidelity" of the representation (2.21).

The introduction of a basis allows to transform the problem (2.14) in a matrix diagonalization problem, at each step of the SC cycle, whose ingredients are the matrix elements $\langle\phi_i|H_{KS}^\sigma|\phi_j\rangle$ of the KS Hamiltonian and the overlap integrals $\langle\phi_i|\phi_j\rangle$ between the basis functions[6]. Diagonalization leads to a set of N_{basis} eigenvalues $\{\varepsilon_i\}$ and eigenvectors $\{c_j^\sigma\}$, which reproduce ψ_i^σ, and hence allows to calculate the electron density $n(\mathbf{r})$ in (2.7).

Each different problem has its best basis set and it should be stressed that a wrong choice of the basis set may result in wrong calculations or non-converging SCF cycles. Among the many possible choices of basis sets we mention plane waves, and localized orbitals [1, chapters 14,15].

Plane waves, generally used in periodic calculations[7], are defined by the reciprocal lattice vectors $\{\mathbf{G}_j\}$ chosen to expand the periodic part $u_{n\mathbf{k}}(\mathbf{r})$ of the Bloch function (2.20):

[6] Indeed it is not necessary to use a set of orthogonal basis function as basis set, so the overlap integrals between different basis functions can be nonzero.

[7] As previously stated, plane waves may be also used for finite-size objects, by means of periodic supercell methods.

$$\phi_j(\mathbf{r}) = \frac{1}{\sqrt{V}} e^{i\mathbf{G}_j \cdot \mathbf{r}}. \tag{2.22}$$

These are normalized using the volume V of the solid, which is the unit-cell volume in real space multiplied by number of $\mathbf{k}$-points used in the BZ sampling. The number of plane waves included in the basis set is usually limited by a cut-off energy E_{cut}, so that only the plane waves fulfilling $|\mathbf{k} + \mathbf{G}_j|^2 < 2E_{cut}$, for all considered $\mathbf{k}$-points, are included in the calculation. It should be noted that plane waves are not the best choice for all-electron calculations, because reliable representations of the localized core orbitals can be achieved only by using very large numbers of plane waves, that results in inefficiently slow computations.

All-electron calculations are generally performed using localized orbitals as basis sets, which are the natural choice to describe finite size systems. Localized orbitals are also employed in periodic tight-binding calculations to reproduce the periodic parts of the Bloch functions. Among the different localized functions available for defining a basi set, we mention:

1. Slater type orbitals (STOs) [39] are analytical functions, whose shape mimic the eigen-functions of the Hydrogen atom. Being spherically symmetric, STOs are usually expressed as products of spherical Harmonics and radial functions, that decay like e^{-r}. STOs enter ab-initio calculations of simple diatomic molecules [26] and can be used both for all electron and pseudo-potential DFT codes.

2. Gaussian type orbitals (GTOs) [40] are spherically symmetric functions with Gaussian radial parts, which have the advantage of easing matrix-elements integrations and speeding up SC iterations. They can be used both for all electron and for pseudopotential calculations. GTOs may be also expressed in cartesian form with an angular part which is a homogeneous polynomial in the components of the position vector.

3. Numerical atomic orbitals (NAOs) [41] are spherically symmetric functions whose radial parts are computed numerically. Unlike the GTOs and STOs, NAOs have the advantage that they can be defined on a finite size support. Being centered on the atomic cores, the overlap between two NAOs is exactly zero when the corresponding centers are sufficiently far apart. NAOs are usually defined as finite support approx-

imations of some analytic functions or from numerical pseudo-potential calculations for the isolated atom.

Finally, it is worth noticing that some techniques use mixed basis functions, like the Projector Augmented Plane Waves method (PAW), with localized functions for the regions near the atomic cores and plane waves for the interstitial regions. An application is provided by the localized d and f orbitals in the LDA+U method.

Chapter 3

Auger electron emission from Carbon Nanotubes

In this chapter we present an ab-initio approach to calculate the Auger transition rate of a many-electron system, once its ground-state one-electron properties are known. The starting point is first-order time-dependent perturbation theory, expressed in terms of the Fermi Golden Rule (FGR), that is combined with a suitable method, like density functional theory (DFT), giving as outputs the one-electron energies and wavefunctions needed to determine the cross-section for the Auger effect. We apply the developed tool to conducting single walled carbon nanotubes (SWCNTs) [3] of the $(10, 10)$ armchair type, and compare the results with Auger electron emission spectroscopy (AES) measurements on Bucky papers [4]. We focus on initial and final state effects that rely on many body correlations lying outside the FGR, which turn out to be extremely important for achieving good agreement between simulations and experiments.

3.1 Introduction

Auger electron emission is a crucial phenomenon for understanding the local electronic structure of solid-state materials. It is at the heart of AES, a widely used surface science technique, which yields a unique spectrum for each chemical species. This peculiarity is due to the local nature of the Auger effect, which has as initial state a missing inner-shell electron. In Carbon nano-structures, AES is based on the analysis of energetic electrons ejected by the sudden creation of a $1s$-hole. The emission mechanism is due to one of the valence $2s/2p$ electrons tunneling to neutralize the core-state and the other being ejected into the vacuum. Accordingly, the Kinetic energy distribution of ejected electrons carries information on the occupied density of the σ and π band levels and the repulsion matrix elements between the initial and final states of the process. From the theoretical point of view, Auger emission rates can be calculated once the many-body wave-functions (for the ground and excited states of the material system) are known. Exact calculations are still impractical, because of the determinantal complexity of these wave-functions. However, ground-state DFT calculations provide information on the one-electron quasi-orbitals and energy levels, which may be used as inputs in the cross-section for Auger electron emission, as given by the FGR [42]. An interesting point is the 'flexible nature' of DFT codes where, for example, we can: (i) include all system electrons or replace the core-electrons by suitable pseudo-potentials; (ii) use finite-size or periodically boundary conditions; (iii) choose localized orbital or plane-wave basis sets. What are left out of the FGR are many-electron correlations, which significantly affect both ends of the Auger core-valence-valence (CVV) spectrum from SWCNTs [3]. Indeed, the final energy of emitted electrons depends on both the initial and final valence band states that are directly or indirectly involved in the Auger effect. The former are shaken up by the core-hole perturbation, while the latter are distorted by the interaction between the valence holes left behind by CVV transitions. Here, we explicitly discuss inclusion of these initial and final-state effects in the FGR, together with finite lifetime corrections. Analysis of the Auger emission properties of SWCNTs with this approach allows us to state the role played by these many body effects in strongly correlated electrons.

The chapter is organized as follows. In section 3.2 we shortly sketch the physical idea behind the Auger effect. In section 3.3 we develop a method to calculate the Auger electron emission rate in the FGR, starting from the set of one-electron orbitals and energies computed with Hartree-Fock (HF) or DFT codes. In section 3.4 we apply the method

of section 3.3 to determine the Auger emission spectrum of a $(10, 10)$ SWCNT. Finally, in section 3.5 we introduce the many-body correlations outlined above and apply them to the calculations of section 3.4, comparing the resulting numerical spectrum with existing Auger measurements on SWCNT bundles [4].

3.2 Auger effect

The Auger effect is a de-excitation mechanism of an inner-shell core-hole that results in the emission of an electron from a valence state. The necessary condition is the creation of a core-hole by x-ray absorption or electron bombardment.

The simplest situation is that of an isolated atom in which a core hole has been created. Fig. 3.1 shows a simple sketch of the Auger effect. The ionized atom with an empty core state of energy E_C lies in an excited state; one of the outer electrons, from an energy level E_1, tunnels to neutralize the core hole; this results in a energy surplus (the excitation energy $E_1 - E_C$) that is dissipated either with the fluorescence of an x-ray photon or with the emission of another outer electron from an energy level E_2. The later is termed '*Auger electron*'. After this process the atom is left doubly ionized. The kinetic energy of the Auger electron is related, by total energy conservation, to the energies of the electronic levels involved in the process. In the simple picture of Fig. 3.1 the kinetic energy of the emitted electron is given by the relation

$$E_K = -(E_C - E_1 - E_2) \tag{3.1}$$

and the emission spectrum is in principle a Dirac delta function of the emission energy, whose lineshape will be eventually corrected to embody initial and final states effects.

The simple form (3.1) links the kinetic energy of the emitted electron to the electronic states involved in the emission mechanism, therefore, it clearly shows that the Auger effect can be used to probe the electronic properties of atoms, molecules and solids. Indeed, the energy levels involved in the emission mechanism are characteristic of the particular atom where the core-hole has been created, so that Auger electrons act as fingerprints of chemical species present in the target materials. This makes the underlying AES technique a powerful tool for both qualitative and quantitative analysis of solid surfaces and surface like objects, because both core hole creation and electron emission are processes that take place at surfaces, due to the short mean free path of electrons in matter at low energies, on the electronvolt energy-scale.

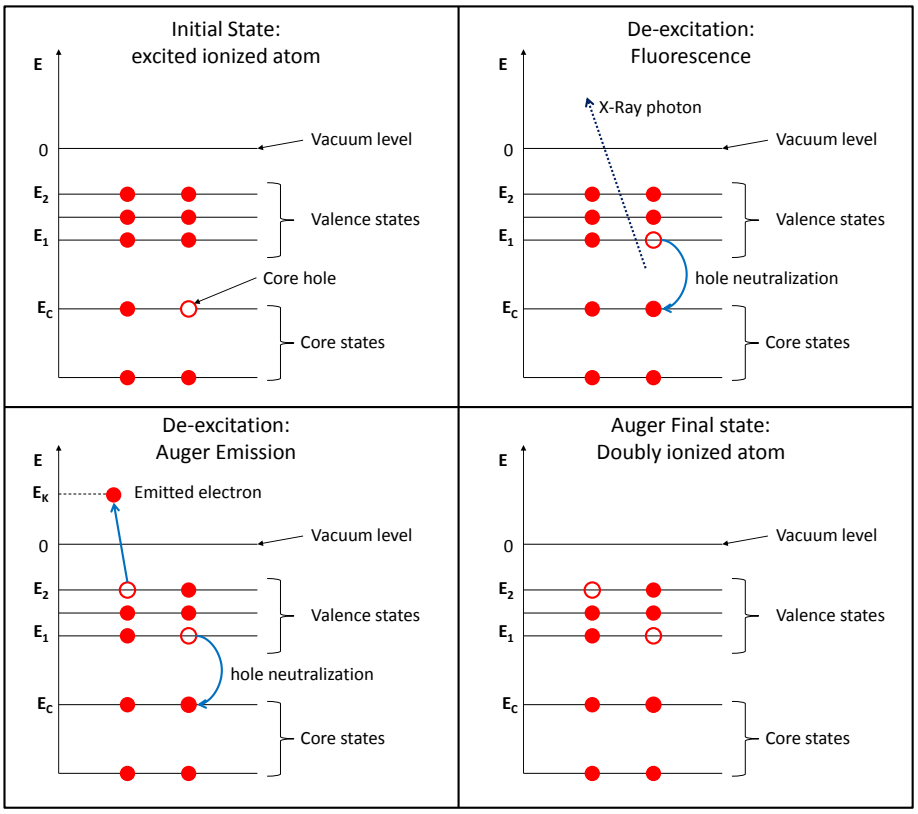

Figure 3.1: Schematic sequence explaining the initial state and possible de-excitation mechanisms for an atom with a core hole. *Top left*: initial state, an ionized atom with a core hole. *Top Right*: de-excitation through fluorescence: an electron from the energy level E_1 relaxes to the core level E_C through emission of a soft x-ray photon; the final state ia a ionized atom with the hole in the E_1 level. *Bottom Left*: Auger de-excitation: the electron from the energy level E_1 neutralizes the core hole E_C while another electron is emitted from the electron state E_2 with a kinetic energy E_K. *Bottom Right*: Auger final state: At the end of the process the atom is doubly ionized.

In solids, the one-electron energy levels are organized in bands, so the situation is similar to the atomic and molecular cases, with the neutralizing and emitted electrons coming from the same or from two distinct energy bands. In this case, the Auger process can be used to study the electronic structure of the investigated materials and, moreover, the electron-electron interactions among band electrons. Emission line-shapes produced by Auger electrons are determined, in first approximation, by the density of states of the involved valence bands, weighted by the proper transition matrix elements, and corrected by initial and final state effects.

Our purpose is the calculation of the Auger emission spectrum from SWCNTs. In Carbon based materials, the energy level are simple because they are made by a deep narrow band, originating from the $1s$ levels, and a series of overlapping bands, coming from $2s$ and $2p$ levels of isolated Carbon atoms. To simplify the picture, we can imagine all these bands to mix together forming valence and conduction bands. Since we are interested in Auger emissions from CVV transitions, both neutralizing and emitted electrons come from the valence bands.

3.3 Auger cross section

The simplest way of handling the calculation of the Auger cross-section is to apply first-order time-dependent perturbation theory [42]. We assume our system to be composed by all the electrons from its constituents atoms: the initial state is an excited state and the potential responsible for the Auger effect is the Coulomb interaction. The lowest order transition rate T for the process is then given by the FGR [42]:

$$T = 2\pi \sum_F \rho(E_\mathrm{F}) \left|V_\mathrm{FI}\right|^2 \delta(E_I - E_F), \tag{3.2}$$

where V_FI denote the matrix elements of the potential between the initial state $|I\rangle$ and a bunch of final states $|F\rangle$, $\rho(E_\mathrm{F})$ is the density of final states, and the delta function ensures total energy conservation. From the knowledge of the transition rate, we can evaluate the probability per unit energy and unit emission angle that the process occurs. Such a key-quantity is proportional to the differential cross section of the process.

We conveniently use a second quantized formalism [43, 44] and assume that, whatever the system, we are able to solve the complicated many-electron problem for its ground state $|0\rangle$ in which the N_el electrons that make up the system occupy the lowest N_el energy levels. The excited states can be obtained by application of creation and annihilation fermion operators, b_i and $b_i^\dagger$, in the following way:

- $b_i^\dagger |0\rangle$ is the many-body state with an extra electron in the one-electron state $|i\rangle$, if such a state is unoccupied[1];
- $b_i |0\rangle = 0$ if the one-electron state $|i\rangle$ is occupied;

[1] Hereinafter, we include in a single letter all the good quantum numbers defining the one-electron state including spin degrees of freedom.

- $b_j |0\rangle$ is the many-body state with a missing electron in the one-electron state $|j\rangle$, if the latter is occupied;
- $b_j^\dagger |0\rangle = 0$ if the one-electron state $|j\rangle$ is unoccupied.

We recall the canonical anti-commutation relations for the fermion operators:

$$\{b_r, b_s^\dagger\} = \delta_{rs}, \tag{3.3}$$

$$\{b_r, b_s\} = \{b_r^\dagger, b_s^\dagger\} = 0; \tag{3.4}$$

and the definitions of field and adjoint-field operators:

$$\Psi(\mathbf{r}) = \sum_i \phi_i(\mathbf{r}) b_i \quad \text{and} \quad \Psi^\dagger(\mathbf{r}) = \sum_i \phi_i^*(\mathbf{r}) b_i^\dagger, \tag{3.5}$$

where ϕ_i represent the one-electron wavefunction, associated to the energy level ε_i, in the space representation.

The electron-electron Coulomb potential is a two body operator so it is defined as:

$$\hat{V} = \frac{1}{2} \int d^3r \int d^3r' \frac{1}{|\mathbf{r} - \mathbf{r}'|} \Psi^\dagger(\mathbf{r}) \Psi^\dagger(\mathbf{r}') \Psi(\mathbf{r}') \Psi(\mathbf{r}). \tag{3.6}$$

For our purpose it is convenient to change the notation by adopting the following conventions: we denote by d, c, and a the creation/annihilation operators for core, valence, and free electrons in the states specified by quantum numbers s, v, and q, respectively. In this way the field operator definition is split in three summations:

$$\Psi(\mathbf{r}) = \sum_q \phi_q(\mathbf{r}) a_q + \sum_v \phi_v(\mathbf{r}) c_v + \sum_s \phi_s(\mathbf{r}) d_s \tag{3.7}$$

Correspondingly, the two-body potential (3.6) turns out be composed of 81 distinct terms, each one made of 2 creation and 2 annihilation operators. These terms incorporate all Coulomb interactions among one-electron states, and include the many-body effects that we will treat in section 3.5. Among the 81 sub-operators, we also have the Auger Neutralization (AN) potential that creates an electron in a core-level and a free electron, while it destroys two valence electrons:

$$\hat{V}_{\text{AN}} = \sum_s \sum_q \sum_v \sum_{v'} V_{s\,v'}^{q\,v} a_q^\dagger d_s^\dagger c_{v'} c_v \tag{3.8}$$

where we have introduced the shortened notation:

$$V_{s\,v'}^{q\,v} = \int d^3r \int d^3r' \phi_q^*(\mathbf{r}) \phi_v(\mathbf{r}) \frac{1}{|\mathbf{r} - \mathbf{r}'|} \phi_s^*(\mathbf{r}') \phi_{v'}(\mathbf{r}') \tag{3.9}$$

for the two-electron integrals. This type of potential gives nonzero results only if the initial and final states entering

$$V_{\mathrm{FI}} = \langle \mathrm{F} | \, \hat{V}_{\mathrm{AN}} \, | \mathrm{I} \rangle \, . \tag{3.10}$$

are linked by an Auger process similar to the one sketched in Fig. 3.1.

The final state is obtained from the ground state by creating a free electron of wavevector $\mathbf{q}_f$ and destroying two electrons with the valence numbers v_f and v'_f:

$$|F\rangle = c_{v'_f} c_{v_f} a^\dagger_{q_f} |0\rangle \quad \Longleftrightarrow \quad \langle F| = \langle 0| \, a_{q_f} c^\dagger_{v_f} c^\dagger_{v'_f} . \tag{3.11}$$

The initial state, instead, is the ground state with a missing core electron in a state s_i:

$$|I\rangle = d_{s_i} |0\rangle \, , \tag{3.12}$$

that we fix in order to remove the s-summation from V_{FI}. The spin of the core-state is also fixed, which has important consequences on the integral (3.9) because of spin-conservation. We will see that summing over different spin orientations of the core-state results in a factor of two in V_{FI}, and a factor of four in the cross-section of the Auger process.

Using equations (3.8), (3.10), (3.11), and (3.12) we can write:

$$V_{\mathrm{FI}} = \sum_s \sum_q \sum_v \sum_{v'} V^{q\ v}_{s\ v'} \langle 0| \, a_{q_f} c^\dagger_{v_f} c^\dagger_{v'_f} a^\dagger_q d^\dagger_s c_{v'} c_v d_{s_i} |0\rangle \, , \tag{3.13}$$

which is easily evaluated using:

$$\langle 0| \, a_{q_f} c^\dagger_{v_f} c^\dagger_{v'_f} a^\dagger_q d^\dagger_s c_{v'} c_v d_{s_i} |0\rangle = \delta_{q q_f} \delta_{s s_i} \left(\delta_{v v_f} \delta_{v' v'_f} - \delta_{v' v_f} \delta_{v v'_f} \right) ; \tag{3.14}$$

to obtain:

$$V_{\mathrm{FI}} = V^{q_f\ v_f}_{s_i\ v'_f} - V^{q_f\ v'_f}_{s_i\ v_f} . \tag{3.15}$$

We recall that, to evaluate the Auger transition rate, we need to take the squared modulus of V_{FI} and then sum over the final states, that in our case corresponds to compute the following summations $\sum_{q_f} \sum_{v_f} \sum_{v'_f}$ restricted by energy conservation. We observe that, as long as the spin-orbit interaction is neglected, spin degrees of freedom have the only effect that each electronic state may be occupied by at most two electrons with opposite spins. Explicit inclusion of spin quantum numbers, however, causes some of the integrals (3.9) to vanish giving rise to the direct and exchange interactions of the HF theory. In particular, the initial neutralizing valence electron state and the core state must have the same spin. The same constraint holds for the initial emitting valence state and the final plane wave

state. Summing over spin quantum numbers and dropping the subscripts i and f from the matrix elements (3.15), we may rewrite the Auger transition rate as:

$$T = 4\pi\rho(E_f)\sum_{q}\sum_{v}\sum_{v'}\left(2\left|V_{s\,v}^{q\,v'}\right|^2 + \left|V_{s\,v}^{q\,v'} - V_{s\,v'}^{q\,v}\right|^2\right)\delta(\varepsilon_q - \varepsilon_{v'} + \varepsilon_s - \varepsilon_v). \tag{3.16}$$

The main ingredients in this relation are the one-electron wavefunctions and energies of the system understudy. The key point is recognizing that the emitted electron can be represented by a plane wave ϕ_q, of wave vector $\mathbf{q}$ and energy $\varepsilon_{\mathbf{q}} = \hbar^2|\mathbf{q}|^2/2m$, and the density of final states coincides with the free electron DOS: $\rho \propto \sqrt{\varepsilon_{\mathbf{q}}}$. Eq. (3.16) allows evaluation of the Auger cross section and the Auger spectrum, i. e., the energy distribution of electrons emitted along a given direction. Such a quantity is proportional to the probability density for an electron to be emitted with energy $\varepsilon_{\mathbf{q}}$ inside the solid angle Ω:

$$\Xi_0(\varepsilon_{\mathbf{q}}, \Omega_{\mathbf{q}}) = \sum_{v\,v'} W_{v\,v'}(\mathbf{q})\delta(\varepsilon_{\mathbf{q}} - \varepsilon_{v'} + \varepsilon_s - \varepsilon_v), \tag{3.17}$$

where the δ function eliminates one of the two summations over the valence states, and the effective potential

$$W_{v\,v'}(\mathbf{q}) = W_{v\,v'}(\varepsilon_{\mathbf{q}}, \theta_{\mathbf{q}}, \phi_{\mathbf{q}}) = W_0\rho\left(2\left|V_{s\,v}^{q\,v'}\right|^2 + \left|V_{s\,v}^{q\,v'} - V_{s\,v'}^{q\,v}\right|^2\right) \tag{3.18}$$

contains both the direct and exchange energies of the HF theory plus a normalization constant W_0 constraining

$$\int d\varepsilon_{\mathbf{q}} \int d^2\Omega_{\mathbf{q}}\Xi_0(\varepsilon_{\mathbf{q}}, \Omega_{\mathbf{q}}) = 1. \tag{3.19}$$

In the next sections we will apply Eq. (3.17) to calculate the CVV Auger line for a SWCNT.

3.4 Cluster and Periodic calculations of Auger electron emission from a $(10, 10)$-carbon nanotube

As shown in the former section, the inputs of the Auger rate (3.16) and normalized spectrum (3.17) are the one-electron eigenenergies and eigenfunctions of the investigated system. We choose to calculate them using DFT combined with two different basis sets and boundary conditions. More specifically, we perform an all-electron cluster and a pseudopotential periodic calculations on a conductive nanotube of chiral indices $(10, 10)$ [3].

The same approaches have been applied to conducting tubes of different lengths and radii [45, 46]. In the present calculation, the two DFT methods give almost identical energy levels and density of states and two necessarily different sets of one-electron orbitals that we use to evaluate the FGR (3.16).

3.4.1 Ground state calculations

We begin our analysis with the primitive cell of a $(10, 10)$ SWCNT used to generate a cluster of 540 Carbon atoms lying on the surface of a tube of radius 6.875 Å and length ~ 35 Å. We add 20 Hydrogen atoms to passivate the dangling bonds of each of the tube ends. We choose the coordinate system shown in Fig. 3.2, together with the unit-cell of the tube, where the x axis coincides with the tube axis and the z axis points long a radial direction connecting the tube center to a reference atom located at $\mathbf{R}_0 = (0, 0, 6.875)$ Å.

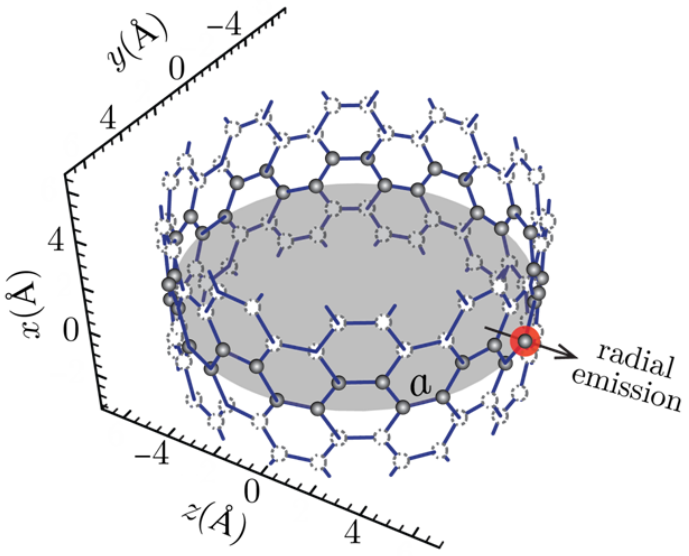

Figure 3.2: Portion of the $(10, 10)$ SWCNT used for both periodic and cluster DFT calculations outlined in the text. The gray spots denote the primitive cell of the structure. Core hole creation is simulated on the highlighted atom, from which we calculate the Auger spectrum.

We perform restricted Hartree Fock (RHF) and DFT computations using the quantum chemistry code called GAMESS [47], with the minimal 3G basis set by Huzinaga [48] and the Generalized Gradient Approximation (GGA) by Perdew Burke and Ernzerhof (PBE) [49] for the exchange and correlation functional. The output ground-state wave-function is

made of 1640 molecular orbitals (MOs), with two electrons of opposite spins per MO. In the MOs we can distinguish 540 core-orbitals and 1100 occupied valence orbitals.

The energy levels for the 540 core orbital are nearly degenerate in a range of 0.18 eV around a mean energy ε_c, taking the value -269.88 eV with respect to the vacuum level, whereas the experimental energy lies at about -290 eV. Such a disagreement is due to a well known inaccuracy of HF and DFT calculations in predicting the energy spectrum of Carbon based nanostructures [50]. The same scaling procedure is usually employed in DFT calculations of the Graphene band structure [51]. The core orbitals are linear combinations of $1s$-orbitals of free Carbon, resulting, however, in 540 orbitals sharply peaked on each of the Carbon atoms. With this in mind, we choose to confuse the core "*band*" with a multiple degenerate state, of energy ε_c, whose wavefunctions, denoted by $\phi_s = \langle \mathbf{r}|1s_{\mathbf{R}}\rangle$, are made by atomic Carbon core functions. The latter are taken from the used basis sets and centered on each Carbon atom positions $\mathbf{R}$.

On the other hand, the valence orbitals $\phi_v = \langle \mathbf{r}|v\rangle$ can be expanded as

$$\langle \mathbf{r}|v\rangle = \sum_{\mathbf{R}} \sum_{i=s,p_x,p_y,pz} v_{i\,\mathbf{R}} \langle \mathbf{r}|i_{\mathbf{R}}\rangle, \tag{3.20}$$

where i represents a contracted Gaussian orbital, that may have s- or p- symmetry and is centered at the $\mathbf{R}$-site, and $v_{i\,\mathbf{R}}$ is the corresponding coefficient obtained from the secular equations yielding the optimized ground state. Their energy levels form a quasi-continuum whose occupied portion lies between -24.35 eV and -4.55 eV, see Fig. 3.3**A**. The upper value of this interval, designating the highest occupied orbital, and denoted ε_F, is consistent with Fermi level measurements on SWCNT bundles [52]. The energy levels show a narrow "*band gap*" (see the inset in Fig. 3.3**A**) between the occupied and unoccupied parts, while the armchair $(10, 10)$ nanotube should be metallic. This is an effect of finite size calculations, as observed in refs. [46, 53]. From the one-electron states we can construct a DOS by partitioning the occupied energy range in steps of 0.2 eV and counting the number of one-electron states inside each interval; the valence orbital expansion (3.20) allows us to construct a *projected DOS* onto states with defined symmetry; the result of this procedure appears in Fig. 3.3**B**. We observe that the DOS is dominated by the s component at the bottom of the valence band. Then, we have the s contribution going to zero and the p components raising up with increasing the valence energy towards ε_F. We clearly see that p_y and p_z components bring identical contributions, while the p_x DOS is different; this is a direct consequence of cylindrical symmetry, x being the axial direction of the tube. We also observe that the highest occupied valence states are made up only by

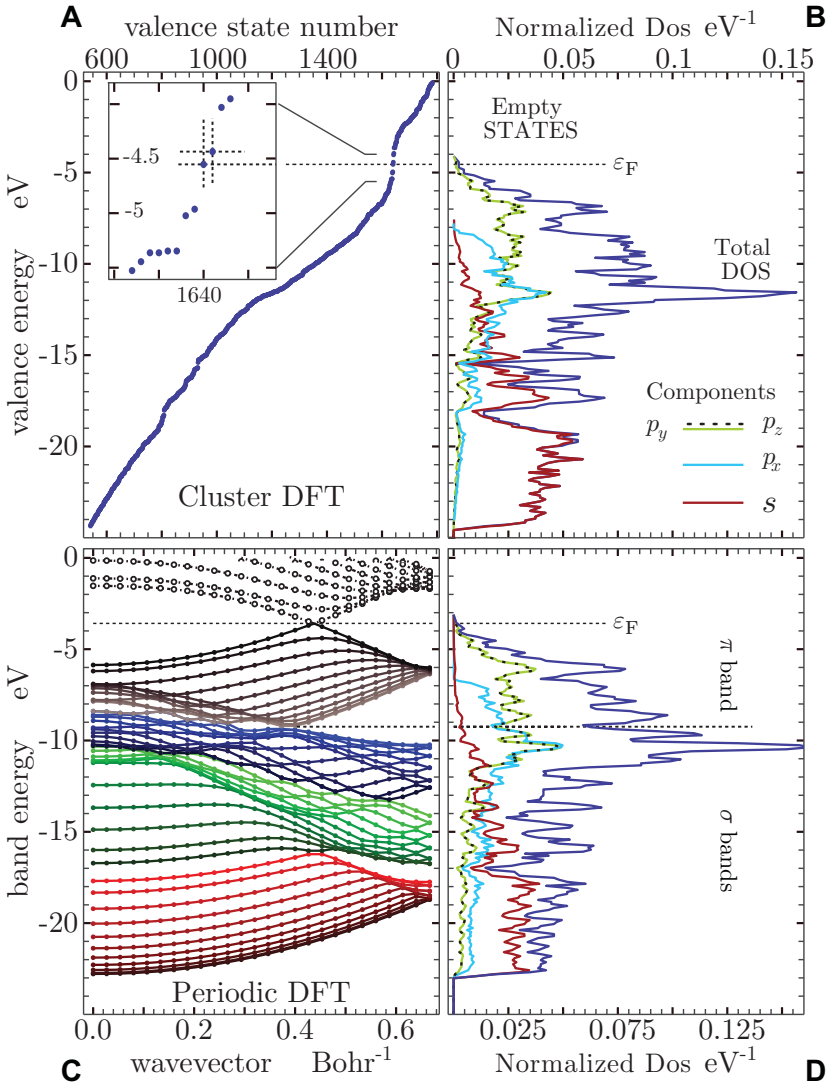

Figure 3.3: Valence energies **(A)** and valence DOS **(B)** of a 35 Å$(10, 10)$ SWCNT, whose unit cell is shown in figure 3.2, as obtained by finite-size all-electron calculations with the GAMESS code [47]. Band energies **(C)** and DOS **(D)** for the same SWCNT obtained by periodic pseudo-potential calculations with the SIESTA code [41]. In both cases, the partial DOS related to the s, p_x, p_y, p_z orbital are obtained from the squared moduli of the optimized coefficients of Eq. (3.20)

p_y and p_z components, which are p-shaped orbitals oriented along the tube radius. The latter correspond to π states in unrolled graphene that extend along the perpendicular direction to the graphene sheet.

To complete our study, we perform periodic pseudopotential calculations on the same

nanotube with the unit cell of Fig. 3.2, using the DFT code called SIESTA[41]. We keep the GGA approximation for the exchange and correlation functionals in the PBE parametrization and use a double zeta basis set of numerical orbitals for the valence states. Such a basis set is derived from a norm-conserving pseudopotential of the Troullier and Martins type [54] replacing the $1s$ orbitals. We choose a sampling 26 k-points in the irreducible segment of the one dimensional Brillouin Zone (BZ). Accordingly, we obtain 80 doubly occupied states per k-point corresponding to a total number of 2080 wave-functions, whose eigenvalues range from -22.78 eV to $\varepsilon_F = -3.70$ eV; these wavefunctions are written using Eq. (3.20) where the multiple index v includes the band and k-point indices, $\langle \mathbf{r}|i_{\mathbf{R}}\rangle$ denotes the numerical orbital centered at the $\mathbf{R}$ site of the primitive cell, and $v_{i\mathbf{R}}$ contains the phase factor of the Bloch wave expansion. The band structure, the corresponding DOS and projected DOSes are shown in Fig. 3.3**C** and **D**. We observe a small band gap, which is however an artifact of the BZ sampling failing to catch the k-point where valence and conduction bands touch.

Direct comparison between the computed DOS with the finite-size and periodic approaches shows that both bandwidth and peak positions are in substantial agreement. Projected DOS analysis give compatible results of the two methods in the energy range from ε_F down to $\varepsilon_F - 12$ eV. On the other hand, we see substantial differences in the component contributions near the bottom of the valence band, where the s DOS appears to be depressed in periodic calculations with respect to cluster calculations. Furthermore, in periodic DFT the p components are non vanishing in the same energy window. This difference may be addressed to the pseudo-potential approach that has removed the $1s$ state, bringing mayor consequences on the s-symmetry of the valence pseudo-orbitals, as we will see later on.

3.4.2 Evaluation of the Auger cross section

Once we have obtained the one-electron energies and wavefunctions, we can apply Eq. (3.16) to calculate the probability for Auger electron emission (3.17). Such an evaluation passes through the computation of the Auger matrix elements (3.9) that, using the expansion (3.20), can be written as linear combinations of Coulomb integrals involving a localized s-type orbital (coming from ϕ_s), and the plane wave (ϕ_q), for the initial state, and two localized functions of either s or p symmetries (included in ϕ_v and $\phi_{v'}$), for the final state. These integrals are analytical if the localized functions are the contracted Gaussian

type orbitals of GAMESS calculations, while they need be simplified by partial wave expansion and computed numerically for the numerical orbitals of SIESTA calculations (see appendix A). Nevertheless, the complexity of the problem is still very high resulting in an impractical procedure due to the large number of atomic components involved in the valence states[2].

To reduce the numerical burden we focus only on one reference atomic site, the one denoted $\mathbf{R}_0$ in Fig. 3.2, and we place the core hole onto this site. Next, we compute the Coulomb integrals (3.9) within the on-site approximation, that is we retain only the coefficients $v_{i\mathbf{R}_0}$ and the atomic states $|i_{\mathbf{R}_0}\rangle$ in the expansion (3.20) of the valence wavefunctions. This approximation is justified by observing that the core hole orbital is sharply peaked at the atomic site where it is centered and its value is nearly zero at atomic distances far from this site. Actually, we performed an evaluation of the nearest neighbor contribution to the Auger spectrum for a smaller size nanotube and we indeed observed negligible corrections to the on-site approximation [45].

With the on-site approximation, we compute the first-order energy distributions of ejected electrons $\Xi_0(\varepsilon_{\mathbf{q}}, \theta = 0)$, shown in Fig. 3.4**A** and **B** for both DFT approaches, which account for all possible transitions leading to electron ejection along the radial direction z of the tube. Partial spectra are obtained by considering separately the components that describe CVV transitions involving the ss, $p_{x(y)}p_{x(y)}$, sp_z, $p_{x(y)}p_z$ and p_zp_z parts of the valence states, respectively. In this way, we can distinguish partial cross-sections where either the neutralizing or the ejected electrons originate from the band states that we denote σ_s (s symmetry), σ_p (p_y and p_x symmetries), and π (p_z symmetry).

The symmetry of the on-site contributions in the Coulomb integrals (3.9) yield a simple angular dependence to all the $W_{v\,v'}$ matrix elements in the FGR spectrum (3.17) and allows us to analytically compute the angular-integrated distribution

$$N_0(E) = \int_{\Omega_0} d^2\Omega \Xi_0(E, \Omega). \tag{3.21}$$

which describe CVV processes involving other core-hole sites at the central region of the tube. The main features of the averaged spectrum (3.21) are shown in Fig. 3.4**C** and **D** for Auger emissions within the solid angle $\Omega_0 \sim 1.85$ sr, corresponding to a cone of

[2]For example, in the present application, each valence state results from 40 and 580 localized orbitals in periodic and cluster approaches, respectively. This implies that each matrix element of the form (3.9) requires $1,600$ and $336,400$ computations per core site, while the number of transitions involved in Auger electron emission are $1,210,000$ and $4,326,400$, respectively.

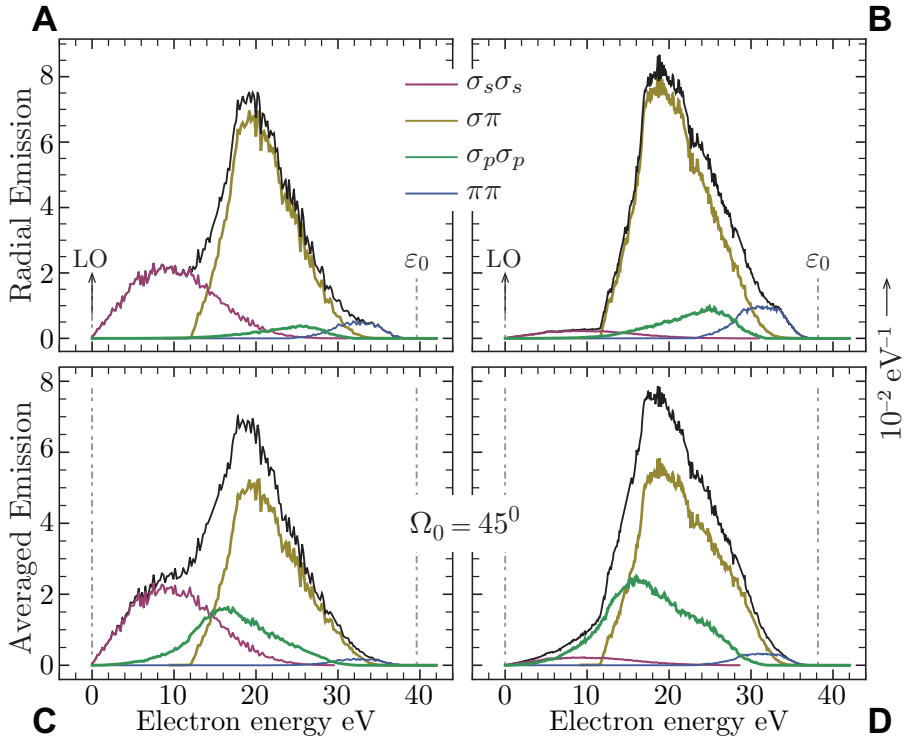

Figure 3.4: Normalized distributions of electrons ejected from a SWNCT cluster (**A**,**C**) and a periodic SWCNT (**B**,**D**). The spectra are resolved into the different emission components explained in the text. In panels **A** and **B** we have plotted the radial emission distributions, while in panels **C** and **D** we show angular averaged calculations over an emission cone with a semi-aperture of $\sim 45°$. Emission energies are referred to electrons emitted from the lowest occupied level (LO) so that the edge of the emission spectrum ε_0 corresponds to the total CVV bandwidth.

$\sim 45°$ relative to the z-direction. The discrepancies between the s and p valence DOS in the two DFT approaches (Fig. 3.3**B**, 3.3**D**) are reflected in unequal CVV rates for electrons ejected from the bottom of the valence band. Indeed, the CVV spectrum contains products of two one-electron DOS whose partial components differ, in the two models, at high binding energy by a factor of $\sim 2-3$. Moreover, we can expect different behaviors of the Auger matrix elements between all-electron and pseudo-potential calculations, because in the latter case the valence orbital are accurate beyond the cut off radius of the pseudo-potential, while we are calculating a matrix element with a narrow $1s$ orbital. Interestingly, the biggest discrepancy concerns the $\sigma_s\sigma_s$ sub-spectrum being more intense by a factor of ~ 8 in cluster calculations. The other subcomponents of the CVV spectrum

are in excellent agreement with one another, demonstrating that only the $2s$ orbitals are significantly disturbed by the pseudo-potential within the $1s$-region. We remark that the FGR rate (3.16), generating the integral spectrum (3.21), has been calculated from the DFT ground-state, which implies that both core and valence orbitals are frozen during the entire process.

3.5 Many body effects

Further insight, into the CVV spectral profile, results from accounting for many body correlations that produce permanent changes in the electronic structure, and cause non non-stationary behavior of initial and final states. In particular, initial-state effects manifest in the sudden core-hole creation and decay, whereas final-state effects are mainly due to the interaction between the valence holes and their subsequent recombination. Both these phenomena are a consequence of the electron-electron interaction and are embodied in the 81 terms of the Coulomb potential expansion (3.10). Finite lifetime of the initial core hole and the final valence holes are additional many-body effects to be included in a realistic simulation of the Auger spectrum.

Initial-state, dynamic core hole screening is dominant on valence electrons close to the Fermi level, that may be excited by the effective core-hole potential and produce asymmetric distortions in the Auger emission spectrum. Such a collective excitation becomes critical in x-ray absorption spectra from simple metals that exhibit a power-law anomaly known as Fermi edge singularity [55, 56]. In Eq. (3.10), the many-electron shake-up is accounted for by the term:

$$\hat{V}_{\mathrm{FE}} = \sum_{s} \sum_{v} \sum_{v'} V_{s\ v'}^{s\ v} d_s^{\dagger} d_s c_{v'}^{\dagger} c_v. \tag{3.22}$$

Final-state correlations are inherent the valence holes created by the Auger effect (see Fig. 3.1), and propagating in the valence bands due to the potential:

$$\hat{V}_{\mathrm{HH}} = \sum_{v_1} \sum_{v_2} \sum_{v_1'} \sum_{v_2'} V_{v_1\ v_1'}^{v_2\ v_2'} c_{v_1}^{\dagger} c_{v_1'} c_{v_2}^{\dagger} c_{v_2'}. \tag{3.23}$$

Accurate evaluation of these features would require DFT calculations of the excited many-body states of the system: the initial state without one core electron, and something like 10^6 combinations of final states without two valence electrons and with an ejected electron (Fig. 3.3). To overcome such an intractable situation, we adopt a semi-phenomenological

scheme where the decay probabilities for core and valence holes are converted into lifetime widths that produce a Lorentzian broadening of the spectra.

We take a contact potential for the core-hole perturbation over a range Δ_0 around $\varepsilon_{\rm F}$, and neglect the variations of the valence DOS within the same range. Thus, we can model the singular response of π electrons by the Mahan, Nozières, and De Dominicis (MND) theory of soft X-ray absorption [55, 56], which predicts ejected electrons around the CVV threshold ε_0 to be more energetic than in the unperturbed case (Fig. 3.4). The MND approach yields an asymmetric broadening distribution of the form

$$\mathrm{MND}(E) = \frac{e^{-(E-\varepsilon_0)/\Delta_0}}{\Gamma(\alpha)\Delta_0^{\alpha_0}(E-\varepsilon_0)^{1-\alpha_0}}, \tag{3.24}$$

with Γ the Euler Gamma function, being nonzero for $E > \varepsilon_0$, which implies that the effect is manifested at energies above the CVV threshold. The α_0-parameter is a critical exponent characterizing the average core hole effect on ejected electrons.

Valence hole-hole correlations are to be found in the two-hole interacting DOS, denoted $D^{v_2 v_2'}_{v_1 v_1'}$, which is combined in a four-index tensor relation with the Auger potential terms (3.9) to give the corrected CVV rate of the process [4]. If the excited many-electron states of the system could be still represented in terms of the ground state valence orbitals, the correlated DOS would take the (diagonal) form

$$D^{v_2 v_2'}_{v_1 v_1'}(E) = \delta_{v_1 v_1'}\delta_{v_2 v_2'}\delta(\varepsilon_{\mathbf{q}} + \varepsilon_s - \varepsilon_{v_1} - \varepsilon_{v_2} + u_{v_1\, v_2}), \tag{3.25}$$

where $u_{v_1\, v_2}$ is the average hole-hole repulsion integrals. In a 'mean field' approach, we may focus just on the diagonal matrix-elements (3.25) raplacing the δ-terms in the FGR rate (3.16). In this way, we are considering each CVV transitions, concurring to the first order response $\Xi_0(\varepsilon_{\mathbf{q}}, \Omega)$, to be shifted towards lower energies by the average repulsion of the valence-holes.

With the simplified picture so far outlined, many-body effects lead to correcting the FGR spectrum $\Xi_0(\varepsilon_{\mathbf{q}}, \theta = 0)$ and the angular integrated spectrum $N_0(E)$ as:

$$N(E) = \sum_{vv'} \int_{\Omega_0} d^2\Omega W_{vv'}(E, \Omega) \mathrm{B}^{\alpha_0 \Delta_0}_{\gamma_0 \delta_0}(E + \varepsilon_s - \varepsilon_v - \varepsilon_{v'} + u_{vv'}). \tag{3.26}$$

where $\mathrm{B}^{\alpha_0 \Delta_0}_{\gamma_0 \delta_0}$ is the broadening function due to initial-final state lifetimes (Lorentian broadening of width γ_0), many-electron shake up (MND distribution of critical exponent α_0, and width Δ_0), and an additional Gaussian broadening (of width δ_0) which accounts for the

electron-phonon coupling at room temperature [57, 58, 59, 45, 46]. We point out that the MND-term is applied only if either or both v and v' run over a π-band state, thus it involves only the $\sigma\pi$ and $\pi\pi$ components of the energy distribution. We also notice that angular integration affects only the Auger matrix elements $W_{vv'}$, thus we can separate the broadened components $N_{ll'}$ of the whole spectrum $N(E)$, with $ll' = \sigma_s\sigma_s$, $\sigma_p\sigma_p$, $\sigma\pi$, and $\pi\pi$, as we did in Fig. 3.4**C** and 3.4**D**. To further simplify the understanding of hole-hole effects, we use the scheme followed Houston et al. [60]. In particular, we compute $N(E)$ by letting all $u_{vv'} \to 0$, and distort each $N_{ll'}$ by an effective hole-hole repulsion energy $U_{ll'}$, using the Hilbert transform of $N_{ll'}$, here denoted $I_{ll'}$. In this way we, reduce the information on the shifts $\{u_{vv'}\}$, which should be calculated from the valence holes of the excited states of the system, to four effective energy parameters. We expect suitable choice of these parameters to compensate for the missing off-diagonal matrix elements of the two-hole interacting DOS. The distorted distributions take the form of the Cini CVV spectrum from filled-band systems [61, 62]

$$\tilde{N}_{ll'}(E) = \frac{N_{ll'}(E)}{[1 - U_{ll'}I_{ll'}(E)]^2 + \pi^2 U_{ll'}^2 N_{ll'}^2(E)}. \tag{3.27}$$

To visualize how the changes brought by Eqs. (3.26) and (3.27) influence the Auger line-shapes of Figs. 3.4**C** and 3.4**D**, we take advantage of previous studies and fix the broadening widths to $\gamma_0 \sim 0.06$ eV [63], $\delta 0 = 0.3$ eV [57, 58, 59, 45, 46]. We estimate the shake-up parameters from the X-ray photo-emission line-shape from nanotube bundles, letting $\Delta_0 \sim 2.9$ eV and $\alpha_0 \sim 0.85$ [59]. As for the effective hole-hole repulsion energies, we use similar values to those proposed in refs. [45, 46] , by taking $U_{\pi\pi} = 0.01$ eV, $U_{\sigma\pi} = 0.02$ eV, and $U_{\sigma_p\sigma_p} = 4.5$ eV, while we separately apply the Cini distortion function (3.27) to CVV processes originating from s-valence states. In particular, we allow hole-hole correlations to be more efficient at the bottom of the valence band, using a larger value for $U_{\sigma_s\sigma_s}$ than $U_{\sigma_p\sigma_p}$. The resulting energy distributions are shown in Fig. 3.5, where we have put in evidence the effect of the σ-band distortion. We need to observe that the peculiar structure of the denominator of Eq. (3.27) is such that the intensities of the undistorted spectra ($N_{ll'}$) and the effective repulsion energies ($U_{ll'}$) are non-linearly correlated: the more intense is $N_{ll'}$, the less amount of $U_{ll'}$ is needed to distort it. A more reliable parameter to compare distorted spectra of different intensities is the average energy displacement between the distorted and the undistorted line-shapes, which in view of Eq. (3.26) can be interpreted as the mean hole-hole interaction energy.

For example, the considered value $U_{\sigma_p\sigma_p} = 4.5$ eV brings an average hole-hole inter-

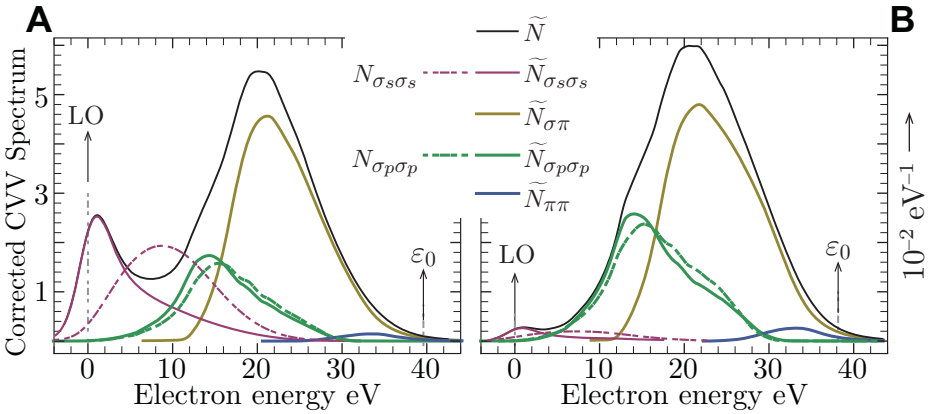

Figure 3.5: Many body corrections to the FGR spectra of figure 3.4 and their components; high binding energy distortions, broadening widths and shake-up parameters are discussed in the text. The $\sigma_s\sigma_s$ and $\sigma_p\sigma_p$ unperturbed contributions from both cluster (**A**) and periodic (**B**) calculations are displayed to highlight the distortion procedure.

action energy of $\overline{u}_{\sigma_p\sigma_p} = 0.8$ eV and $\overline{u}_{\sigma_p\sigma_p} = 0.8$ eV to the $\sigma_p\sigma_p$ sub-spectra, as obtained from the cluster and periodic DFT approaches, respectively. On the other hand, applying a similar distortion to the $\sigma_p\sigma_p$ parts of Fig. 3.4**C** and 3.4**D** means to consider close values for the average interaction energy between the two s-holes, but largely different values for $U_{\sigma_s\sigma_s}$. Based on the cluster calculations of ref. [46], we set $\overline{u}_{\sigma_s\sigma_s} = 1.5 - 2$ eV, which corresponds to $U_{\sigma_p\sigma_p} \sim 18 - 20$ eV in the $\sigma_s\sigma_s$-component of Fig. 3.4**C**.

Comparison with experiments requires a further adjustment of the valence energy widths to the observed band width [50]. To do so, we assume the valence eigenstates, calculated with both DFT methods, to have eigenenergies in an artificially expanded energy-scale of $\sim 7 - 8\%$, which allows the core level to get the correct experimental value of -290 eV. We, then, select the data of ref. [4], acquired on nanotube bundles of diameter in the range $1.3 - 1.4$ nm, where the high binding energy resonance was clearly resolved. As shown in Fig. 3.6, not only we find excellent agreement with the measured features of the spectrum at emission energies above ~ 250 eV, but we also provide evidences that the peak at ~ 240 eV is an effect of the hole-hole interaction. We confirm the interpretation of ref. [4], although more accurate studies are needed before reaching any final conclusion. As a final remark we observe that the Fermi edge singularity is somewhat quenched in conducting nanotubes by the decreasing behavior of the valence DOS, which goes virtually to 0 at ε_F (Figs. 3.3**B** and 3.3**D**). On the contrary, the dynamic screening of

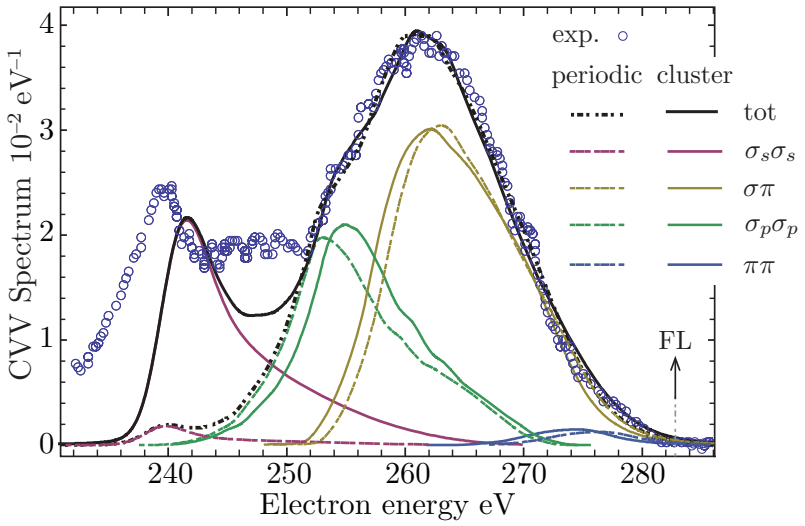

Figure 3.6: Normalized distributions and band-components of figure 3.5 stretched horizontally by 7.5% and compared with the measurements on carbon nanotube bundles, ref. [4].

π-electrons is more efficient in tubes of different chirality that offer electron structures with narrow band gaps, and virtually divergent DOS. This means that our shake-up parameters might have been overestimated.

3.6 Conclusions

In conclusion, we have presented two DFT models to determine the Auger CVV spectra of electrons ejected from conducting SWCNTs, taking into account the full effect of the on-site electron-electron interaction. Using the FGR, we have computed the cross section for Auger electron emission from a core-hole placed at the center of the tube along directions parallel to the tube diameter. We observed that the FGR approach gives an Auger emission spectrum with structures that our method was capable to assign to different Auger process, where the involved electrons come from different orbitals. At this stage we see that the pseudo-potential method give results that differ from the all electron method only in the low energy part of the spectrum (s-s part). This issue can be addressed to the pseudization procedure that gives orbitals that are accurate only beyond the pseudopotential cut-off radius. This point affects the carbon CVV auger cross section because the latter involves the evaluation of a matrix element with the $1s$ orbital characterized by a very narrow function. The effect is prominent in the s-orbitals because these are mostly influenced by

the pseudization procedure for symmetry reasons.

We have extended the calculations to include the effect of other core-holes, around the tube's central region, by averaging over different emission angles. We have attempted a simple modeling of the many body effects inherent in CVV processes, based on the original theory by Cini and Sawatzky [61, 62], and following the procedure outlined by Houston et. al. [60]. In both cases we see that the procedure predict a low emission energy resonance, observed experimentally [4].

We have included the many-electron shake-up around the Fermi energy by a heuristic procedure related to some previous studies on ion induced Auger electron emission from simple metals [57, 58], X-ray photoemission from bundles of SWCNTs [59], and CVV emission from infinite Carbon nanotubes [45]. The collective effect induced an asymmetric broadening on the calculated emission spectrum that affect principally the high emission energy of the spectrum. We have found satisfactory agreement with measurements of CVV electron emissions from SWCNT bundles [4].

Chapter 4

Secondary electron emission from Graphene adsorbed on Ni(111)

In this chapter we present experimental measurements of electron emission, induced by electron bombardment, from graphene adsorbed on Nickel (111) surfaces [5, 6, 7, 8]. In particular, we focus on secondary electron emission spectra and their properties, by varying the experimental parameters. Then, we develop a simple method, based on a density functional theory (DFT) approach, to calculate the density of unoccupied states. We first apply it to graphite, using experimental data taken from the literature, and then to the Graphene-Nickel system to reproduce some features observed in our experimental spectra.

4.1 Introduction

Secondary electron emission (SEE) is a fundamental phenomenon in particle-solid interactions and is important in a wide variety of areas like surface analysis, microscopy, electrical discharge and plasma processing of materials, particle accelerators. Studies of the energy distribution of emitted electrons, the secondary electron spectrum, and its integral, the electron emission yield (number of emitted electrons per incident particle), reveal the complexity of the process that is generally discussed as a three-step process: in depth excitation by primary particles, transport of secondary excited electrons by collisions toward the surface, escape through the surface barrier. Transport of secondary electrons occurs by multiple elastic and inelastic scattering events. The main product of this collision cascade is an energy distribution of emitted electrons characterized by a broad continuum spectrum, peaked at low energy and monotonically decreasing at high energy. This spectrum can be superimposed by spectral features arising from the peculiar density of final excited states, and from specific emission processes such as the Auger de-excitation of inner-shell holes or Plasmon decay.

All these features and the small electron mean free path at low energy make SEE particularly suitable to study surface like objects, in particular Graphene. Interestingly, SEE experiments on Graphene have been undertaken only recently, even though experimental measurements on graphite and on graphite adsorbed on different surfaces proved to be suitable for the study of the empty states of the system. In this chapter we analyze the SEE properties of the system Graphene adsorbed on Nickel (111), basing our analysis on experimental measurement of electron emission induced by electron bombardment. The main features observed in the emission spectra is a series of peaks superimposed to the cascade peak and connected to the empty bands of the system.

From the theoretical point of view, it is not possible to deal with the SEE properties without modeling properly the emission process. In particular, up to now the theoretical study of the empty states of a systems, singled out by peaks in the secondary emission spectra, has been performed only trough band structure calculations. In this work we try to do the same using DFT to calculate the band structure of our system, and applying the method to graphite experimental measurements found in literature.

The chapter is organized as follows. In section 4.2 we shortly review the experimental equipment used to adsorb a Graphene single layer on a Nickel (111) surface and to acquire the secondary electron emission spectra. In section 4.3 we present our experimental mea-

surements, in particular the SEE spectra and discuss how these spectra are modified by the experimental parameters. Then in section 4.4 we calculate through DFT the band structure of the system and introduce a simple method to go from a band structure calculation to a k-projected density of states that can be compared to the experimental measurements of the empty states obtained through SEE spectroscopy. We apply this method to graphite first, taking advantage of the vast amount of experimental data available in literature, and then to the experimental data on Graphene/Nickel presented in section 4.3.

4.2 Experimental Details

Our secondary electron emission experiments were carried out in an Ultra High Vacuum (UHV) chamber with base pressure 10^{-10} mbar. The UHV chamber is equipped with all standard facilities for surface science techniques, among the others, the one used for our measurements are an electron gun, a ion gun an hemispherical electron analyzer and a Low Energy Electron Diffraction (LEED) instrument; the chamber is also equipped with High-Resolution and Angle-Resolved electron energy loss (HREELS and AREELS) instruments. The UHV chamber is shielded with $\mu-$metal and has different gas-lines that allow controlled gas insertion into the chamber. The hemispherical electron analyzer (SPECS Phoibos 100) allows both the sample composition analysis, by means of auger electron spectroscopy (AES), and angle resolved secondary electron emission spectroscopy, operating at constant pass energy (E_{pass} = 30 eV) with an angular acceptance of 2°. The electron beam, generated by a thermionic source, lied at 90° from the axis of the spectrometer.

4.2.1 Sample preparation and preliminary analysis

The substrate on whom Graphene is deposited is a (111)-oriented surface of a high-purity Nickel single crystal. The Nickel surface was prepared with repeated cycles of sputtering with Ar ions at 2.5 keV and annealing at 1000 K. The surface contamination was monitored with AES and the crystalline order by LEED.

Graphene monolayer were grown by cracking under Vacuum ethylene at 800 K on the Nickel surface. The layer formation was monitored observing the Carbon signal in the AES spectrum of the surface. An exposure to 600 L (Langmuir 1 L= 10^6 torr s) was found to be enough for the formation of the monolayer [64, 65, 66]. Further exposition to

ethylene gave no significative changes in the carbon signal in the AES spectra, confirming that the absorption rate of carbon decreases drastically once the surface is fully covered by a monolayer, so that the further formation of other graphite layers is automatically stopped. The crystalline quality of the adsorbed monolayer was checked by LEED, that highlighted a good reconstruction of the surface [67] and a high crystalline quality. Also AREELS and HREELS techniques on our samples gave results fully consistent with the existing literature (see [15] and reference therein).

4.3 Secondary electron emission measurements

Our secondary emission study starts with a comparison (figure 4.1) between the secondary emission spectra obtained from the clean and the Graphene covered Nickel (111) surface. The surface is excited by 500 eV primary electrons impinging on the surface with an angle of $\theta_i = 45°$ with respect to the surface normal, along the **ΓK** direction. The electron analyzer collects the electrons emitted with an emission angle of $\theta_e = 45°$ with respect to the surface normal, along the **ΓK** direction, see section 1.1 for the Brillouin Zone geometry. The spectra are collected keeping the sample connected to the same bias voltage, namely -5 V with respect to ground, to see the onset of the electron emission. In figure 4.1 we show the collected spectra, normalized to the same height to compare line-shapes.

As it is often the case for secondary emission from metal surfaces, the Ni spectrum is dominated by a broad cascade peak of secondary electrons starting at ~ 7 eV, with a maximum at ~ 9 eV and smoothly decreasing at high energies. The onset of the spectrum gives information about the work function (the minimum energy required to emit an electron) of the sample. The origin of the energy scale is determined by the electron analyzer work function. In our case we were able to set it by measuring the position of a know Auger line. In the figure we use the same value of the origin for both spectra. In this way we can't give an absolute value for the work function, rather we can measure work function differences.

Now we can focus on the modification that the adsorbed Graphene induces to the emission spectrum. We can notice two main differences. First of all we see that the onset of the two spectra is located at different energies. This is a consequence of the fact that the surface work function decreases by roughly 1 eV when the surface is covered by Graphene. Then we can observe that the spectrum is not smooth anymore but it is constituted by a series of peaks superimposed to the cascade peak.

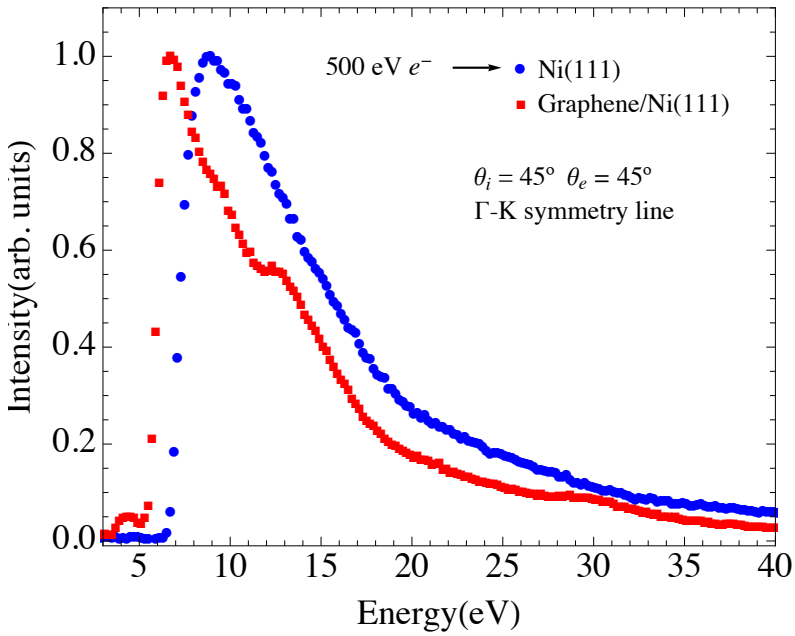

Figure 4.1: Secondary electron emission spectra of a clean (blue circles) and a Graphene covered (red squares) Ni(111) surface, excited by 500 eV electrons; the inset shows the experimental geometry. Both samples were biased with respect to ground by −5 eV. The spectra are normalized to the same height to compare line-shapes. The horizontal axis origin is set to the same value for both spectra (see text).

In figure 4.2 we try to analyze the peak series that we will call fine structure from this moment on. A spectrum acquired using a primary electron energy of 700 eV and the same experimental geometry as in figure 4.1 is shown in figure 4.2**A**. Three main feature are clearly visible, labeled **I**, **II**, and **III**. The three features appear to be superimposed to the smoothly decreasing cascade peak. Other peaks can be resolved after a background substraction of the cascade peak, represented by a smooth polynomial function and that appears as a red line in figure 4.2**A**. The procedure of the background substraction is illustrated in figure 4.2**B**, where a zoom-in of the subtracted data is shown for two spectra, acquired with 500 eV and 700 eV primary electron energies. The substraction highlights the three main features and other weaker features, labeled **a** and **b**. It should be mentioned that the procedure shown in figure 4.2 is extremely complicated and somehow arbitrary because there is no justification for the choice of the function that represents the background and because it doesn't allow to resolve structures that can be hidden near the maximum of the cascade peak, rather, local maxima can be searched for by other means that we employ for the fine structure analysis later on.

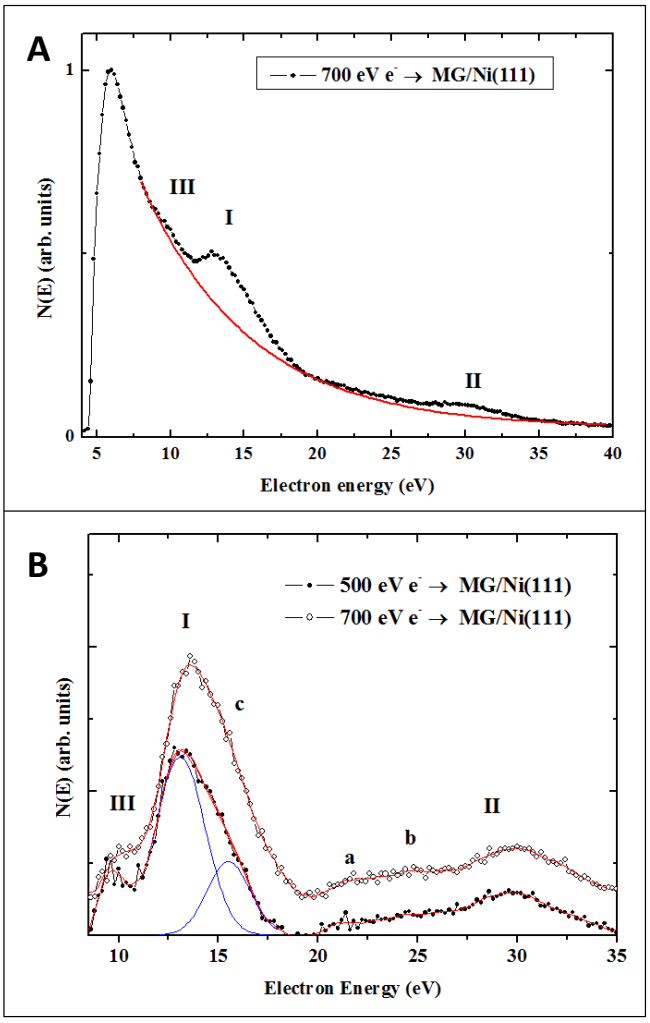

Figure 4.2: *Panel* ***A***: Electron emission spectrum from Graphene/Ni(111) using 700 eV primary electrons and the same experimental geometry of figure 4.1; the three main peaks, labeled **I**, **II**, and **III**, are highlighted; the red line is the function used for secondary electron background substraction.
Panel ***B***: Data after background substraction for 500 eV and 700 eV impinging on Graphene Nickel; other three feature, **a**, **b**, and **c**, are resolved.

4.3.1 Fine structure properties

The comparison in figure 4.1 shows that the fine structure is the main consequence of the Graphene deposition on the Nickel substrate. To understand the origin of the peaks we carried out a qualitative analysis of the behavior of the fine structure when we changed the experimental parameters.

In in figure 4.3 we carried out two different Carbon depositions, in different conditions, on the clean Nickel (111) surface and we acquired the electron emission spectra, shown in figure 4.3**A**, from both the samples in the same experimental condition, namely 500 eV electron beam impinging at 45° with respect to the surface normal and collecting the emitted electron at an emission angle of 45° on the **ΓK** direction; we also acquired the LEED pattern of both the samples shown in figures 4.3**B** and 4.3**C**. As it is clear form the LEED patterns the two Carbon deposition gave two different results. In figure 4.3**B** we can see only six spots, equal to those typical of the Ni(111) surface, meaning that we obtained a perfect reconstruction of the Nickel surface, that is the carbon overlayer is indeed a well ordered Graphene sheet. The second LEED pattern (figure 4.3**C**) shows, besides the six spots, more diffuse light and some secondary structures. We call this second sample "disordered Graphene" and it represents indeed a situation where the covering procedure of the Nickel failed to give a good graphene sheet. The comparison of the secondary electron emission spectra of these two samples is shown in figure 4.3**A**. We can see that the spectrum of the "disordered" sample exhibits a different fine structure than the one of the "ordered" sample.

The analysis of figure 4.3 shows that the fine structure is very sensitive to the crystallographic order of the Graphene overlayer. Furthermore, we also observed that the fine structure is modified and rapidly washed out by even the slightest bombardment with Helium and Argon ions.

An important issue in secondary electron emission is the dependence of the emission efficiency as a function of the energy of the primary electron beam. The total electron yield (the number of emitted electron per incident electron) is found to depend on the primary electron energy. Our main concern is, however, the dependence of the electron spectra on the primary energy and, in particular, the dependence of the observed fine structure on the primary electron energy. This issue is addressed in figure 4.4, were we compare two emission spectra excited with different primary electron energies in the same experimental geometry. As it is clear from figure 4.4 the observed fine structure exhibits no significant dependence on the primary electron energy.

The next point is exploring the dependence of the fine structure on the incidence and emission angles. In figure 4.5 we show the electron emission spectra acquired from the same Graphene/Nickel sample keeping fixed the primary electron energy and changing the experimental geometry. Though our current experimental setup is not very well suited for angular measurements, as it does not allow for independent variations of the incidence

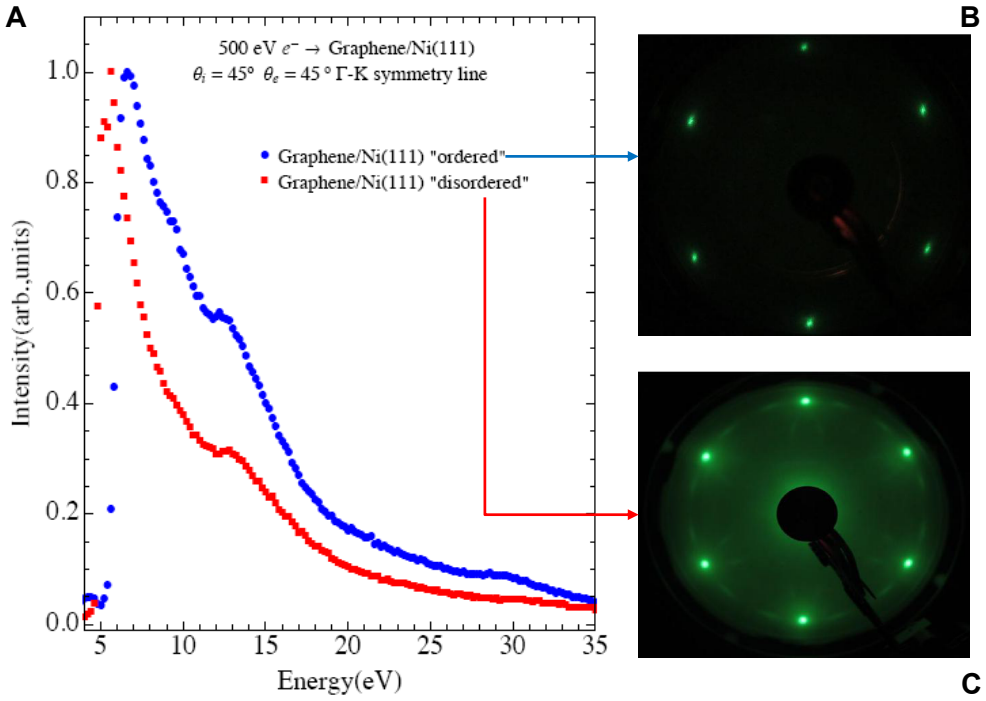

Figure 4.3: *Panel* ***A***: Comparison between the electron emission spectra obtained with the same experimental geometry from two different Graphene/Nickel samples and different deposition results; the spectra are normalized to the same height. In *Panel* ***B-C*** we show the LEED patterns obtained from the two samples.

and emission angles, the modifications that we observe in the spectra are significant. First of all we can observe that the spectrum acquired with $\theta_i = 55°$ and $\theta_e = 35°$ (blue triangles) is narrower than the one with $\theta_i = 45°$ and $\theta_e = 45°$ (red circles). Indeed the former is more intense (it is not reflected in the figure because of the normalization). This is a direct consequence of the more intense cascade peak in the former situation due to the incidence angle of the primary electrons. A big incidence angle with respect to the surface normal means that the incident electrons penetrate less inside the sample and that the cascade of collision is generated near to the surface. Secondly, we can observe that the fine structure is present in both the spectra but the peaks appear shifted in the two configurations and the shift is not rigid.

Summarizing, we can say that the absorption of the Graphene over the Nickel (111) surface induces significant changes in the emission spectrum. In particular we observed a series of peaks superimposed to the cascade peak background. Our experiments demon-

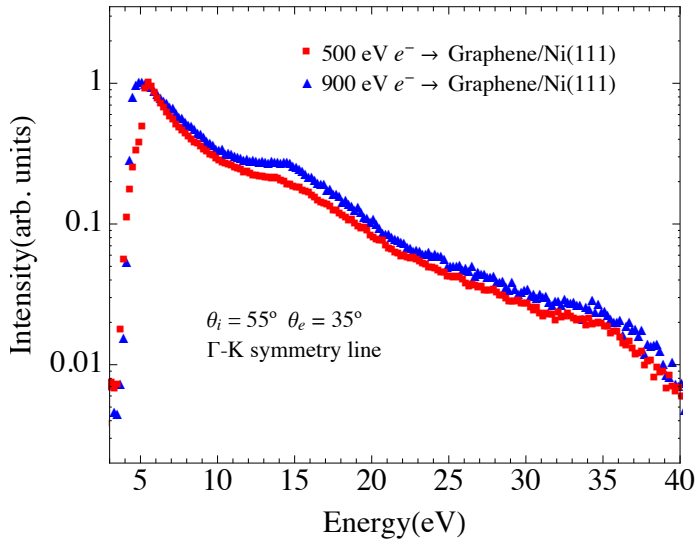

Figure 4.4: Comparison between the electron emission spectra obtained from the Graphene/Nickel sample using two different primary electron energies, namely $E_p = 500$ eV (red squares) and $E_p = 900$ eV (blue triangles). In both cases the electron beam impinged on the surface at 55° with respect to the surface normal on the **ΓK** direction. Electron were collected at 35° along **ΓK**. The spectra are normalized to the same height to compare line shapes. The vertical axis has a logarithmic scale.

strate that these peaks are very sensitive to the crystallographic order of the surface that is a very important point, and suggests that secondary electron emission can be used also to monitor the quality of the growth process. Then we observed that the fine structure is independent on the primary beam energy, while it exhibits a strong dependence on the experimental geometry.

This last point suggested us to carry out a systematic study of the dependence of the fine structure on the experimental geometry. In figure 4.6 we show the results of our observations. We can see that changing the experimental geometry results in very different spectral fine structures. As stated previously some of these peaks are very difficult to resolve from the cascade peak. Nevertheless, we can clearly identify other structures and some of them show a remarkable "dispersion" with the emission angle.

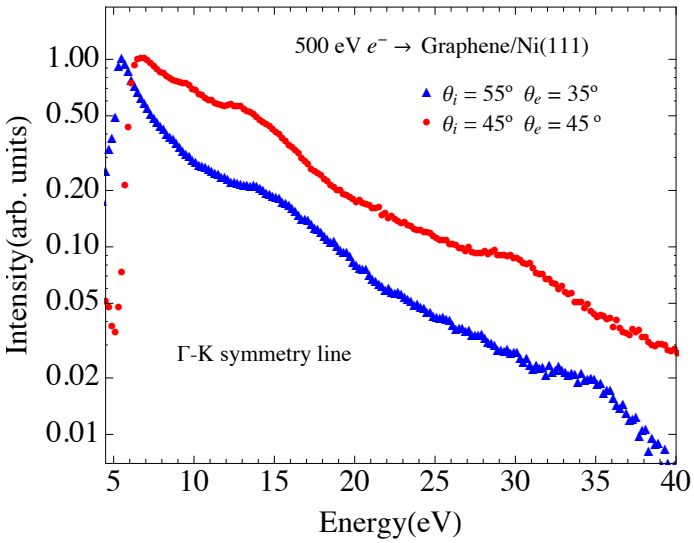

Figure 4.5: Comparison between the electron emission spectra of Graphene/Nickel excited by 500 eV primary electrons, using two different experimental geometries: blue triangles $\theta_i = 55°$ and $\theta_e = 35°$; red circles $\theta_i = 45°$ and $\theta_e = 45°$. In both cases the angle is measured with respect to the surface normal along the **ΓK** direction. The spectra are normalized to the same height to compare line shapes. The vertical axis has a logarithmic scale.

4.3.2 Origin of the fine structure

The observations of the previous section allow us to state that the fine structure is related to the empty states of the system. During the collision cascade electrons are excited into unoccupied electronic states above the vacuum level. From these states the excited electrons emerge into vacuum creating the series of peaks that constitutes the fine structure, reflecting the maxima of the density of unoccupied states. This attribution explains the angular dependence of the peaks and indeed was already observed in Silicon [68] and in graphite [69, 11]. In our case, thanks to the comparison of figure 4.1, we can conclude that Angle Resolved Secondary Electron Emission (ARSEE) is capable of map out the empty bands of Graphene.

Using the angle resolved spectra of figure 4.6 and the free electron dispersion relation for the emitted electrons we can calculate the parallel component $k_{\parallel}$ of momentum of the

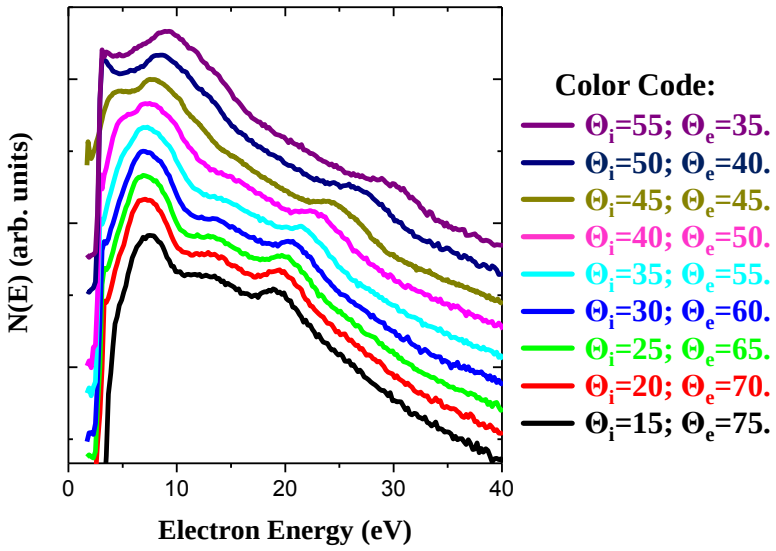

Figure 4.6: Comparison between Graphene/Nickel electron emission acquired with 500 eV primary energy and different experimental geometry (see the inset for the color code). All angles are measured with respect to the surface normal; the incident beam and the emitted electron lie on the **ΓK** symmetry line. The vertical axis has a logarithmic scale. The spectra are normalized and displaced vertically for clarity. The energy axes origin is the same for all the spectra.

emitted electrons as:

$$k_{//} = \sqrt{\frac{2mE}{\hbar^2}} \sin\theta_e \tag{4.1}$$

where E is the energy of the emitted electron with respect to the vacuum level (kinetic energy) and m_e is the electron mass. If we use equation (4.1) we can calculate the dispersion of the structures observed in figure 4.6 that is the dispersion of the excited states of the system graphene/Ni(111); such a dispersion is shown in figure 4.7. To do so, however, we need to measure carefully the energy and to reference it to the Vacuum level. We can do it by measuring the energy of one of the Nickel or Carbon Auger lines; this procedure results in an uncertainty on the measured energy of roughly 1 eV. This value is comparable with the uncertainty on the maximum of the fine structure peaks as it is clear from figure 4.6. In figure 4.7 the points are taken as centers of each fine structure peak. $k_{||}$ is calculated using (4.1) and the energy of the peak referenced to the Vacuum level, using a work function $\phi = 5.1$ eV, while the vertical axis in figure 4.7 has its origin on the Fermi level.

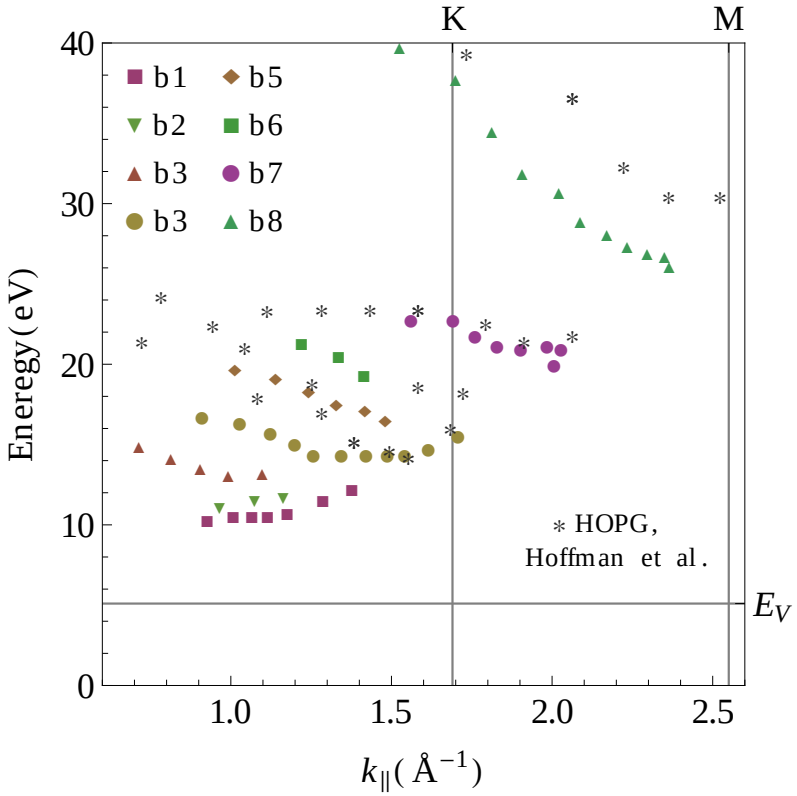

Figure 4.7: Fine structure peaks dispersion. The origin of energy axis is set to the Fermi level, also the vacuum level $E_V = 5.1$ eV is indicated. $k_{\|}$ is along the **ΓK** direction; high symmetry points are indicated in the upper horizontal axis. The obtained data are compared with ARSEE data from HOPG [11], corrected to take into account a work-function of 4.6 eV for HOPG. The naming of the bands b1-b8 will be used in the analisys.

As anticipated before, in figure 4.7 we can see some structures that exhibit an important dispersion with $k_{\|}$ and other nearly flat bands. Our result is compared with some ARSEE measurements on Highly Oriented Pyrolytic Graphite (HOPG) by Hoffman et al. [11]. We can see a reasonable agreement between the two sets of experimental data, that are taken from similar materials. It should be stressed that in both cases the measurement uncertainties are very big.

Very recently emission from few-layer Graphene grown on SiC has been studied [70] under the assumption that the thickness of the sample does not produce significant attenuation either in the incoming beam or in the secondary electrons ejected from the substrate. Under the same assumptions, the only expected effect would be a variation of the escape probability due to the variation of the work function [70] that is similar to the case of the

adsorption of sub-monolayer quantities of alkali metals on sputter-cleaned metal surfaces [71, 72, 73]. Hence, based only on the increase of the measured work function with the number of Graphene layers, a decrease of emission intensity and a slight distortion of the spectral distribution of secondary electrons have been calculated, starting from an initial distribution typical of Si [70]. The variations in the spectral line-shapes observed in our experiments cannot be ascribed to work function changes, and are not consistent with the assumption that the overlayer has no significant effect on the secondary electrons issued from the substrate. Rather, the reported observations imply that the electronic structure of adsorbed Graphene has an important effect in the transport of secondary electrons. Electrons that succeed in being emitted originate from a collision cascade that is governed by the peculiar electronic structure of the graphitic overlayer, resulting in the observed fine structure.

It is important to remark that a detailed analysis of the spectra requires knowledge of excited states at much higher energy than those covered by existing band-structure calculations for Graphene/Ni(111) [17]. This point will be addressed in the projected density of state calculation of the following section.

4.4 Ab-initio band structure and k-projected density of states

4.4.1 Calculation details

Our *ab-initio* computations begin with a DFT ground state (GS) calculation, within the Local Density Approximation (LDA) [74] for the exchange and correlation part of the total Hamiltonian, as implemented in the ABINIT code [75, 76]. We used the plane wave basis (energy cut-off 25 Hartree), and a norm conserving pseudopotential of Troullier and Martins type [54]. We performed GS calculations for free standing Graphene, two-dimensional (2D) few-layer graphene slabs (2 to 6 layers) and 2D Nickel slabs (up to 7 layers, oriented in the (111) direction), three-dimensional (3D) Nickel and 3D-graphite, and Graphene-Ni(111) interfaces. The 2(3,6)-layer Graphene model are obtained superimposing 2(3,6) Graphene layers with the ABAB stacking of graphite at the graphite interlayer spacing, namely 3.354 Å, see figure 4.8 and section 1.1 for all the crystallographic information. As for the Graphene-Nickel interface, we used Nickel (111) slabs of different thickness (up to 7 layer) by placing the two inequivalent C atoms on top of the outmost Ni layer and in the fcc

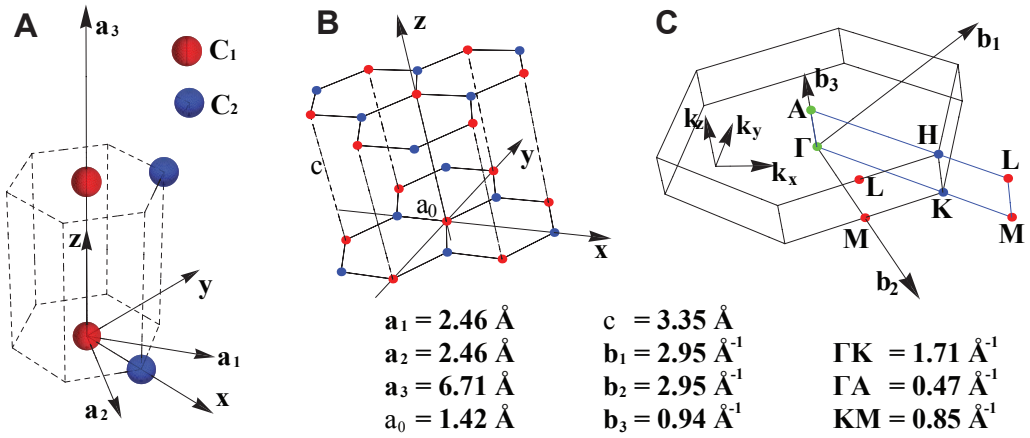

Figure 4.8: **A**: 3D unit cell and lattice vectors of Graphite; there are four atoms per unit cell. Each carbon layer has two inequivalent atoms C_1 and C_2.
B: AB stacking of graphite, C_1 atoms are stacked one on top of the other in the z direction C_2 atoms are not.
C: 3D Brillouin Zone and reciprocal lattice vectors of Graphite, the position of the high symmetry points encountered in the calculation is highlighted.
Inset: Values of some of the lengths shown, a_0 is the smallest carbon-carbon distance, while c is the graphite interlayer distance.

hollow sites of the surface, following the calculation by Bertoni et al. [17]. The separation distance between the repeated system in the perpendicular direction (slab cases) was large enough to exclude interactions between the replicas, keeping constant the total volume. We adopted a vacuum distance larger than 30 Å. Brillouin Zone (BZ) integration was performed on unshifted 50×50 Monkhorst-Pack [36] grids in the irreducible BZ, which correspond to a 2551 full-BZ k-point sampling in 2D systems, while we used unshifted $36 \times 36 \times 12$ and $30 \times 30 \times 17$ samplings in bulk Graphite and bulk Nickel calculations, respectively. The converged electron density was finally used to calculate the one electron eigenstates and eigenvectors on selected k-points along the **ΓK** direction.

4.4.2 k-projected density of states

Our band structure calculation are in very good agreement with calculation found in literature, see for instance [77]. However previous calculations were focused on the energy region close to the Fermi energy, while our main purpose is the calculation of unoccupied electronic states up to 40 eV above the Fermi level. The calculated band structure of

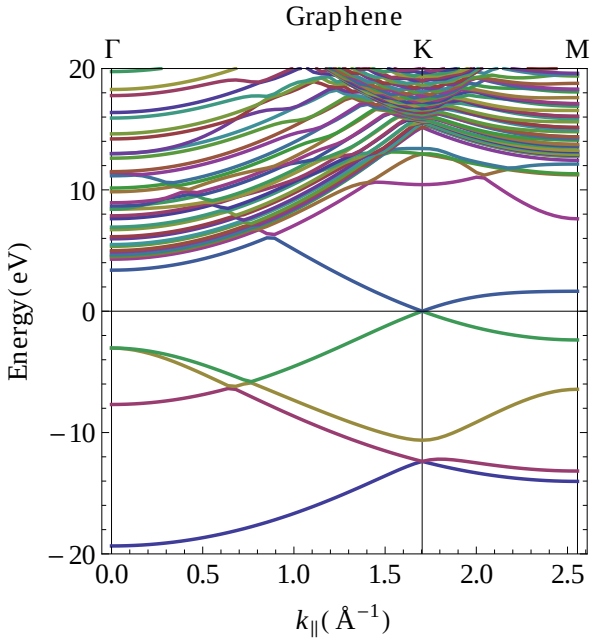

Figure 4.9: Calculated energy bands of graphene. The graph covers all the **ΓK** line up to the **M** point. The Fermi level is set to energy 0.

Graphene in figure 4.9 shows the typical Dirac cone formed by the π bands at the Fermi level (set to 0 energy) at the K point. The empty part is composed by a quasicontinuum of states starting at about 4 eV with a parabolic-like dispersion with $k_{\parallel}$ on which are superimposed states with defined symmetry [78].

The comparison of the experimental secondary electron emission data with the band structure of figure 4.9 is quite difficult, rather we can construct a k-projected density of unoccupied states. The construction is as follow: for a selected k-point k_0 and a given energy E_i we count the number of eigenenergies $N(E_i)$ inside the energy interval $E_i - dE/2 \div E_i + dE/2$; to each point of such an histogram is added a gaussian broadening; we use $dE = 0.1$ eV and a broadening of 0.5 eV.

In figure 4.10 we show a false color plot of the k-projected density of states (k-DOS) obtained with the outlined procedure. The brighter regions mark the high density points. As can be seen from the graphic, the quasicontinuum of states of figure 4.9 of the empty bands is still present, however 5 high density bands that show a parabolic dispersion with $k_{\parallel}$ dominate the plot. These bands are nothing but 2D free-electron-like states resulting from the geometry of the lattice. As a comparison in fig. 4.10 we show also (red dashed lines) the free electron band for a 2D wavevector plotted in the reduced-zone scheme,

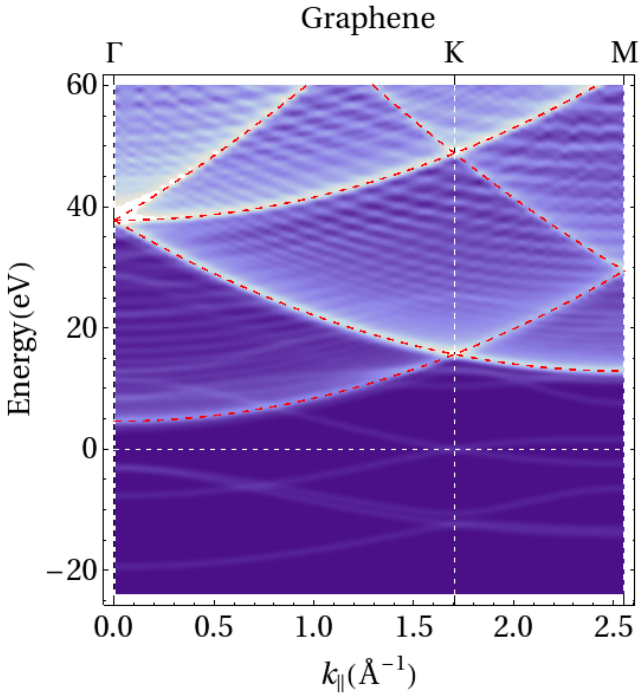

Figure 4.10: False color plot of the calculated k-projected density of states for graphene, brighter parts mark higher density points. The red dashed lines are 2D free-electron-like bands, calculated with (4.2).

obtained from (4.2)

$$E(k_{\parallel}) = \sum_{\mathbf{G}} \frac{\hbar^2}{2m}(\mathbf{k} - \mathbf{G})_{\parallel}^2 + \phi \tag{4.2}$$

where $\mathbf{G}$ is a reciprocal lattice vector, the subscript $\parallel$ stands for the vector parallel component to the $\mathbf{\Gamma K}$ direction, and $\phi = 4.6$ eV is an offset representing the distance between the Fermi level and the vacuum level. This observation is reinforced by the fact that the same free-electron-like parabolas are present in the calculation of a slab of a different material with the same 2D lattice, for instance a one-layer-thick Nickel (111) slab. It is worth noticing that, beyond the 2D parabolic bands, the typical Graphene symmetry features [78] are still present and visible.

4.4.3 Application to Graphite

As previously stated, there is a lack of experimental measurements of the empty states of Graphene, instead the empty bands of graphite have been intensely studied for about thirty years with different techniques such as Angle Resolved Photoelectron Spectroscopy

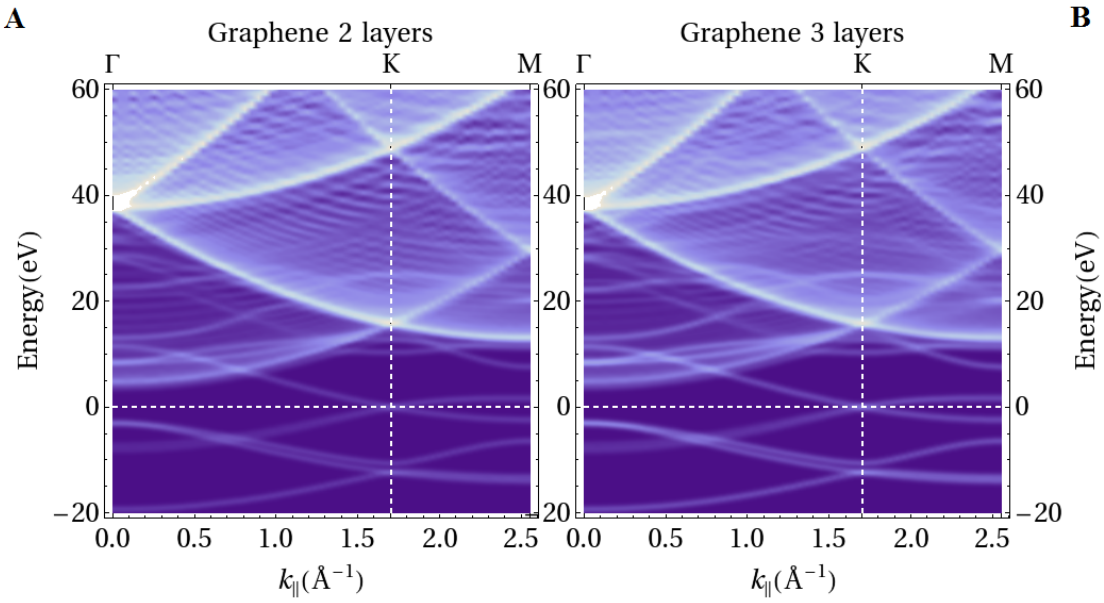

Figure 4.11: False color plot of the calculated k-projected density of states for graphene bilayer, panel **A**, and tri-layer, panel **B**(see text), brighter parts mark higher density points.

(ARPES)[10, 79, 80], Angle Resolved Secondary Electron Emission spectroscopy (ARSEE) [69, 9, 81, 80, 11], Inverse Photoemission (IP) [9, 82, 83], and Target Current Spectroscopy (TCS) [9, 82, 83]. All these techniques are capable to map the density of unoccupied states, so we can apply the previously outlined procedure to graphite.

Before going further to the analysis of the experimental data taken from literature it is worth doing a comparison between different calculations to see the 'transition', if any exist, between a pure 2D material, like a Graphene sheet, and a bulk material, like graphite. This comparison is carried out in figure 4.11 and 4.12, where we show the same calculation as the one in figure 4.10 applied to Graphene bi-layer, tri-layer, 6-layer, and to bulk graphite.

Figure 4.11 shows the k-DOS for bilayer Graphene (panel **A**) and trilayer Graphene (panel **B**). A comparison to figure 4.10 shows that in both cases we can identify the same features present in Graphene, ie the 2D parabolic bands are the most visible structures, while the other Graphene typical features seem to increase with the number of layers, suggesting that they are in fact typical of the graphitic carbon layer.

This behavior is clearer in the case of 6-layer Graphene (figure 4.12**A**), where the 2D parabolic bands are still visible, but the layer feature are as intense as the parabolic ones.

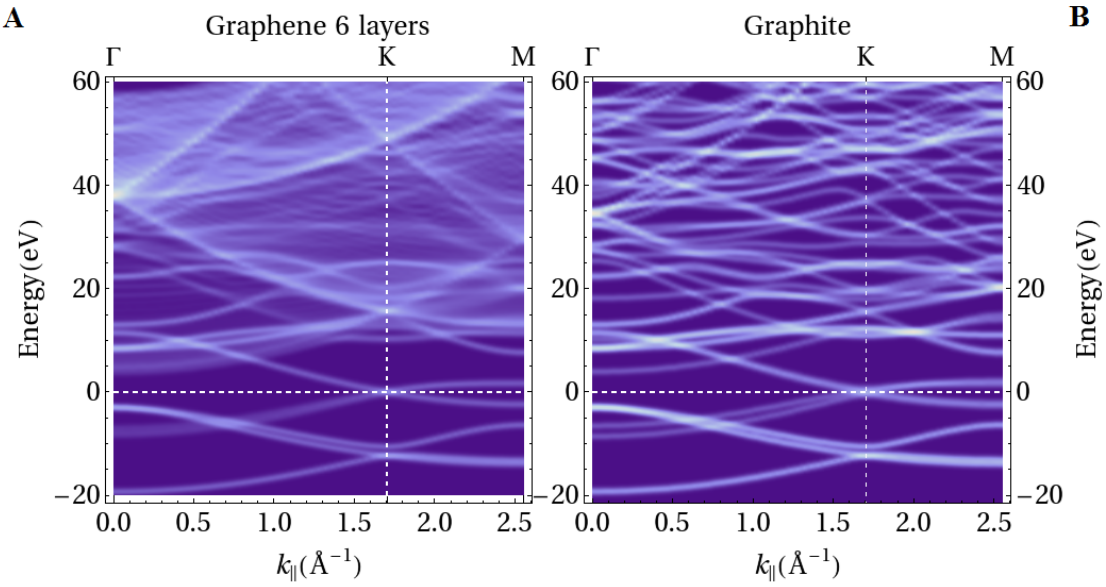

Figure 4.12: False color plot of the calculated k-projected density of states for 6-layer graphene, panel **A**, and bulk graphite, panel **B**; brighter parts mark higher density points.

To complete the analysis we calculate also the band structure and the k-DOS of bulk graphite, the **ΓKM** plot appears in figure 4.12**A**. The comparison of the 6-layer Graphene k-DOS with the graphite one shows, first of all, that the 2D parabolic states are not present in bulk graphite More importantly, we can observe that the carbon layer features, clearly visible in the 6-layer-Graphene case, are also present in the graphite plot, suggesting that they are indeed graphite bands; in particular, a calculation of the k-DOS along other directions in the BZ shows that they can be associated with graphite bands that do not show a significant dispersion with $k_{\perp}$, reinforcing the conjecture that they are related to the graphitic carbon layer. Finally we notice that the free-electron-like parabolas are quite invisible if we calculate the k-DOS for 9-layer Graphene. So we can conclude that the Graphene 6 layer calculation represent a good compromise between the bulk graphite properties and the surface properties, represented by the 2D parabolic states found in the slab calculations.

At this point we can come back to the analysis of the experimental data on graphite. Recently Mahata et al. [10] have reported some ARPES measurements where they were able to map some empty states of HOPG and single-crystal graphite and compared their results with a selection of other measurements obtained with other experimental techniques

like IPS [83], TCS [82], VLEED [84], and the first principles calculation by Tatar and Rabii [85].

The interpretation of the empty bands obtained with different experimental techniques is difficult for many reasons. First of all some structures detected with one technique is not observed with another one, see for example [9]; this is usually addressed to the different physical principle at the base of each technique. Another problem is the determination of $k_{\|}$. For a free electron it can be calculated by

$$k_{\|} = (2mE/\hbar)^{1/2} Sin\theta_e \tag{4.3}$$

where θ_e is the emission angle with respect to the surface. However to use (4.3) we need to define a reference level for the energy scale. The choice of the reference is not unique. In the case of an experimental technique where electrons are emitted, such as ARPES and ARSEE, one can use the Fermi level of the sample which is an absolute choice (for metallic samples) only if the sample is grounded, otherwise sample and spectrometer will have different Fermi levels; however also in this case there is an ambiguity in the choice of the point in energy to start the free electron parabola for the calculation of (4.3), since the vacuum level of grounded sample and spectrometer are, in general, different. Finally, as it is clear from [10], all the techniques used have very large error bars. All these difficulties are highlighted by the fact that all the results found in literature, albeit consistent, are not in very good agreement with one another.

With this in mind we can start analyzing the experimental data for graphite available in literaurte. We use the ARPES experiments by Mahata et al. [10] and the ARSEE experiments by Hoffman et al [11] and by Maeda et al. [9]. For our comparison we us the calculation on Graphene 6 layer, as we saw that it encloses both the bulk graphite features and the parabolic bands. The comparison appears in figure 4.13. We see that the calculation for the 6 layer Graphene reproduces the spectroscopic features that have been observed in experiments of electron emission from bulk graphite, including also the anomalous bands reported recently in ARPES experiments on HOPG by Mahata et al. [10]. On the other hand, the 2D parabolic bands are those observed in photoemission experiments on Graphene layers grown on SiC reported by Hibino et al. [86].

4.4.4 Application to Graphene adsorbed on Ni(111)

Once we verified that our approach was fruitful in the interpretation of graphite experimental measurements we can turn to the Graphene/Nickel system that is the main goal

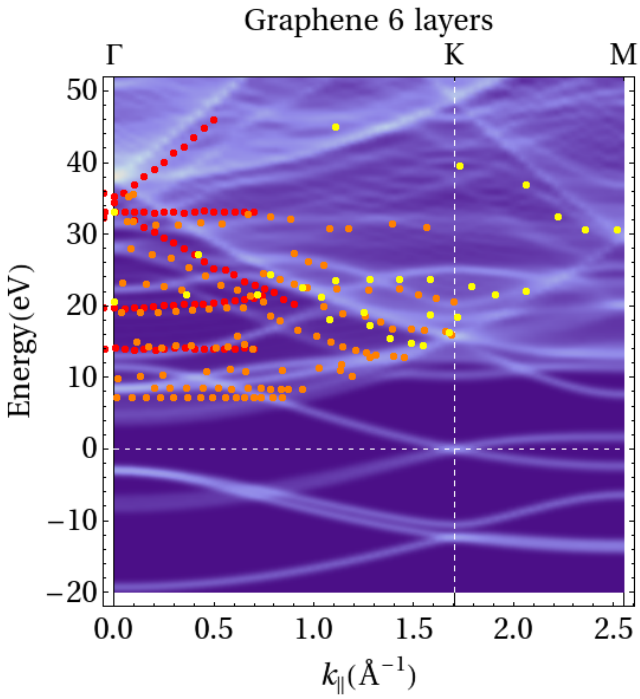

Figure 4.13: False color plot of the calculated k-DOS for 6-layer graphene, compared with three sets of experimental data taken from literature: Red: ARPES data by Mahata et al. [10]; Orange: ARSEE data by Maeda et al. [9]; Yellow: ARSEE data by Hoffman et al. [11] corrected to include a work function of 4.6 eV.

of our work.

In figure 4.7 we reported the dispersion of the fine structure observed in secondary emission spectra from Graphene Nickel, ascribing the fine structure to empty bands of the system and comparing it to the ARSEE results by Hoffman et al. [11]. Now we can compare those points with the k-DOS calculation of Graphene Nickel. To better understand, however, we plot the data of figure 4.7 also on the calculation for monolayer Graphene fig. 4.14**A**, 6 layer graphene fig. 4.14**B**, a 5 layer Nickel slab fig. 4.15**A**, and the system Graphene/Nickel 5 layers fig. 4.15**B**.

As already evidenced in figure 4.7, we can identify 8 bands. We already noticed that the Graphene k-DOS plot was dominated by the parabolic quasicontinuum that renders very difficult a comparison with the dispersion data. We move to the graphitic case 4.14**B**, well described by the 6-layer Graphene calculation as evidenced in the previous section. The band (see inset in figure 4.7 for the names) b1, b2, b4-b7 find correspondence in the calculation and in the experiments performed on graphitic samples. b5 and b6 can

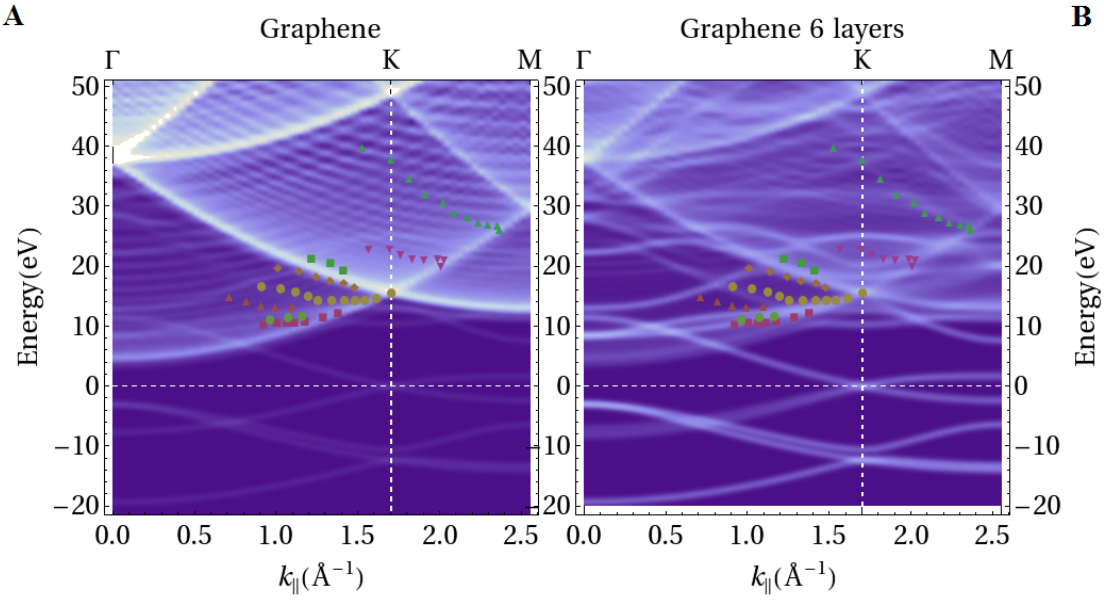

Figure 4.14: Comparison between the fine structure dispersion in figure 4.7 and the k-DOS calculation for graphene (panel **A**) and 6-layer Graphene (panel **B**).

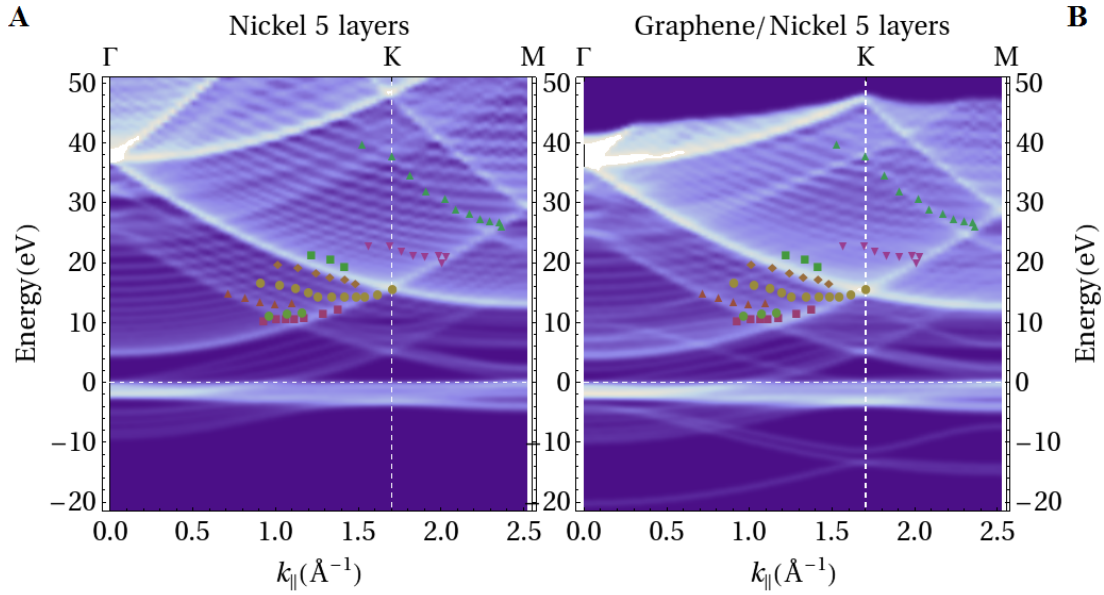

Figure 4.15: Comparison between the fine structure dispersion in figure 4.7 and the k-DOS calculation for a 5-layer Nickel slab (**A**) and the system graphene/Nickel 5 layers (**B**).

be ascribed either to a 2D parabolic band or to a graphitic band that overlap in this region. The comparison in fig. 4.15**A** shows that b8 is peculiar of the Nickel system, either slab or bulk calculation. Finally b3 finds no correspondence in either Graphene, graphite and Nickel bulk, while appears in Nickel slab calculation and is enhanced in the system graphene/Ni(111).

4.5 Conclusions

Summarizing, we measured secondary electron emission spectra from Graphene adsorbed on a Nickel (111) surface. We saw that the adsorption of the Graphene overlayer induces significant changes in the secondary emission lineshape of Nickel. In particular we observed a series of peaks superimposed to the cascade peak. This fine structure showed to be sensitive to the crystallographic order and radiation damage, suggesting secondary electron emission as a tool to study the quality of the produced Graphene overlayer. Moreover the fine structure proved to be independent on the primary electron beam energy, while showed an important angular dependence. These observations suggested us to perform a systematic study of the peak dispersions with the emission angle and allowed us to conclude, consistently with existing literature, that the fine structure is connected to the empty states of the system. As a consequence our secondary electron emission experiments allowed us to map the empty bands of graphene/Ni(111). To complete our analysis we made a DFT calculation of the band structure of the system. We decided to study first the graphite case to take advantage of the vast amount of data available in literature. In particular we chose the datasets regarding secondary electron emission Maeda et al. [9] and by Hoffman et al. [11] and the photoemission spectroscopy data by Mahata et al. [10]. After our ground state DFT calculation we constructed a k-projected density of state for graphitic system and, our approach, though very simple, proved to be very fruitful in the reproduction of the experimental data. Then we moved to Graphene adsorbed on Nickel, performing an equivalent analysis and we found a good agreement between our calculation and the experimental data taken from our secondary electron emission experiments. In particular we were able to identify graphitic states, and Nickel states. This point is particularly interesting, because the Nickel features were much weaker and somehow hidden in the cascade peak before the adsorption of the Graphene sheet that seems to act as an enhancing factor for the emission from Nickel states. More insight into this problem can be achieved performing a deeper study also on the clean Nickel substrate.

Chapter 5

Electron energy Loss calculations on Graphene and Graphene adsorbed on Ni(111)

This chapter is devoted to develop a technique that allows to calculate ab-initio the energy loss function starting from a Density Functional Theory (DFT) based ground state calculation. The theory relies on many body perturbation theory, as given in ref [87], and its application to surfaces and surface like materials [88]. The illustrated theory is first applied to freestanding pristine Graphene, obtaining results fully consistent with existing measurements and calculations; then the doped Graphene loss function is calculated, taking into account the effect of injection of electron and holes in the system; finally we analyze Graphene adsorbed on Nickel, representing an example of strong interaction between Graphene and the supporting substrate.

5.1 Introduction

Electron energy loss spectroscopy (EELS) is a high sensitive method for characterization and investigation of solid surfaces and surface like objects, such as Graphene and Graphene adsorbed on metal surfaces. To this extend, the Graphene-surface interactions play a fundamental role, distinguishing between weak bonding and strong bonding. In this chapter we apply a DFT-based approach, called Time Dependent Density Functional Theory (TDDFT), to calculate the loss function of doped freestanding Graphene and Graphene adsorbed on a Nickel (111) surface: the former is applicable to weak interaction Graphene/substrate, while the latter represents a paradigmatic examples of strong bonding.

In the case of weak bonding, the typical band structure of Graphene, in particular the conical Dirac point, is preserved. Graphene is called quasi-freestanding and the main effect is the charge exchange between the supporting material and Graphene, having as a consequence the production of a shift in the Fermi level, observed also in doped freestanding Graphene. Actually the Fermi level shift can be ascribed to different causes like, shape and defect of the Graphene flake, charge transfer with the supporting material [89], chemical doping [90], application of a gating potential [12]. This point is receiving particular interest for the technological applications of Graphene, especially in the raising Graphene based electronics [91], where the device engineering preserving the conical Dirac point can be a very important task. The insertion of electron or holes is reflected in the loss function, where it is produced an intraband plasmon resonance, observed experimentally on Graphene adsorbed on several surfaces [92, 93, 94, 95, 96] and predicted by some Tight Binding based calculations [97, 98, 99]. On the contrary, our calculation shows two distinct intraband plasmon resonances due to the anisotropy of the band structure near the Dirac point, one of them has not been experimentally observed yet.

In the case of strong bonding the strong Graphene-substrate interactions destroy the conical Dirac-point band structure leading to a more complicated picture. Anyway a loss function calculation for Graphene adsorbed on Nickel (111) is interesting, because this system is one of the most studied Graphene-metal interfaces due its promising application in the production of large and good quality Graphene monolayers [15]. The strong interaction in this case are mainly due to the hybridization between the carbon p and the Nickel d orbitals. As a consequence the effect is reflected in the distortion of the Graphene π plasmon, as observed in two recent works [100, 101].

The chapter is organized as follows. In section 5.2 we review how the screening problem of an electron gas is treated in a perturbation theory framework, and how the screening properties are related to the excitation spectrum of a system and to the electron energy loss spectrum. We also describe a technique that allow to treat the screening within a Density Functional Theory framework and consequently to calculate ab-initio the energy loss function of a system. Then, in section 5.3, we apply the theory developed in section 5.2 to calculate ab-initio the energy loss function of Graphene. We concentrate on the case of freestanding Graphene and include also the effect of doping, i. e., the effect on the loss function induced by the injection of electrons or holes in the system. Finally in section 5.4 we calculate the loss function for Graphene adsorbed on a Nickel (111) surface, simulated by a Graphene sheet adsorbed on a 1, 2 or 3 layer thick Nickel slab.

5.2 Theoretical basis

To construct a theoretical model for the energy loss of an electron moving inside matter we start with a simple picture. We can imagine the electron approaching a solid surface, and eventually entering it, with a kinetic energy E_0. Along his path, the electron interacts with the particle that make up the solid through the Coulomb interaction, suffering both elastic and inelastic scattering. The elastic scattering causes the electron to change its direction, while inelastic scattering causes it to loose part of its kinetic energy, creating excitations in the solid. So we can imagine the electron as being a potential $V_p(\mathbf{r}, t)$ that depends on space and time, because we are dealing with a moving electron, perturbing the electrons of the solid, that we can imagine in its ground state. One can think to handle this problem by the usual time dependent perturbation theory, however it turns out that it is far too complicated because of the very high (in principle infinite) number of particle to take into account and because of the complicated many body interaction between them.

The problem can be simplified if we assume that the perturbation V_p, that the incoming electron exerts on the solid electrons, is weak compared to the electron-electron interactions inside the solid. This allow us to use the linear response theory [102, chapter 6], [103, Chapter 3], [43, Chapter 13]. In the linear response theory, the effect of the external perturbation in the system is given in term of a response function that is independent on the inducing perturbation, being a property of the unperturbed system itself.

The main result of the linear response theory is the Kubo formula. If the external perturbation is coupled with the observable whose operator is $\hat{B}$ (i. e. we write $V_p(t) =$

$F_t\ \hat{B}$, with F_t a complex number) and we want to know the effect that the perturbation has to the observable whose operator is $\hat{A}$, the Kubo formula states that the variation of the mean value $\langle \hat{A} \rangle$ is given by [103, Page 116]:

$$\Delta A_t = \langle \hat{A} \rangle_t - \langle \hat{A} \rangle_0 = -\frac{i}{\hbar} \int_{-\infty}^{t} dt' F_{t'} \left\langle \left[\hat{A}(t), \hat{B}(t') \right] \right\rangle_0 \tag{5.1}$$

where the $\langle\ \rangle_t$ is the expectation value taken at the time t when the perturbation is on, $\langle\ \rangle_0$ is the expectation value on the unperturbed system, $[\hat{A}, \hat{B}]$ is the usual commutator between the operators $\hat{A}(t)$ and $\hat{B}(t)$ in the Heisemberg representation with the perturbation off. As it is clear in (5.1) in the linear response framework the perturbed quantity is calculated by means of unperturbed expectation values.

In our case, the perturbation induced by the incoming electron is coupled with the charge density of the system and we are interested on the modification induced by the electron on the charge density of the system, so we are interested in the density-density response function of our system.

This effect is similar to the macroscopic screening of a test charge in a system by the other free charges of the system. Indeed we can imagine the space- and time-dependent potential as induced by a moving test charge inside or in the vicinity of the electron gas made up by the quasi-free electron of the system. With this observation we can introduce a dielectric function ϵ, that takes into account the microscopic response of the electrons, in analogy to the classical dielectric theory.

5.2.1 Dielectric Function ϵ

We can define the Dielectric function starting from the classical relations for the electric field and the electric displacement in a dielectric medium[87]:

$$\nabla \cdot \mathbf{D} = 4\pi \rho_{ext} \qquad \nabla \cdot \mathbf{E} = 4\pi \rho_{tot} \tag{5.2}$$

with ρ_{ext} the external charge density and introducing the total charge density $\rho_{tot} = \rho_{ext} + \rho_{ind}$ as a sum of the external charge and the induced charge in the medium by the external electric field. At this point we assume[1] that the induced density is proportional to the electric displacement $\mathbf{D}$, that, in fact, means assuming that the induced density is proportional to the external density, $\rho_{ind} \propto \rho_{ext}$. This means that the electric field is

[1] This assumption is fully consistent with linear response regime.

proportional to the electric displacement so that we can write the classical relation:

$$\mathbf{E} = \epsilon^{-1}\mathbf{D}. \tag{5.3}$$

We can use the dielectric constant ϵ to write a relation between the charge densities, consistent with (5.2) and (5.3), $\rho_{tot} = \epsilon^{-1}\rho_{ext}$, and, more importantly, between the potentials generated by the charge densities:

$$\phi^{tot} = \phi^{ext} + \phi^{ind} = \epsilon^{-1}\phi^{ext}. \tag{5.4}$$

All the above equations can be generalized to the case of position- and time-dependent quantities, introducing a position- and time-dependent dielectric function $\epsilon(\mathbf{r}, \mathbf{r}', t, t')$, or, in the frequency domain, $\epsilon(\mathbf{r}, \mathbf{r}', \omega)$[2]. Equation (5.4) is then generalized to:

$$\phi^{tot}(\mathbf{r}, \omega) = \int d^3r' \epsilon^{-1}(\mathbf{r}, \mathbf{r}', \omega)\phi^{ext}(\mathbf{r}', \omega). \tag{5.5}$$

It can be demonstrated that the dielectric function can be related to a quantity, called spectral density S, that is directly related to the elementary excitation of the "disturbed" quantity [103], in our case the density. We recall that the loss function we are looking for is made up of the energy loss by the electron to excite the electron density of the solid.

Up to now we have defined the dielectric function (5.5) and stated its importance, however we still need a model to calculate it, that includes the microscopic effect of the electron gas. It is worth noticing that it is not possible to calculate exactly ϵ [44], not even in the case of the electron gas, so approximations are necessary. It turns out that, as in the classical dielectric problem, in linear regime, we can introduce a function equivalent to the classical susceptibility χ. This function is nothing but the aforementioned density-density response function, as we will see. In the next section we introduce this response function and its link to the dielectric function. We start defining our χ as the linear response of the density to the external potential, so we call it density response function [88].

From the next section on we will adapt the notation so that the electron density, rather than the charge density, enters in all our equations. To do so we need to include the electron charge consistently in the definition of the densities and potentials; we assume that this process is carried out through the transformation $\phi \to \varphi$ and $\rho \to n$.

[2]Going from the time to the frequency domain we assume that the dielectric function is local in time, that is $\epsilon(\mathbf{r}, \mathbf{r}', t, t') = \epsilon(\mathbf{r}, \mathbf{r}', t - t')$; this allows us to use the convolution theorem for the Fourier transform, so that all the time integrations become products between functions in the frequency domain.

5.2.2 Density response function χ

We want to calculate the response induced in the electron density n of a many electron gas by an external potential $\varphi^{ext}(\mathbf{r}, t)$, assuming a space- and time-dependent external potential. We can go to the frequency space by a Fourier-transform and analyze directly the ω-Fourier component of the potential $\varphi^{ext}(\mathbf{r}, \omega)$. In what follow all the quantities will be in the frequency domain.

We start writing the total electron density as:

$$n(\mathbf{r}, \omega) = n_0(\mathbf{r}, \omega) + \delta n(\mathbf{r}, \omega), \tag{5.6}$$

where we use the unperturbed electron density $n_0(\mathbf{r}, \omega)$ and we introduced the induced density $\delta n(\mathbf{r}, \omega)$. In the framework of the linear response theory, we have to retain term in the Taylor expansion of the total density (5.6) up to the first order in the external potential, this allows us to write:

$$\delta n(\mathbf{r}, \omega) = \int d^3r' \chi(\mathbf{r}, \mathbf{r}', \omega) \varphi^{ext}(\mathbf{r}', \omega) \tag{5.7}$$

where we introduced the density response function $\chi(\mathbf{r}, \mathbf{r}', \omega)$, that is given by [87]:

$$\chi(\mathbf{r}, \mathbf{r}', \omega) = \sum_m \rho^*_{m,0}(\mathbf{r}) \rho_{0,m}(\mathbf{r}') \times \left[\frac{1}{\hbar\omega - (E_m - E_0) + i\eta} - \frac{1}{\hbar\omega - (E_m - E_0) + i\eta} \right]; \tag{5.8}$$

where the η is an infinitesimal with dimension of energy, and $\rho_{m,0}$ are matrix elements between the manybody excited state $|\Psi_m\rangle$, of total energy E_m, and the many body ground state $|\Psi_0\rangle$, of total energyE_0, of the electron density operator,

$$\hat{\rho}(\mathbf{r}) = \sum_{i=1}^{N_{el}} \delta(\hat{\mathbf{r}} - \mathbf{r}_i), \tag{5.9}$$

where δ is the dirac delta function and $\mathbf{r}_i$ are the electron coordinates of the N_{el}-electron system.

At this point we can find a relation between the density response function and the dielectric function. The latter is indeed defined as:

$$\epsilon^{-1}(\mathbf{r}, \mathbf{r}', \omega) = \delta(\mathbf{r} - \mathbf{r}') + \int d^3r'' v(\mathbf{r} - \mathbf{r}'') \chi(\mathbf{r}'', \mathbf{r}', \omega). \tag{5.10}$$

In (5.10) it is clear that solving the problem of calculating ϵ is equivalent to the problem of calculating χ. However, equation (5.8), even though symbolic, embodies directly the microscopic properties of the electron gas. As it is always the case in many-body physics, equation (5.8) is difficult to evaluate because of the complexity of the many-body wavefunctions inside it; in what follow we introduce and discuss some approximate ways to calculate the density response function.

Random Phase Approximation (RPA)

A first possibility to calculate the density response function (5.8) is given by the Random Phase Approximation (RPA), or time dependent Hartree approximation.

The idea behind the RPA is considering the many-body wave function in the matrix elements in (5.8) as composed by independent one-electron wave functions as in the Hartree approximation. The external potential φ^{ext} induces a perturbation δn in the electron density that creates an induced potential $\delta\varphi$:

$$\delta\varphi(\mathbf{r},\omega) = \int d^3r' v(\mathbf{r},\mathbf{r}')\delta n(\mathbf{r}',\omega), \tag{5.11}$$

where $v(\mathbf{r},\mathbf{r}')$ is the bare Coulomb potential. The induced potential (5.11) is used to calculate the induced density δn self-consistently:

$$\delta n(\mathbf{r},\omega) = \int d^3r' \chi^0(\mathbf{r},\mathbf{r}',\omega)\left[\varphi^{ext}(\mathbf{r}',\omega) + \delta\varphi(\mathbf{r}',\omega)\right]. \tag{5.12}$$

In (5.12) we introduced the independent-electron density response function, $\chi^0(\mathbf{r},\mathbf{r}',\omega)$, that is the response function of the Hartree system with N_{el} independent electrons:

$$\chi^0(\mathbf{r},\mathbf{r}',\omega) = \sum_{i,j}(f_i - f_j)\frac{\psi_i(\mathbf{r})\psi_j^*(\mathbf{r})\psi_j(\mathbf{r}')\psi_i^*(\mathbf{r}')}{\hbar\omega - (\varepsilon_i - \varepsilon_j) + i\eta}, \tag{5.13}$$

where ψ_i and ε_i represent the i^{th} eigenfunction and eigenenergy of the Hartree Hamiltonian[3] and $\{f_i\}$ are the Fermi-Dirac occupation factors. Equation (5.13) follows easily from (5.8), noticing that the many-body ground state $|\Psi_0\rangle$ in the Hartree approximation is the product of the N_{el} lowest energy eigenfunction $\psi_l(\mathbf{r})$, that is $|\Psi_0\rangle = \prod_l \psi_l(\mathbf{r}_l)$, and the

[3]For the Hartree approximation see for instance ref. [104]; the Hartree hamiltonian is similar to the Kohn-Sham hamiltonian introduced in 2.3.1 in which the electron-electron interaction is represented by $V_{Hartree}$ of (2.16) only.

ground state energy E_0 is simply $\sum_l \epsilon_l$, while the m^{th} excited state is the ground state with the i^{th} occupied state substituted by the j^{th} unoccupied state.

Equations (5.11) and (5.12) and (5.7) define the interacting density response function $\chi(\mathbf{r}, \mathbf{r}', \omega)$ with the Dyson type equation:

$$\chi(\mathbf{r}, \mathbf{r}', \omega) = \chi^0(\mathbf{r}, \mathbf{r}', \omega) + \int d^3r_1 \int d^3r_2 \chi^0(\mathbf{r}, \mathbf{r}_1, \omega) v(\mathbf{r}_1, \mathbf{r}_2) \chi(\mathbf{r}_2, \mathbf{r}', \omega). \tag{5.14}$$

The interacting density response function in (5.14) enters (5.10) to give the inverse dielectric function that we can write, shortening the notation, as

$$(\epsilon^{RPA})^{-1} = 1 + v\chi; \tag{5.15}$$

with a little of algebra[4] it is possible to write the following relation for the so called RPA or Lindhard dielectric function [44, 105]:

$$\epsilon^{RPA} = 1 - v\chi_0. \tag{5.16}$$

Time Dependent Density Functional Theory (TDDFT)

The natural generalization of RPA is given by Time Dependent Density Functional Theory (TDDFT). In formulating the TDDFT approach we can follow the same path of the previous section. This time the one electron wavefunctions ψ_i and energies ε_i are the Kohn-Sham quasi-orbital and eigenenergies obtained from the diagonalization of the full KS-Hamiltonian (2.15). The expression for the density response function is generalized to:

$$\chi(\mathbf{r}, \mathbf{r}', \omega) = \chi^0(\mathbf{r}, \mathbf{r}', \omega) + \int d^3r_1 \int d^3r_2 \chi^0(\mathbf{r}, \mathbf{r}_1, \omega) K(\mathbf{r}_1, \mathbf{r}_2, \omega) \chi(\mathbf{r}_2, \mathbf{r}', \omega), \tag{5.17}$$

with the due generalization in the definition of χ_0, and where $K(\mathbf{r}, \mathbf{r}', \omega)$ is given by:

$$K(\mathbf{r}, \mathbf{r}', \omega) = v(\mathbf{r}, \mathbf{r}') + f_{xc}[n_0](\mathbf{r}, \mathbf{r}', \omega) \tag{5.18}$$

with $v(\mathbf{r}, \mathbf{r}')$ the usual bare Coulomb potential and with the introduction of the Exchange-Correlation Kernel $f_{xc}[n_0]$, defined formally by:

$$f_{xc}[n_0](\mathbf{r}, t, \mathbf{r}', t') = \left. \frac{\delta V_{xc}[n](r, t)}{\delta n(\mathbf{r}, t)} \right|_{n=n_0}. \tag{5.19}$$

[4]The calculation is straightforward in the "shortened" notation, however the relation holds also in the "integral" notation of (5.10).

V_{xc} entering (5.19) can be the same used in the DFT calculation performed to get the eigenvalues and wavefunction, eventually generalized to include explicitly the time dependence of the density, but this choice is not compulsory. As in the case of the DFT Hamiltonian, the right xc-Potential and xc-Kernel are unknown so they must be approximated in some way. There are a lot of possibilities in selecting the exchange and correlation kernel:

1. Time Dependent Local Density Approximation (TDLDA) or Adiabatic Local Density Approximation (ALDA) [106], in which f_{xc} is assumed to be the functional derivative of the LDA Exchange-Correlation, that is:

$$f_{xc}^{ALDA}[n_0](\mathbf{r},\mathbf{r}') = \delta(\mathbf{r}-\mathbf{r}')\frac{\delta V_{xc}^{LDA}[n](r,t)}{\delta n(\mathbf{r},t)}\bigg|_{n=n_0}.$$

2. Another common used approximation [107] for the exchange correlation kernel is:

$$f_{xc}[n_0](\mathbf{q},\mathbf{G},\mathbf{G}',\omega) = -\frac{\alpha}{|\mathbf{g}+\mathbf{G}|}\delta(\mathbf{G}-\mathbf{G}')$$

   written directly in the reciprocal space and with α a parameter that depends on the case under study.

3. Random Phase Approximation (RPA) in which the exchange-correlation kernel is set to 0. The difference with the previous section is that the Kohn-Sham orbital and energies are used in χ_0, so the $f_{xc} = 0$ case is sometimes called DFT-based RPA. It should be stressed that nowadays the term RPA approximation is usually referred to the DFT-based RPA of this section rather than the pure RPA introduced in the previous section. In this case it is possible to define an RPA dielectric function as in (5.16).

All the calculations of the next sections are performed in the DFT-based RPA approximation framework.

5.2.3 χ_0 in Fourier space, Adler-Wiser formula

It can be useful to evaluate the Fourier transform of the density response function χ in the wave-vector representation. In the case of a periodic system the main ingredient entering

equation (5.14) or (5.17), the noninteracting density response function χ_0, is given by the Adler-Wiser formula [108, 109]:

$$\chi_0(\mathbf{q},\mathbf{G},\mathbf{G}',\omega) = \frac{2}{\Omega}\sum_{\mathbf{k}}^{1^{st}BZ}\sum_{v,c}\frac{f_{v,\mathbf{k}}-f_{c,\mathbf{k}+\mathbf{q}}}{\hbar\omega-(\varepsilon_{c,\mathbf{k}+\mathbf{q}}-\varepsilon_{v,\mathbf{k}})+i\eta} \times \langle v,\mathbf{k}|\, e^{-i(\mathbf{q}+\mathbf{G})\cdot\mathbf{r}}\,|c,\mathbf{k}+\mathbf{q}\rangle\,\langle c,\mathbf{k}+\mathbf{q}|\, e^{i(\mathbf{q}+\mathbf{G}')\cdot\mathbf{r}'}\,|v,\mathbf{k}\rangle\,; \quad (5.20)$$

where we used the bra-ket notation for the one-electron Bloch wave functions [35]:

$$\langle\mathbf{r}|n,\mathbf{k}\rangle = \phi_{n,\mathbf{k}}(\mathbf{r}) = e^{i\mathbf{k}\cdot\mathbf{r}}u_{n,\mathbf{k}}(\mathbf{r}) \quad (5.21)$$

with the band index n, the Bloch quasi-momentum $\mathbf{k}$, and with $u_{n,\mathbf{k}}(\mathbf{r})$ being the function with the same periodicity of the direct lattice.

Although it is not clear at a first sight, (5.20) is indeed the Fourier transform of (5.14) or (5.17) in the case of a periodic system[5]. It becomes clear, if we observe that a generic function $f(\mathbf{r})$ can be Fourier-analyzed including explicitly the reciprocal lattice vector as:

$$f(\mathbf{r}) = \frac{1}{\sqrt{V}}\sum_{\mathbf{q}}^{1^{st}BZ}\sum_{\mathbf{G}}\tilde{f}(\mathbf{q},\mathbf{G})e^{-i(\mathbf{q}+\mathbf{G})\cdot\mathbf{r}}; \quad (5.22)$$

where the $\mathbf{G}$-s are reciprocal lattice vectors and the $\mathbf{q}$ summation is confined to the first Brillouin zone; we note that the fourier-transform is normalized to the volume. In the case of χ_0 the Fourier components should be (dropping the $\sim$):

$$\chi_0(\mathbf{q},\mathbf{G},\mathbf{q}',\mathbf{G}';\omega) = \frac{2}{\Omega}\sum_{\mathbf{k}_1}\sum_{\mathbf{v}}\sum_{\mathbf{k}_2}\sum_{\mathbf{c}}\frac{f_{v,\mathbf{k}_1}-f_{c,\mathbf{k}_2}}{\hbar\omega-\varepsilon_{c,\mathbf{k}_2}+\varepsilon_{v,\mathbf{k}_1}} \times \langle c,\mathbf{k}_2|\, e^{i(\mathbf{q}_1+\mathbf{G}_1)\cdot\mathbf{r}}\,|v,\mathbf{k}_1\rangle\,\langle v,\mathbf{k}_1|\, e^{i(\mathbf{q}_2+\mathbf{G}_2)\cdot\mathbf{r}'}\,|c,\mathbf{k}_2\rangle\,, \quad (5.23)$$

where Ω is the normalization Volume and the factor 2 comes from the spin degrees of freedom integration. However it is easy to show that the only non-zero components are those with $\mathbf{q}=\mathbf{q}'$ and are given by (5.20). Using (5.21) we have:

$$\langle c,\mathbf{k}_2|\, e^{i(\mathbf{q}+\mathbf{G})\cdot\mathbf{r}}\,|v,\mathbf{k}_1\rangle = \int d^3r\,\underbrace{u_{v,\mathbf{k}_1}(\mathbf{r})u^*_{c,\mathbf{k}_2}(\mathbf{r})e^{i\mathbf{G}\cdot\mathbf{r}}}_{g(\mathbf{r})}\underbrace{e^{i(\mathbf{k}_1-\mathbf{k}_2+\mathbf{q})\cdot\mathbf{r}}}_{h(\mathbf{r})}. \quad (5.24)$$

[5]In the papers by Adler [108] and Wiser [109] χ_0 is derived directly in Fourier space so we can think the other way round, that is equations (5.14) or (5.17) as the Fourier transforms to the direct-space representation of equation (5.20).

We recognize in the integrand of (5.24) a periodic part $g(\mathbf{r})$ with the same periodicity of the direct lattice and an oscillating part $h(\mathbf{r})$; the integration is extended to the volume of the solid. We can imagine that, because of the highly oscillating integrand, the result of the integration would be zero, unless the oscillating part is constant, i.e. $h(\mathbf{r}) = 1$, that requires $\mathbf{k}_1 - \mathbf{k}_2 + \mathbf{q} = 0$, that is

$$\mathbf{k}_2 = \mathbf{k}_1 + \mathbf{q}. \tag{5.25}$$

In (5.23) we have two integrals as (5.24) that give rise to two conditions like (5.25). These two conditions can be put together to give another condition involving the $\mathbf{q}$s. The two conditions are:

$$\mathbf{q}_1 = -\mathbf{q}_2 = \mathbf{q}, \tag{5.26}$$

$$\mathbf{k}_2 = \mathbf{k}_1 + \mathbf{q}; \tag{5.27}$$

and justify the expression (5.20).

One of the main advantages of the Fourier space representation is that all the integrations entering the defining equations of χ, ϵ^{-1} and ϵ_{RPA} become matrix multiplications. Indeed we can imagine χ_0 at a given $\mathbf{q}$ as a matrix (an infinite dimensional matrix), whose matrix elements can be labeled by $\mathbf{G}$ and $\mathbf{G}'$. If we notice that the Fourier components of the coulomb interaction are given by:

$$v_{\mathbf{q}}(\mathbf{G}, \mathbf{G}') = \frac{4\pi}{|\mathbf{q} + \mathbf{G}|^2} \delta_{\mathbf{G},\mathbf{G}'}, \tag{5.28}$$

we can write for the Fourier components of χ and ϵ^{-1}:

$$\chi(\mathbf{q}, \mathbf{G}, \mathbf{G}', \omega) = \chi_0(\mathbf{q}, \mathbf{G}, \mathbf{G}', \omega) + \sum_{\mathbf{G}_1} \sum_{\mathbf{G}_2} \chi_0(\mathbf{q}, \mathbf{G}, \mathbf{G}_1, \omega) v_{\mathbf{q}}(\mathbf{G}_1, \mathbf{G}_2) \chi(\mathbf{q}, \mathbf{G}_2, \mathbf{G}', \omega); \tag{5.29}$$

$$\epsilon^{-1}(\mathbf{q}, \mathbf{G}, \mathbf{G}', \omega) = \delta_{\mathbf{G},\mathbf{G}'} + \sum_{\mathbf{G}_1} v_{\mathbf{q}}(\mathbf{G}, \mathbf{G}_1) \chi(\mathbf{q}, \mathbf{G}_1, \mathbf{G}', \omega). \tag{5.30}$$

The second advantage of the Fourier space representation is that it allows to define some "$\mathbf{q}$-resolved" quantities like the Fourier components in (5.29) and (5.30). To do so we have to "get rid" of $\mathbf{G}$ and $\mathbf{G}'$ form equations (5.29) and (5.30). It can be demonstrated [109] that the $\mathbf{q}$-Fourier component of a macroscopic quantity f is the $\mathbf{G} = 0$ component

of the microscopic expansion (5.22). So the Fourier components of the macroscopic ϵ^{-1} and χ are:

$$\chi(\mathbf{q},\omega) = \chi(\mathbf{q},\mathbf{G}=0,\mathbf{G}'=0,\omega), \tag{5.31}$$

$$\epsilon^{-1}(\mathbf{q},\omega) = \epsilon^{-1}(\mathbf{q},\mathbf{G}=0,\mathbf{G}'=0,\omega), \tag{5.32}$$

This definition is particularly useful because allows to connect the dielectric function ϵ and the density response function χ to the density excitation of the system through the Spectral Density.

5.2.4 Spectral Density, S, excitations and collective modes

We start from the perturbation theory and the Fermi golden rule [87]. As stated before, if we imagine the interaction potential to be coupled to the density of the system (i.e. we write the potential as $V_{\mathbf{q}}\hat{\rho}$, where $V_{\mathbf{q}}$ and $\hat{\rho}$ play the role of F_t and $\hat{B}$ in the definition of the Kubo formula (5.1)) the probability that the external potential exchanges energy ω and momentum $\mathbf{q}$ is given by:

$$P(\mathbf{q},\omega) = 2\pi \left|V_{\mathbf{q}}\right|^2 \sum_m \left|\hat{\rho}_{m,0}\right|^2 \delta(\hbar\omega - (E_m - E_0)). \tag{5.33}$$

In (5.33) we used directly the Fourier transform of the interaction potential assuming that it is local and it is not explicitly time dependent[6]; $\hat{\rho}$, m, 0, E_m and E_0 have the same meaning as in (5.8) and (5.9). It is useful to define a function called Structure Factor or Spectral Density that is independent on the potential as:

$$S(\mathbf{q},\omega) = \frac{P(\mathbf{q},\omega)}{\left|V_{\mathbf{q}}\right|^2}. \tag{5.34}$$

$S(\mathbf{q},\omega)$ contains all the possible excitation mechanisms that involve a response in the system density, whatever the shape of the potential, and is actually the density-density response function we are looking for. Using (5.8) and (5.33) it is clear that S is related to the imaginary part of the density response function χ and hence to ϵ^{-1}. So we can finally close the gap and link the excitation of the system to the macroscopic screening function ϵ (5.32). Now we recall our picture of the projectile impinging on a surface and

[6]This is the case for the Coulomb potential; actually using (5.33) we are assuming that the time dependence appears as a slowly switching on of the potential.

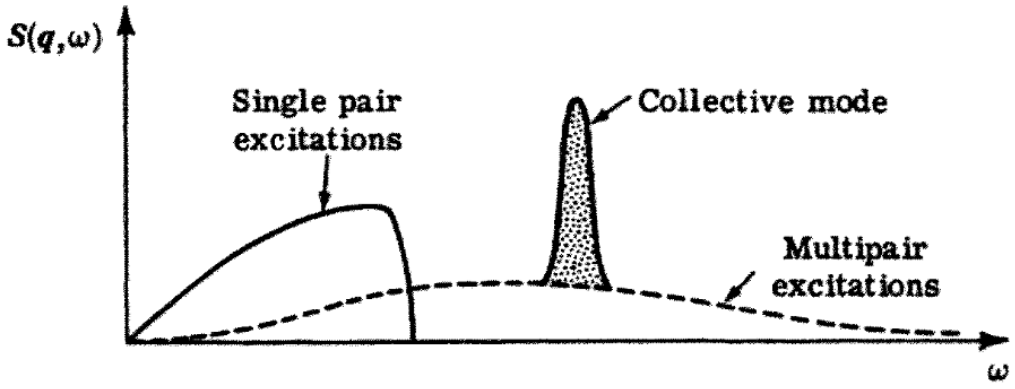

Figure 5.1: Qualitative sketch of the different contribution to the spectral density as predicted by the Landau Theory for the Fermi liquid[87, chapter 2].

we come back to the energy loss of the projectile. Because each excitation of the system is correlated to an energy loss of the projectile we can write:

$$ENERGY LOSS = -\mathfrak{Im}\left\{\frac{1}{\epsilon}\right\}. \tag{5.35}$$

The exact knowledge of the spectral density gives all the possible density excitation of the system and then all the contribution to the energy loss function. These properties are, of course, typical of the system under study; however it is possible to give a qualitative description of the spectral density within the framework of the Landau theory of the Fermi liquids [87]. These theory is valid under some condition that are usually met by systems of interacting electrons.

All the possible contributions to the spectral density can be collected in three categories, single-particle excitations (SPE), multi-particle excitations and collective modes. In figure 5.1 we show a qualitative sketch of the different contribution to the spectral density, as predicted by the Landau theory, in the simple case of electrons occupying a single partially filled band of finite bandwidth.

We start with single particle excitation (SPE), that we can imagine to be the contribution to the spectral density that takes into account the generation of an excitation in which one electron is promoted from its energy level to an excited level, creating an electron-hole pair. In the simple picture of an electron belonging to a single band, with the Fermi level placed somewhere inside the energy band, the SPE spectrum has a finite extent (see figure 5.1), that reflects the bandwidth, while its shape is influenced by the transition matrix elements and by the density of states. In a more realistic situation, the energy structure

of a system is made up by several valence and conduction bands, so the SPE spectrum is more complicated, reflecting the convolution of the density of occupied states and the density of empty states, weighted by the transition matrix elements[7]. We can imagine the SPE spectrum to be related to the response of a single electron as being independent on the other electrons, so it is related to the independent electron response function χ_0. In fact, the optical excitation spectrum, related to the single particle excitation spectrum, is usually [44] calculated as:

$$OPTICAL\ SPECTRUM \propto -\mathfrak{Im}\{\epsilon\} \tag{5.36}$$

In our case we can say that the SPE spectrum is proportional to $-\mathfrak{Im}\{\chi_0\}$, or, equivalently, introducing the Coulomb potential, we have in our case:

$$SPE = -\mathfrak{Im}\{\epsilon^{RPA}\} \tag{5.37}$$

The multi-particle excitation spectrum simply represent the spectral density contribution in which more than one electron is excited at the same time. This part is less intense than the single particle one, but extends from 0 to ∞ also in the simple case of a single finite-width energy band (see figure 5.1).

Finally superimposed to single particle and multi-particle excitations we have the contribution due to collective excitations of the electron gas. As depicted in figure 5.1 collective modes appear as very narrow peaks, having in principle the shape of a Dirac delta. In the case of the electron gas they are associated to electric charge oscillation, so they are called Plasmons. As in the classical plasma oscillation, the plasmon condition is given by the zeros of the dielectric function. In our case the plasmon condition is given by:

$$\text{PLASMON CONDITION:} \qquad \epsilon^{RPA}(\mathbf{q}, \omega) = 0. \tag{5.38}$$

In (5.38) it is meant that both the real part the imaginary part are zero. Equation (5.38) defines the dispersion relation $\omega(\mathbf{q})$ of the plasmon, that appears also as a singularity in ϵ^{-1}.

In figure 5.1 the plasmon is sketched as a narrow but actually finite-width peak, in contrast with the plasmon condition (5.38) predicting the collective modes to be Dirac deltas. Nevertheless the Landau theory predicts a coupling between the collective modes and the single particle and multi particle excitations. This coupling results in the broadening of the plasmon peak that is called Landau Damping. Depending on the coupling,

[7] This is usually called joint density of states.

the plasmon can be over-damped that results in a broadening that renders the plasmon peak indistinguishable from the single particle and multi particle excitation spectrum. In this case the collective mode concept is no longer well defined. From the mathematical point of view, Landau damping due to single particle excitation is present whenever the plasmon mode is in a region where $\mathfrak{Im}\{\chi_0\} \neq 0$, that is the plasmon condition is fulfilled only by the real part of ϵ^{RPA}. Actually, zeros of $\mathfrak{Re}\{\epsilon^{RPA}\}$ occur always in couple, the first one in energy being connected to a peak in $\mathfrak{Im}\{\epsilon^{RPA}\}$, so a Single particle excitation peak, and the second one either in a region in energy where $\mathfrak{Im}\{\epsilon^{RPA}\} = 0$, giving an undamped plasmon, or in the tail of the single particle excitation peak, in this case we have a Landau-damped plasmon. In the case of strong damping it is possible to follow the plasmon dispersion only following the plasmon peaks in ϵ^{-1}. Finally it is worth noticing that in any real situation plasmon resonances are always damped, even in the region where Landau damping is negligible, due to other interactions, like plasmon-phonon coupling or electron-electron interactions that go beyond the Random Phase Approximation.

5.3 Loss function of freestanding pristine and doped Graphene

Our first system under study is freestanding Graphene. We apply all the theory developed in the previous section to this system. Our aim is the calculation of the loss function of Graphene, that makes possible the interpretation of electron energy loss spectra. We will focus also in the influence of the charge carrier density due to doping in the loss function of Graphene.

5.3.1 Calculation details

Our *ab initio* calculation starts with a Density Functional Theory (DFT) ground state calculation for Graphene within the local density approximation (LDA) [30] for the exchange and correlation part of the potential. We use the plane waves basis set (cut-off energy 25 Hartree) and a norm conserving pseudo-potential of Troullier and Martins type [54]. Our system is constituted by repeated Graphene slabs with a slab spacing of ~ 20Å. The Brillouin Zone integration is carried out using a unshifted $60 \times 60 \times 1$ Monkhorst-Pack grid [36], resulting in 341 k-points in the irreducible Brillouin Zone and 3600 k-points in the Full Brillouin Zone, see section 1.1 for all the crystallographic information. In figure

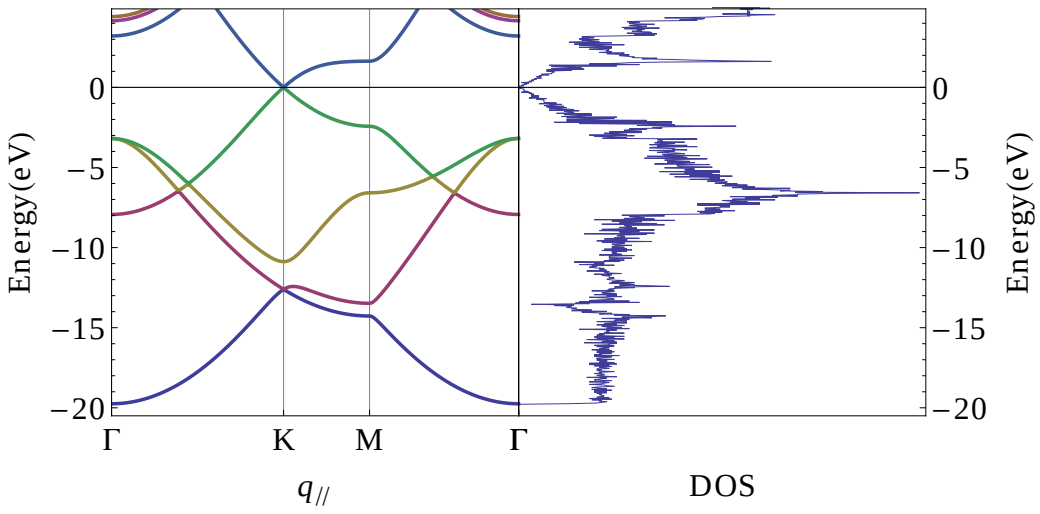

Figure 5.2: LeftPanel: Graphene band structure along the path **ΓKMΓ** obtained after the ground state calculation; the origin of the energy axis is the Fermi energy. RightPanel: Graphene Density of States.

5.2 we show the band structure and density of states (DOS) for Graphene, obtained after our ground state calculation. We obtain results in very good agreement with existing calculation found in literature, see for example ref. [77]; in particular we obtain the very well known dispersion at the Dirac point **K**, where valence and conduction band touch in a single point and the band dispersion is linear, having the shape of a cone [13]. The Fermi level, set to 0 in the figure, passes through this single point. The DOS is 0 at the Fermi level; we see also that nearly flat bands around the **M** point give rise to Van Howe singularities in the DOS, both in the occupied and in the unoccupied part.

We use the converged electron density to calculate one electron eigenerergies and eigenfunction on a denser k-point mesh ($180 \times 180 \times 1$, that is 32400 k-points in the Full BZ) and including up to 60 bands. The eigenenergies and eigenfunctions are plugged inside the Adler-Wiser formula, (5.20), to obtain the independent electron response function χ_0, from which we can calculate the density response function χ (5.29), the inverse dielectric function ϵ^{-1} (5.30), the RPA dielectric function ϵ_{RPA} (5.16), and all the desired quantities, as outlined in the previous section.

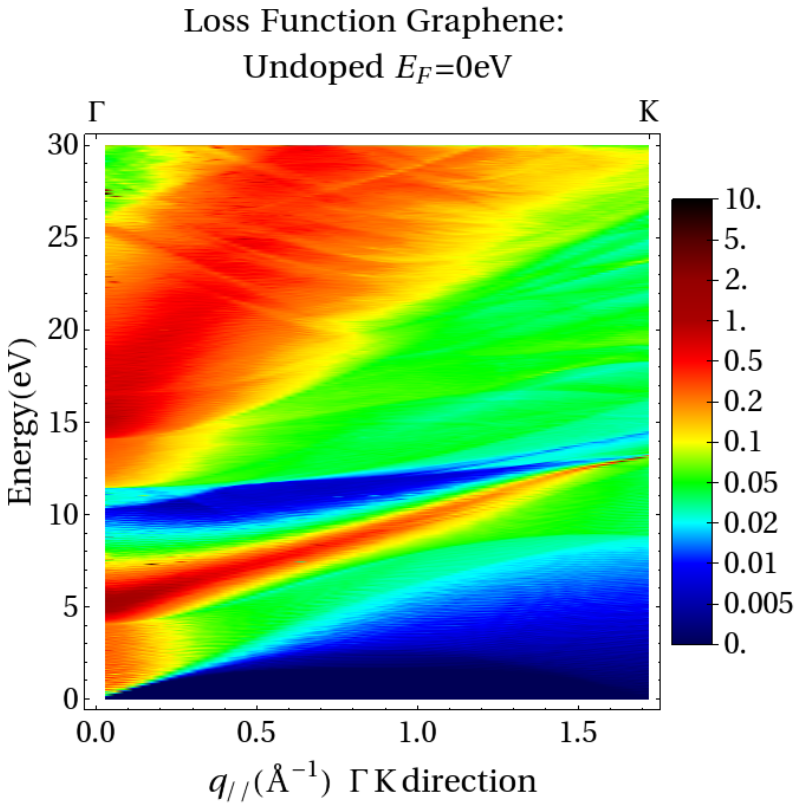

Figure 5.3: Energy loss function for undoped Graphene, as a function of the exchanged parallel momentum in Å^{-1} along the **ΓK** direction (horizontal axis) and energy in eV (vertical axis). The intensity scale (on the right of the plot) has logarithmic increments.

5.3.2 Undoped Graphene

In figure 5.3, we show the calculated Loss function for undoped Graphene, plotted as a function of the parallel exchanged momentum along **ΓK**, going from 0 to the **K**-point, and energy, from 0 to 30 eV. A cut at 0.287 Å^{-1} of the same calculation is given in figure 5.4, where we plot also the real part of ϵ_{RPA} and minus the imaginary part of ϵ_{RPA}, i. e., the SPE spectrum. In the Loss function we can recognize different features.

First of all we see the SPE at low energy as a nearly flat plateau, starting at $q_{\|} = 0$ and $E = 0$. This is clear from figure 5.4, where we see that the SPE plateau appears in the region where $-\mathfrak{Im}\{\epsilon_{RPA}\} \neq 0$.

After the SPE plateau we see an intense feature that disperses roughly linearly with the parallel momentum. As we can see in figure 5.4 these peak appears in the tail of the peak in the $-\mathfrak{Im}\{\epsilon_{RPA}\}$ and is correlated with a zero of $\mathfrak{Re}\{\epsilon_{RPA}\}$. In fact this peak is

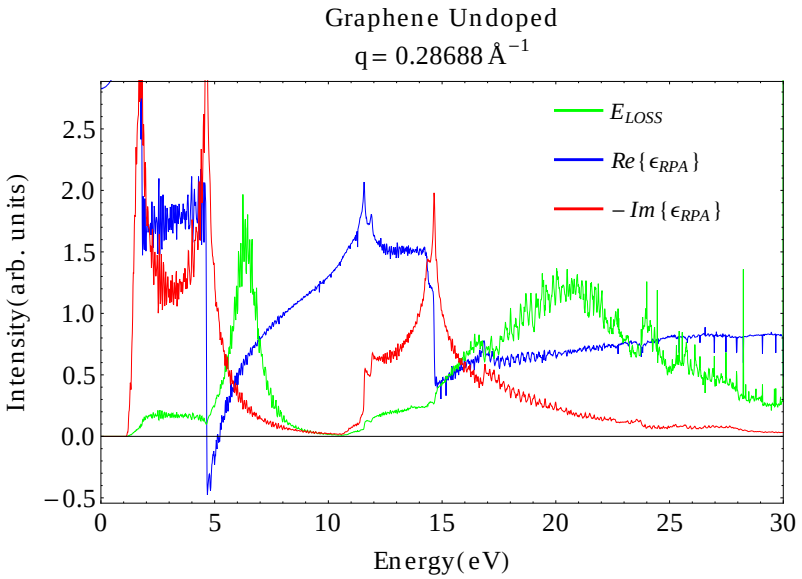

Figure 5.4: Energy loss function (green), real part (blue) and minus imaginary part (red) of ϵ_{RPA} for undoped Graphene, at the transmitted parallel momentum in 0.287 Å^{-1} along the **ΓK** direction as a function of energy in eV. The intensity is given in arbitrary unit because the plots have been scaled to allow them appear in the same graphic.

a plasmon peak, usually called π-plasmon that is also present in Graphite [110] and that in Graphene appears red-shifted with respect to graphite. The reason of the name is that this plasmon is the collective mode excited after the strong transition (the aforementioned peak in $-\mathfrak{Im}\{\epsilon_{RPA}\}$) between electrons from the Graphene π-bands, that are the last occupied and the first unoccupied bands (see figure 5.2) and that give rise to the Van-Howe singularities at roughly -2.5 eV and 2 eV in the DOS, see also ref. [111]. The fact that the π-plasmon is in a region where the SPE spectrum is decreasing but non-zero, makes it to be slightly broadened by Landau damping and gives it an asymmetric shape.

The third interesting feature in figure 5.3 is a very broad asymmetric peak that starts at roughly $15-18$ eV for $q_{\parallel}\sim 0$ and that disperse with $q_{\parallel}$. As it can be seen in figure 5.4 this peak is linked with a maximum of $-\mathfrak{Im}\{\epsilon_{RPA}\}$ (this time the transition being between a σ-level and a π-level) and with a drop of $\mathfrak{Re}\{\epsilon_{RPA}\}$ that does not become zero because of Landau damping. Actually, this peak is the so-called $\sigma-\pi$-plasmon that is also present in graphite and that in Graphene appears red-shifted with respect to graphite [110].

An important issue in the loss function calculations are crystal local fields effects. As already observed, once we use the Fourier representation for the χ_0, χ, and ϵ, for a given $\mathbf{q}$ and ω, we can imagine them to be matrices, whose matrix elements can be labeled by

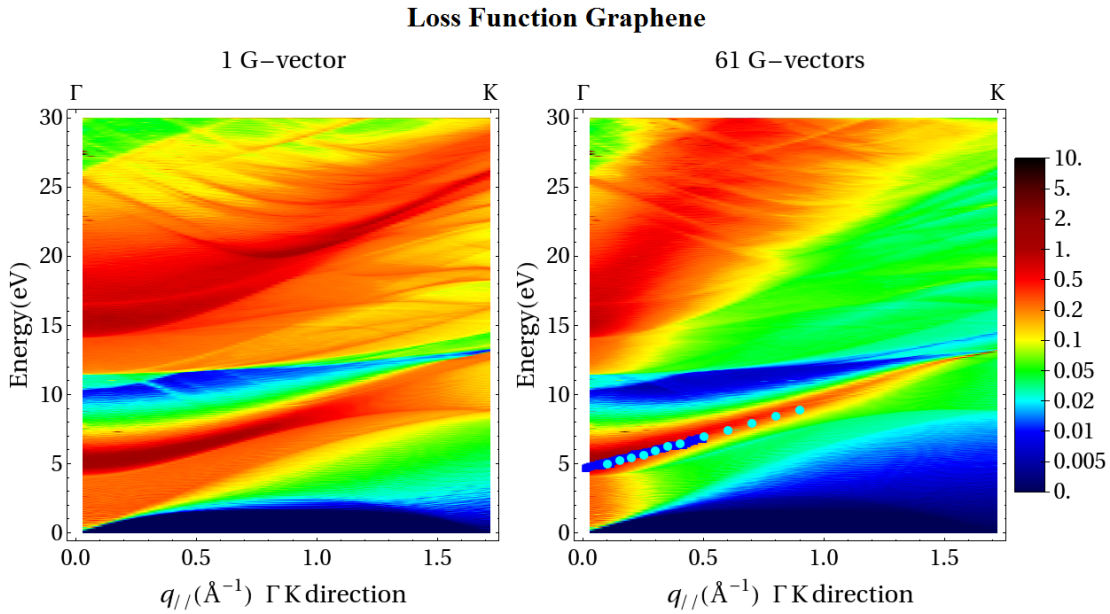

Figure 5.5: Energy loss function calculation for undoped Graphene as a function of the exchanged parallel momentum and energy, see figure 5.3.
Left Panel: the calculation includes only the $\mathbf{G} = 0$, $\mathbf{G}' = 0$ component in the χ_0 expansion (5.23), i.e., the calculation is without the inclusion of crystal local field effects.
Right Panel: the calculation includes 61 shortest $\mathbf{G}$-vectors, that is χ_0 is a 61×61 matrix; the calculation is compared to some available experimental data of the π plasmon dispersion for vertically aligned carbon nanotubes [112] (cyan circles), and for Graphene [113] (blue squares).

the reciprocal lattice vectors $\mathbf{G}$ and $\mathbf{G}'$, and that in fact are infinite dimensional. We can observe that in the definition of the loss function, equations (5.35) (5.32), we need only the $\mathbf{G} = 0$ and $\mathbf{G}' = 0$ component of ϵ^{-1}, nevertheless, we see that in the definition of χ, equation (5.29), and then also in ϵ^{-1}, all the infinite χ_0 matrix elements are used through the matrix multiplication. Actually only a finite number of matrix elements is needed for the calculation, because they are multiplied by the components of the Coulomb potential that decrease with increasing the length of the $\mathbf{G}$-vector. The convergency of the loss function with the number of $\mathbf{G}$-vectors included in the evaluation of the loss function is a crucial point, because the computation of the matrix elements of χ_0 is the most time consuming part of the calculation and the effects on the results are remarkable. This inclusion is usually referred to as including crystal local field effects, because the $\mathbf{G} \neq 0$ components have the meaning of microscopic periodic part of the function, as already pointed out.

We checked the convergency of the calculation including up to ~ 500 **G**-vectors in the definition of χ_0. We found that the inclusion of 61 **G**-vectors was enough to warrantee the convergency. Nevertheless the effect of crystal local fields is crucial. We can see this effect in the dispersion of the π-plasmon. It has been already proved that the inclusion of crystal local fields is necessary to reproduce the linear dispersion of the π-plasmon [112]. This issue is addressed in figure 5.5, where we can see that the inclusion of only 1 **G**-vector in the calculation results in a parabolic dispersion in the π-plasmon. Conversely the inclusion of 61 **G**-vectors gives a linear dispersing plasmon that is in very good agreement with the measured dispersion of the π-plasmon in Vertically aligned Carbon Nanotubes [112] and in Graphene [113], we note also the very good agreement between our calculation and other previous calculations on undoped Graphene [112, 114].

5.3.3 Doped Graphene

Once we have analyzed the undoped Graphene loss function, we can use the same technique to study the doped case. To do so we need to know how to include doping in our calculation. Actually we are interested in the case of doped freestanding or qausi-freestanding Graphene. The real (experimental) situation we want to analyze is in fact a Graphene monolayer that is suspended (freestanding Graphene) or is deposited on a substrate that has negligible influence on its electronic structure. Then we introduce the doping shifting the Fermi level above or below the Dirac point, that is we assume that the doping has the only effect of adding or removing electrons.

The aim of our calculation is to observe the effect that the charge carrier density[8] has on the screening properties of Graphene. The charge carrier density can be modified by different effects: defects in the Graphene lattice; the shape of the Graphene flake; chemical functionalization; interaction with the supporting substrate [89]; desired or undesired doping during the fabrication process [90]; a gating potential [12]. To do so we use the same ground state calculation for Graphene and artificially change the occupation factors f_i in (5.20) so that the Fermi level is shifted of the desired quantity ΔE_F, see figure 5.6. This represents an approximation, in fact we are assuming that adding or removing electrons does not change the energy bands of the system.

In figure 5.6 we show a zoom in energy of the band structure and the density of states of figure 5.2 near the Dirac point. The original Fermi level is set to zero energy. The

[8] In the case of Graphene we use surface densities.

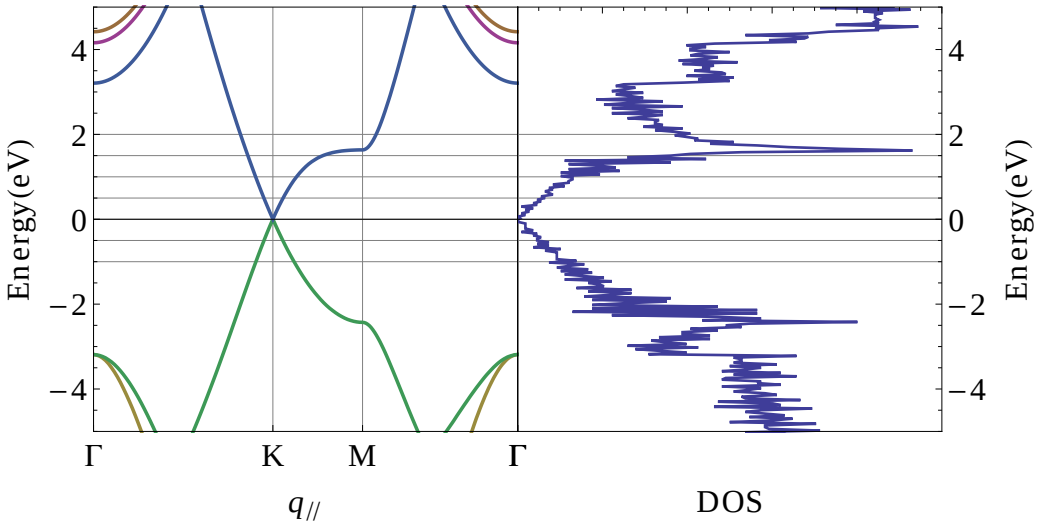

ΔE_F(eV)	$\overline{n}$	$p/n(\mp\ \mathrm{cm}^{-2})$
−1.0	−0.05420	-1.03455×10^{14}
−0.5	−0.011420	-2.71009×10^{13}
0	–	–
0.5	0.012346	2.3566×10^{13}
1.0	0.060124	1.14767×10^{14}
1.5	0.159383	3.04237×10^{14}
2.0	0.429938	8.20687×10^{14}

Figure 5.6: Energy bands and density of states for Graphene around the Dirac Point. The horizontal lines mark the position of the Fermi level used in this work for the doped Graphene calculation. In the table we list the values in eV of the Fermi level shift ΔE_F, the corresponding number of added (+) removed (−) electrons per unit cell $\overline{n}$ and the n (+) or p (−) doping concentrations.

horizontal lines mark the position of the Fermi level used to analyze the doped cases. The Fermi level shift ΔE_F, the number $\overline{n}$ of added/removed electrons per unit cell and charge carrier densities are listed in the table. We use the convention that a negative position of the Fermi level corresponds to a decrease of the electron per unit cell, the undoped value being 8. In this way negative numbers in the second and third column of the table correspond to situations where electrons are removed and holes are injected, so p-doping. Conversely positive numbers correspond to n-doping. Regarding the values of the charge carrier densities, we use the convention of calculating it using the number of charge carriers

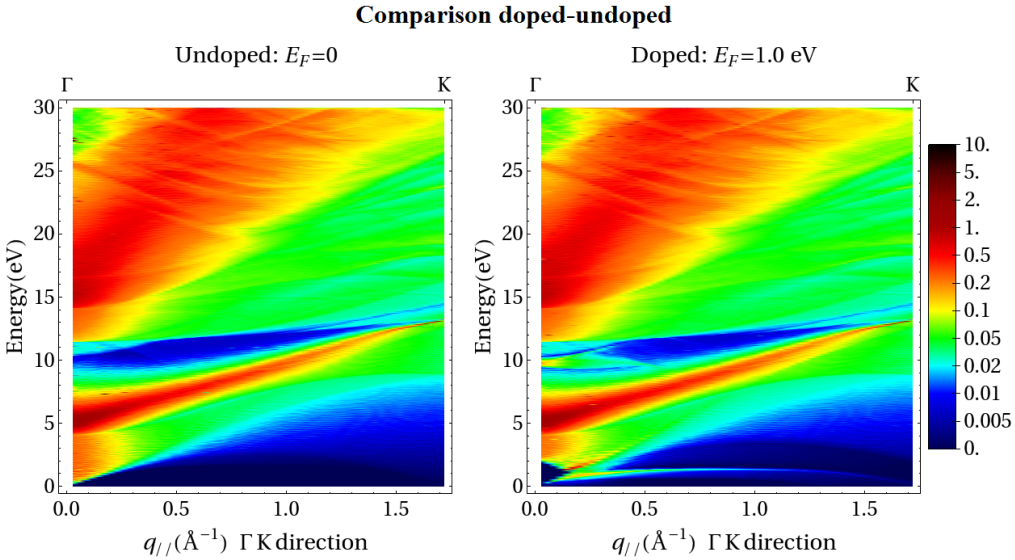

Figure 5.7: Energy loss function for undoped Graphene (left panel) and for doped Graphene $\Delta E_F = 1.0$ eV (right panel), as a function of exchanged parallel momentum and energy (see figure 5.3); the intensity scale (on the right) is the same in the two plots.

added (removed) with respect to the undoped case. It is worth noticing that values for the charge carrier densities used in this work are a little high. Typical values of charge carrier densities that can be obtained with gating potential are of the order $10^{12} \div 10^{13}$ cm^{-2} [12]; our analysis is more suitable for chemical doping [90]. Nevertheless, as we will see, we used such high values to better single out the effect of doping in the screening properties of the system.

We start our analysis with the comparison of the loss function of undoped Graphene and the loss function of Graphene doped using $\Delta E_F = 1$ eV, as shown in figure 5.7.

The first observation that we can make with the aid of figure 5.7 is that the doping does not influence neither the π plasmon, nor the $\sigma - \pi$ plasmon. We verified that this trend is verified for all the doping levels used in our analysis and shown in figure 5.6, but the case $\Delta E_F = 2$ eV. This result is not surprising because the π and $\sigma - \pi$ plasmons result from transition that involve the Van Howe singularities at ~ -7 eV, ~ -2.5 eV, and ~ 2 eV so they are not influenced as long as the Fermi level lies at values lower than ~ 2 eV. Then we can observe that the big difference between the doped and undoped situation is in the low energy part of the loss function. To better analyze this part we show in figure 5.8 a zoom of the loss function for low transferred energy and parallel momentum.

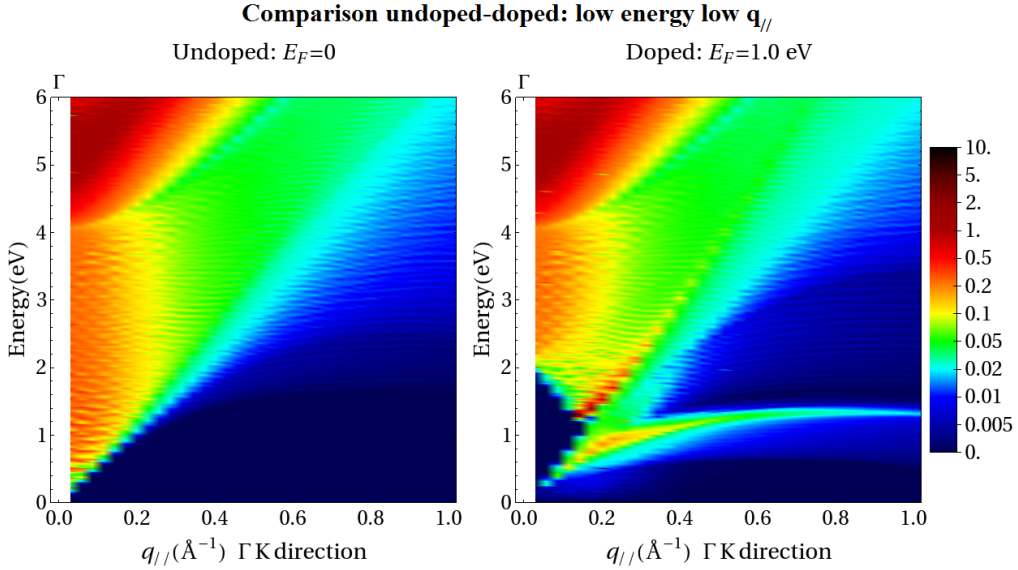

Figure 5.8: Energy loss function for undoped Graphene (left panel) and for doped Graphene with $E_F = 1.0$ eV (right panel), for low exchanged parallel momentum and energy; the intensity scale is the same in the two plot.

The zoom allows us to observe that the single particle transition part is strongly modified. We see that adding the doping causes a gap opening in the interband transitions (interband SPE). Then we can also observe some intensity below the "imaginary line" that represents the Fermi velocity, that was zero in the undoped case. This means that we are allowing some intraband transitions (intraband SPE). Both these result can be understood in the simple Dirac cone approximation, sketched in figure 5.9.

In the simple approximation of the cone band dispersion for Graphene, i. e., $E = v_F q_\parallel$, with v_F the fermi velocity, we see that, in the undoped case (see figure 5.9, left panel) only interband excitation are possible, because the valence band is completely filled and the conduction band is completely empty. We note also that the interband transition lie above the "Fermi velocity line" ($v_F|\mathbf{q}|$) and that it is possible to have transition at very low $q_\parallel$ and very low energy. In the doped case (figure 5.9, right panel) we are filling part of the conduction band (n-doping) or emptying part of the valence band (p-doping). This results in the opening of a gap for interband transition at low $q_\parallel$, that is the vertical (or quasi-vertical) transition at very low energy are forbidden. Furthermore, the half filling of the conduction or valence band, allow the appearing of intraband transitions, that lie below the Fermi velocity line.

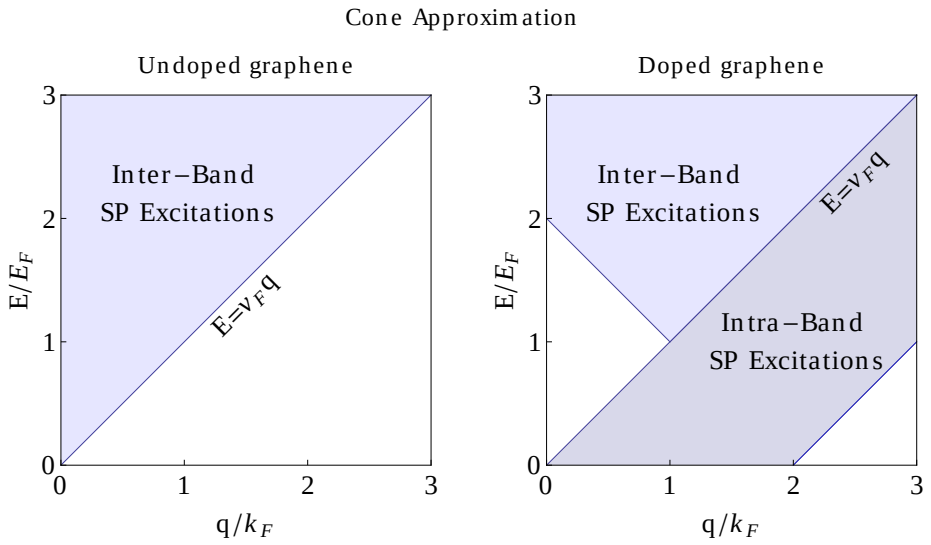

Figure 5.9: Schematic representation for Single Particle (SP) excitation in Graphene in the cone approximation; *Left Panel*: undoped case; *Right Panel*: doped case.

Coming back to figure 5.8 we see that, apart from the single particle excitation modification, we can observe two new features in the loss function, one sitting in the intraband SPE region and the other that is visible in the interband SPE region and seems to disappear entering the SPE gap region. Both the structures are connected to zeroes of the real part of ϵ_{RPA}, so we can conclude that they are collective modes, even though Landau-damped plasmons. The structure that lies lower in energy (we will call it low energy palsmon from now on) is always Landau damped by intraband SPE. The structure that lies higher in energy (high energy plasmon from now on) is Landau damped in the interband SPE region. Because we didn't include any artificial damping mechanism in our calculation, the high energy plasmon is undamped in the SPE gap region, where it appears as a Dirac delta that can't be caught by our finite energy mesh. We can follow its dispersion inside the undamped region through the zeroes of ϵ_{RPA}. In this way, following the zeroes of ϵ_{RPA} in the gap region, and the maxima of the loss function in the damped region, we are able to draw a dispersion for both the plasmons, shown in figure 5.10.

Before going on with the analysis, it is interesting to compare the low energy part of the loss function when the exchanged parallel momentum is on different directions. In figure 5.11 we show the calculated loss function for doped Graphene ($\Delta E_F = 1.0$ eV), with the exchanged parallel momentum lying on the **ΓK** and **ΓM** directions.

We see that the single particle excitation is slightly different, and this reflects directly

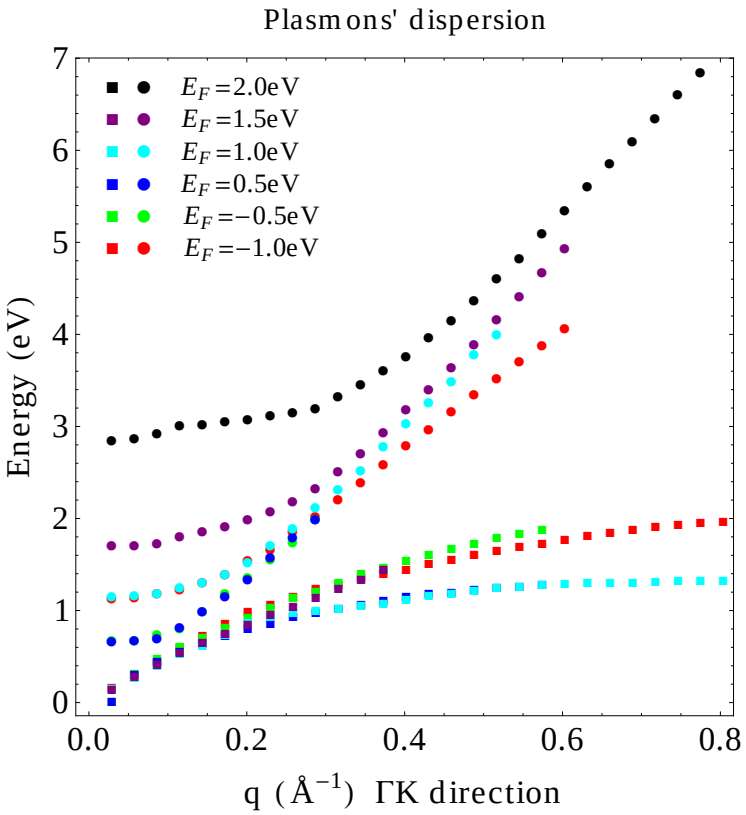

Figure 5.10: Energy momentum dispersion for the two new plasmons in doped Graphene for different doping levels. Squares represent the low energy plasmon, circles the high energy one; the colour code is shown in the inset.

the different band dispersion along the two directions. More interestingly, we can clearly see that the low energy plasmon is absent along **ΓM** and that the high energy plasmon dispersions are different, their linear dispersion having different slopes.

To understand the nature of the two new plasmons is necessary to analyze their properties, starting from figure 5.10.

We can start from the low energy plasmon. It lies always in the region of single particle intraband excitations, so it is always Landau damped. From figure 5.10 we can see that it disappears for $\Delta E_F = 2$ eV; we should also add that the shape of the peak is altered for a doping of 1.5 eV (not shown explicitly). Moreover, we see that the plasmon disappears when we move to the **ΓM** direction. We see also that the dispersion is different in case of n- and p-doping.

As for the high energy one in figure 5.10, we can see that it exhibits an almost linear

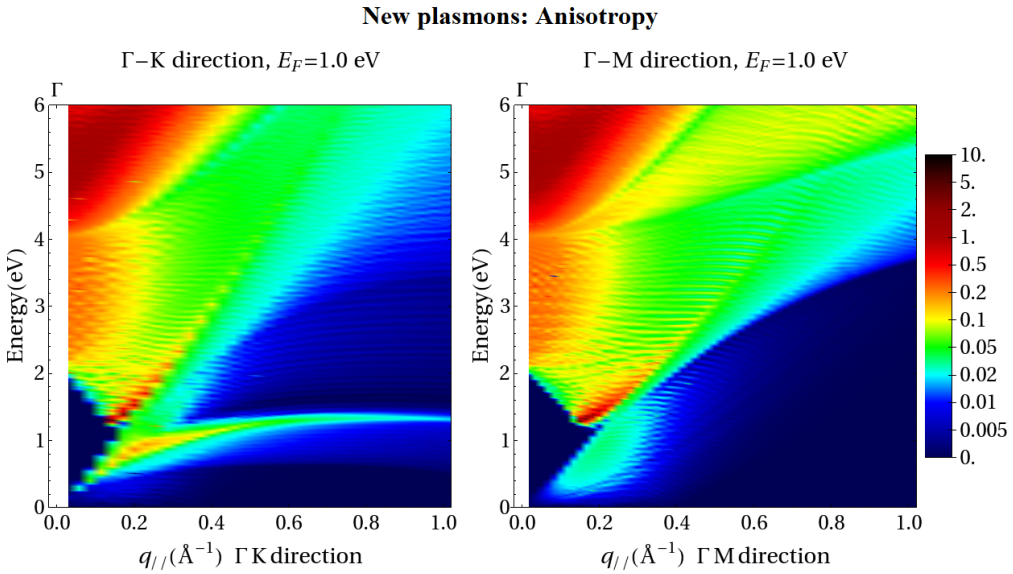

Figure 5.11: Comparison between the loss function for doped Graphene for momentum transfer along two different directions in the Brillouin zone, left panel **ΓK**, right panel **ΓM**.

dispersion at high energies with a slope that is independent on the doping level, but has two different values for n- and p-doping. Moreover the slope depends on the direction of the transferred momentum. For low momentum transfer it enters the SPE gap region and its dispersion becomes slightly flat, approaching a value that depends on the doping level.

All these properties can be explained looking at the band dispersion around the **K**-point of the Brillouin zone. In figure 5.12 we show a comparison between the Graphene band structure around the **K**-point obtained in the framework of the cone approximation (black dashed line) and the one obtained in our DFT calculation. We see that in the "real" situation, instead of an isotropic cone, we have different band dispersions on the different directions. With the aid of the Brillouin zone reproduction in figure 5.12 we can see that if we put the transferred momentum $q_{\parallel}$ along the **ΓK** direction we are actually probing two different lines in the Brillouin zone: the first one is the $\mathbf{K} \rightarrow \mathbf{\Gamma}$ line, highlighted by the red arrow, and that results in the red branch; the second one is the $\mathbf{K} \rightarrow \mathbf{M}$ line, highlighted by the blue arrow, and that results in the blue branch. Conversely, if we put $q_{\parallel}$ along the **ΓM** direction we are probing only one direction, $\mathbf{K} \rightarrow \mathbf{K}$, highlighted by the green arrow, that results in the green branch.

The above observations allow us to conclude that the two new structures are intraband plasmons. We observe the low energy plasmon only when $q_{\parallel}$ is along **ΓK** because we see

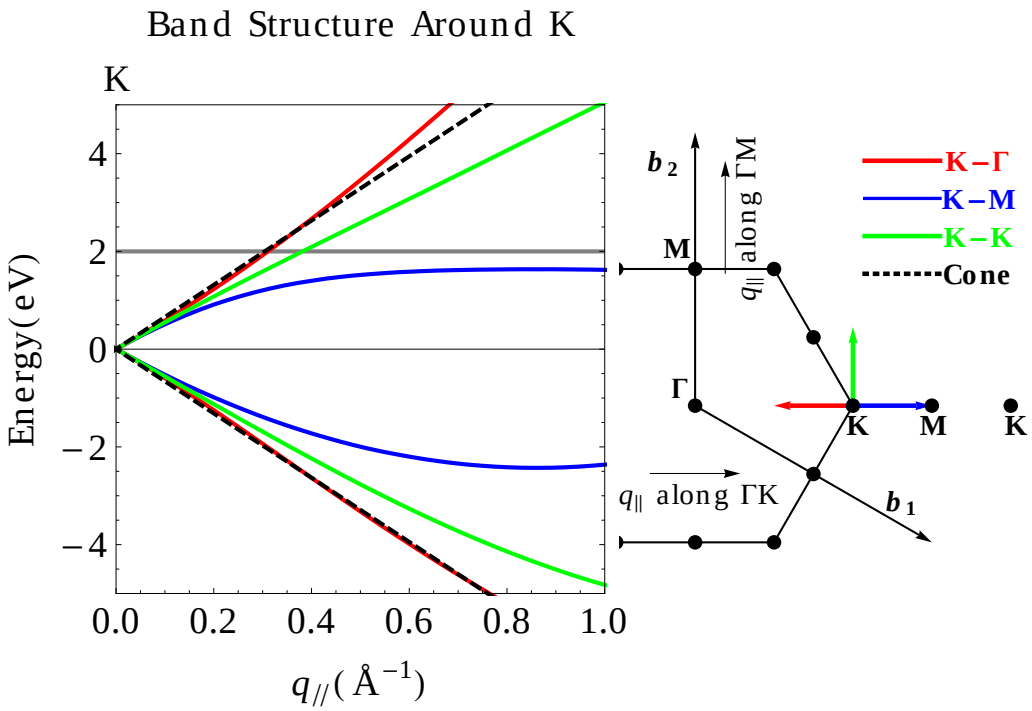

Figure 5.12: Anisotropic band structure of Graphene, as obtained from our ground state DFT calculation and plotted along three different high symmetry paths originating at the **K**-point and highlighted by arrows in the Brillouin zone reproduction, i.e., **KΓ** (red arrow and line), **KM** (blue arrow and line), **KK** (green arrow and line); **KΓ** and **KM** branches are sampled by $q_{||}$ along **ΓK**, while $q_{||}$ along **ΓK** samples the **KK** branch. The isotropic behaviour due to the cone approximation for the π bands, at the Dirac point, is shown as a black dashed line.

that the band structure has two different branch, so we have electrons with two different velocities within the same band, resulting in two distinct intraband plasmon modes. This is also consistent with the observation that the low energy plasmon changes its shape increasing the doping up to $\Delta E_F = 1.5$ eV and disappears for $\Delta E_F = 2.0$ eV, because for these doping levels the band branch that give rise to the plasmon is almost filled or completely filled and the intraband transitions are accordingly unfavored or forbidden. This attribution explains also the different dispersion for n- and p-doping, in fact it is clear that the blue band in figure 5.12 is not symmetric going from positive to negative energies. When $q_{||}$ is along the **ΓM** direction we have only one branch, then only one intraband plasmon mode.

Now we can focus on the high energy plasmon that is present in both directions but has different slopes in the high momentum limit. The existence of this intraband plasmon has

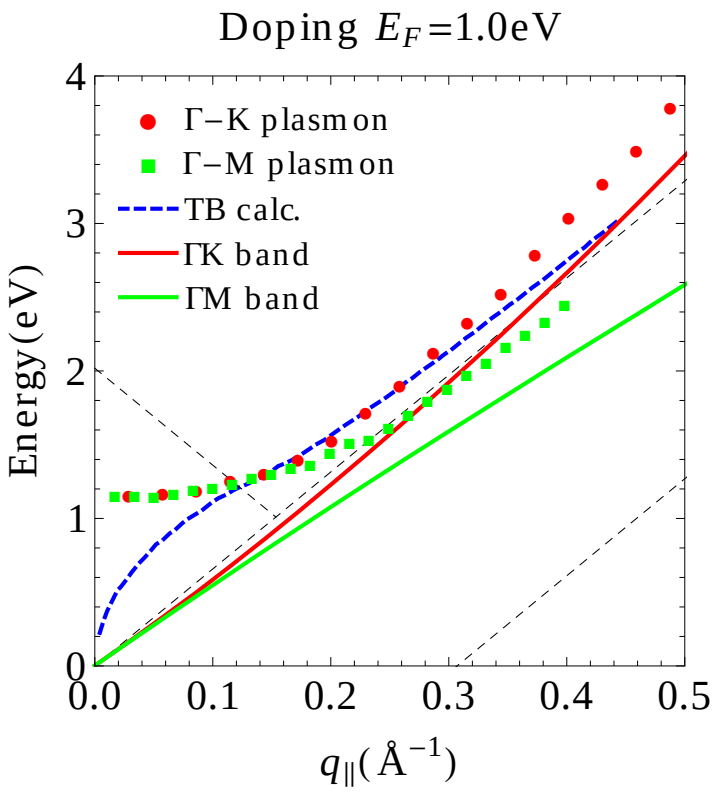

Figure 5.13: High energy plasmon dispersion relation for $q_{\|}$ along **ΓK** (red circles) and along **ΓM** (green squares); our calculation is compared to the Tight Binding based calculation by Hwang and Das Sarma [98] relying on the cone approximation (blued dashed line). In the figure are also shown the band dispersions along **ΓK** (red line) and **ΓM** (green line) taken from figure 5.12.

been predicted by some tight binding (TB) calculations relying on the cone approximation, assuming linear dispersing bands around the Dirac point and infinite bandwidth [97, 98, 99]. The plasmon has also been observed experimentally by many authors on Graphene adsorbed on different materials [92, 93, 94, 95, 96]. The calculations predicted a square root dispersion law for low $q_{\|}$ and a linear dispersion, parallel to the Fermi velocity line, for high $q_{\|}$. The square root law for low $q_{\|}$ is typical of 2D plasmons [115], while the linear dispersing behavior at high $q_{\|}$ is typical of Graphene and is due to the linear dispersing bands. In figure 5.13 we compare the TB based calculations by Hwang and Das Sarma [98] with our ab-initio calculation.

As it is clear from figure 5.13 we find a substantial agreement, in an intermediate momentum transfer region between ~ 0.2 and ~ 0.4 Å^{-1}, and two major differences, at low momentum and high momentum transfer. Specifically, in our calculation the plasmon

dispersion becomes flat for low $q_{\parallel}$, while the "classical" 2D plasmon should go to zero energy as $\sqrt{q_{\parallel}}$ for $q_{\parallel} \to 0$ [115]. Such a discrepancy is an artifact of the three dimensional slab periodicity required in ground state DFT computations with plane waves; in fact, for low $q_{\parallel}$ the Coulomb interaction entering χ is dominated by the long range part. In practice, when $q_{\parallel}$ approaches 0 the charge densities associated with the plasmons on the Graphene replicas start seeing each other, rendering the collective mode a fictitious 3D plasmon, with the typical 3D plasmon behaviour, i.e., a finite non zero energy limit for $q_{\parallel} \to 0$ and zero slope [87]. Conversely, for high values of $q_{\parallel}$ the TB-calculated plasmon becomes linear, with the slope being the Fermi velocity in the cone approximation, i. e. the plasmon dispersion is parallel to the band dispersion. In our calculation, the high energy plasmon dispersion is linear and parallel to the band dispersion as well; however in the real case the band dispersion is anisotropic, thus, the different slopes of the plasmon dispersion reflect the different Fermi velocities in the inequivalent directions.

5.3.4 Summary on doped Graphene

Summarizing, our calculation of the loss function for Graphene with different charge carrier densities showed that some new resonances are present in the low energy part of the loss function. These resonances are intraband plasmons and proved to be sensitive to the charge carrier density. This can suggest to use electron energy loss spectroscopy as a tool to determine the doping level of freestanding and quasi-freestanding Graphene. Our calculation showed also that the two new features have a remarkable anisotropy. This anisotropy comes from the anisotropy of the band structure around the Dirac point and results, in practice, in electrons having different velocities within the same band that give rise to acoustic plasmon with different dispersions. This anisotropic effect on the acoustic plasmon dispersion has not yet been observed experimentally.

5.4 Loss function of Graphene adsorbed on Ni(111) surfaces

Once we have investigated the loss function of freestanding and quasi-freestanding Graphene, we move to the system Graphene adsorbed on Ni(111). In this case we can not consider Graphene as quasi-freestanding because of the strong interaction between the electrons belonging to the Graphene π bands and the d-electrons of Nickel. Nevertheless the system

is particularly interesting because Ni(111) surfaces are very well suited for the absorption of Carbon graphitic monolayer [15] so this system has been investigated for long time, both theoretically and experimentally, and now it is receiving renewed interest for the synthesis and study of Graphene.

5.4.1 Calculation details

As in the previous case, our calculation start with a DFT ground state calculation using the LDA approximation [30] for the exchange and correlation and the plane waves basis set (cut-off energy 25 Hartree). This time we use the ABINIT code [75, 76] for the ground state calculation. We use norm conserving pseudopotentials of Troullier-Martins type [54] for both Carbon and Nickel. The Graphene-Nickel interface is modeled with a slab (made up by 1-, 2- or 3-monolayer of Nickel oriented in the (111)-direction) and Carbon atoms. The unit cell is made such that one of the two inequivalent carbon atoms sits on top of the topmost layer Nickel atoms and the other one is in the fcc hollow sites; the geometry is taken from the calculation by Bertoni et al. [17], see section 1.1. As in the previous case, we make a periodic calculation in three dimensions. The 2-dimensional slabs are repeated in the perpendicular direction with a periodicity of ~ 21 Å. The Brillouin zone integration is carried out using an unshifted $60 \times 60 \times 1$ k-point Monkhorst-Pack grid [36]. The converged electron density is used to calculate eigenvalues and eigenfunctions on the same grid, including 60 bands; this allows us to calculate a converged loss function up to 15 eV above the Fermi level.

5.4.2 Graphene Nickel loss function

In figure 5.14 we show the band structure for Graphene adsorbed on 1, 2 and 3 atoms thick Nickel slabs, and the corresponding density of states. The comparison with figure 5.2 shows that the deep Graphene σ bands are not influenced by the Nickel d bands; conversely the Graphene band structure is strongly modified in the region in energy near the Fermi level where the nearly flat Nickel bands appear. The mayor difference is that the Dirac cone is not present anymore and the density of states is very high at the Fermi level.

We can expect that this increased number of electrons near the Fermi level plays a prominent role in the screening, and then in the loss function. In figure 5.15 we show the Graphene/Nickel loss function for the three different analyzed configurations as a function

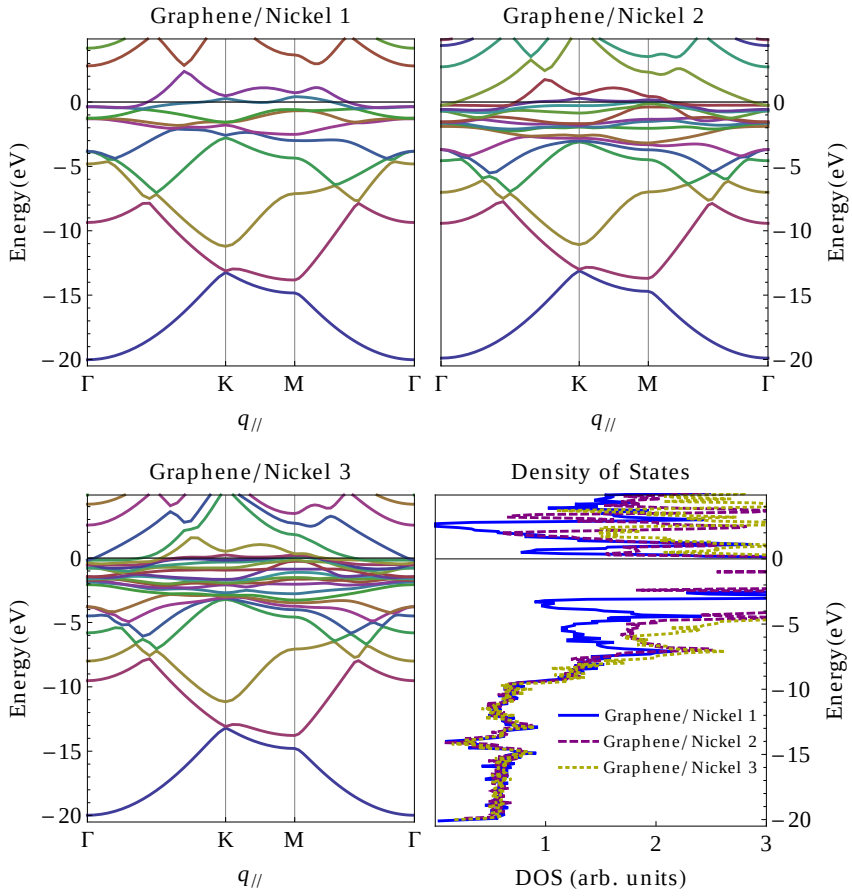

Figure 5.14: Graphene adsorbed on Ni(111): band structure for Graphene on 1 Ni layer (top left), 2 Ni layers (top right) and 3 Ni layers (bottom left); density of states for the three calculations (bottom right).

of exchanged parallel momentum along the **ΓK** direction and energy. In all the three situations at low $q_{\|}$ the loss function is dominated by a peak at about $6 \div 8$ eV that can be attributed to the Graphene π plasmon. This peak is superimposed on a background due to the Nickel substrate, as we see that it changes increasing the number of Nickel layers. At higher $q_{\|}$ the overall intensity drops down and also the relative intensity of the π peak with respect to the background, in all the analyzed configurations. We also observe that the Nickel substrate causes a broadening of the π peak, as compared to the Graphene (see figure 5.4); the width of the peak also increases increasing the number of Nickel layer, and in all cases is much bigger than the one calculated for freestanding Graphene. To better understand, in figure 5.15, bottom right panel, we show the energy momentum dispersion of the π plasmon, calculated as the maximum of the observed peak. We observe also that,

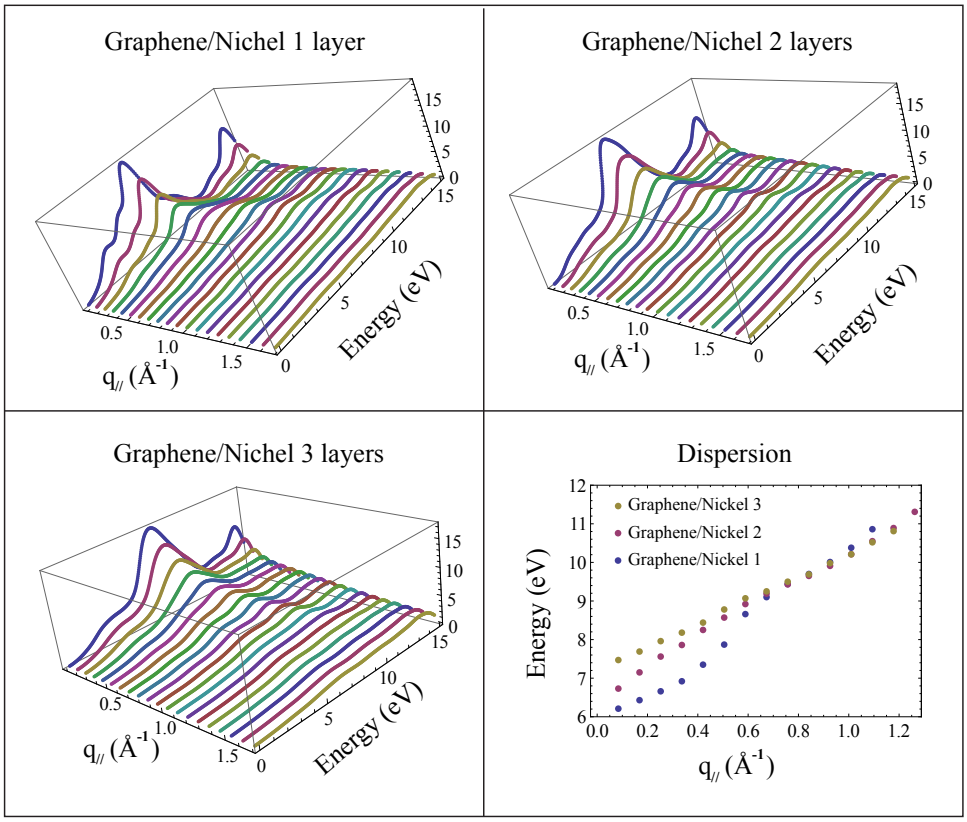

Figure 5.15: Energy loss function for Graphene adsorbed on Nickel 1 layer (top left), 2 layers (top right), 3 layers (bottom left) as a function of the exchanged parallel momentum on the ΓK direction and energy. The intensity scale is the same within the same plot. Bottom right: energy momentum dispersion of the π plasmon peak.

at least for the few lowest analyzed $q_{\parallel}$ we see the initial part of a maximum at higher energies; this maximum can be attributed to Graphene $\sigma - \pi$ plasmon, even though the energy range of the calculation should be increased to assign it confidently.

The Graphene π plasmon is indeed the more interesting part. We see that the three different calculations give results consistent with one another, even though, as we already observed, the width of the peak may suggest that the peak shape is influenced by some structure due to the Nickel substrate. This observation is further confirmed by the different dispersion obtained in the three calculations. We observe that the three calculation seem to have two branches following two different dispersion laws, the separation between the two regimes being $q_{\parallel} \sim 0.6$ Å^{-1}. The high $q_{\parallel}$ part is the same for the three calculations,

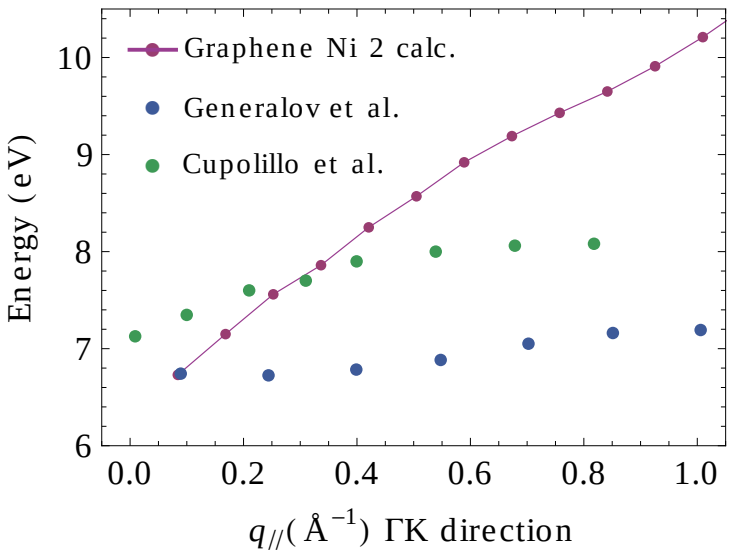

Figure 5.16: Comparison between π plasmon dispersions calculated in the present work for the system Graphene/Nickel 2 layers and the experimental measurement by Cupolillo et al [101] and Generalov et al. [100] on Graphene adsorbed on Nickel.

while the low $q_{\parallel}$ part is slightly different. We can ascribe this behavior to the presence of two structures, one being the Graphene π plasmon and the other one being some SPE peak due to the Nickel substrate, appearing at higher energies with respect to the π peak[9]. This structure causes an additional broadening through Landau damping on the π peak that become quite indistinguishable from the SPE background at high $q_{\parallel}$ and causes also a blue shifting of the π peak. This effect increases in strength with increasing the number of Nickel layers.

In two recent papers [101, 100] the energy loss of Graphene adsorbed on Nickel has been reported together with a dispersing structure identified with the Graphene π plasmon. In figure 5.16 we show a comparison of the calculated dispersion for the system Graphene Nickel 2 layers and the experimental data by Cupolillo et al. [101] and by Generalov et al. [100]. As we can see, the agreement is not very good specially for high $q_{\parallel}$. However we can observe that the two set of data are in substantial disagreement with one another. The main issue is that the experimental EELS measurements taken into account, as it is clear from both articles, are affected by a large uncertainty due to background substraction and to the exact determination of the energy position of the plasmon resonance. On the

[9]In freestanding Graphene the loss function goes to zero after the π peak (see figure 5.4) here we have non zero intensity.

other hand we already mentioned that in our calculation the peak of the π resonance is very broad. Actually our calculation can be improved both from the technical point of view, including more k-points in the BZ integration, and from the principle point of view, understanding better the role played by the number of Nickel layers included in the calculation. Both of the improvement are presently under study.

5.5 Conclusions

Summarizing in this chapter we calculated the energy loss function for freestanding Graphene and Graphene adsorbed on a Ni(111) surface.

The loss function for freestanding Graphene show three main contributions. First, the single particle excitation spectrum starting at low energy and low $q_{\parallel}$. Second, the linear dispersing π plasmon starting at ~ 5 eV, that appear red-shifted with respect to the graphite π plasmon. Third, the broad $\sigma - \pi$ plasmon at higher energies, appearing red-shifted with respect to graphite as well. Then we calculated the modification of the energy loss function of freestanding Graphene due to the injection of electrons or holes. The main result is the appearance of two intraband acoustic plasmon resonances, instead of the single intraband resonance observed in the experiments and predicted through TB calculations. The two resonances are the result of the anisotropy around the Dirac point, usually neglected in TB based calculations, that have as a consequence the presence of electrons with two different velocities within the same band, resulting in two distinct plasmon dispersions. The low energy intraband plasmon still waits to be observed experimentally.

Then we calculated the loss function of the system Graphene-Nickel (111) as a paradigmatic example of strong bonding between the Graphene with the supporting material. The main effect of the Nickel substrate is the destruction of the Dirac conical point due to the hybridization of the carbon p orbital with the Nickel d orbitals. As a consequence we observe an high density of state at the Fermi level, unlike the zero density of state at the Fermi level of Graphene, that results in different screening properties. In particular we observe a significative distortion of the Graphene π plasmon peak and a different peak dispersion, due to the interaction of the π plasmon with the single particle excitation due to the Nickel substrate. This feature is compared with two experimental observation reporting the same effect, even though the accord is not very good. The discrepancy can be probably reduced through an improvement of the calculation technique, presently under study.

Chapter 6

Conclusions and perspectives

In this work we have analyzed some properties related to electron excitations in carbon based nanomaterials, which offer a wide range of potential technological applications and represent an important field for fundamental research. Our main focus has been on Graphene, doped Graphene, adsorbed Graphene on metal surfaces, and carbon nanotubes, with particular attention to ground-state electronic properties and electron excitations of the valence and conduction bands.

The first part of the thesis was concerned with a study of the kinetic energy distributions of electron emitted by Auger core-valence-valence processes (CVV) in carbon nanotubes (CNTs). Indeed, the principles at the basis of the Auger effect allows to investigate both inner core electrons and valence band properties of the target materials. We presented a density functional theory (DFT) method to calculate the Auger emission probability in the framework of the Fermi golden rule (FGR), and applied it to a $(10, 10)$ armchair single walled (SW) CNT. Our main goal was to asses, through the comparison of our results with experimental data taken from literature, the role of some many body corrections that lie outside the FGR approach and are at the heart of the "exotic" electronic properties of carbon based materials. In particular, we treated two many body effects: the shake up of valence electron, due to the core hole dynamic screening in the initial state, and the effect of hole-hole interactions in the valence band, due to the missing final state electrons. We treated initial and final state effects by a mean field approach that corrects the ground state DFT calculations, and we found these corrections to be necessary for an accurate description of Auger electron emission spectroscopy experiments on nanotube bundles. As a side effect, we faced a technical problem, that is of fundamental interest in the DFT modeling of carbon based materials and in DFT in general. We tested an all-electron

cluster and a periodic pseudopotential DFT approaches as starting ingredients to evaluate the FGR. We found a general good agreement in the output electronic structures, apart from some significant differences concerning the lowest occupied valence states of the system. We addressed such discrepancies to the pseudization procedure that removes the 1s core orbitals of carbon in pseudopotential calculations. This point, however, needs a more detailed analysis that will be the subject of future works. Another interesting point that will deserve our attention is a more self-consistent evaluation of initial and final state effects, for example by time-dependent (TD) DFT techniques with suitable approximations capable of reducing the computational complexity inherent in these methods.

As a second argument, we presented a study of secondary electron emission (SEE) from Graphene adsorbed on a Nickel (111) surface. We first tackled the problem from the experimental point of view, by presenting electron emission spectra induced by primary electron bombardment. We found some interesting features on a series of peaks superimposed to the cascade electron peak. Consistent with the previous literature on SEE from other target materials, we attributed this series of peaks to maxima in the density of unoccupied states above the vacuum level, i. e. to the empty bands of the system. We then made a systematic study of the peak positions through angular resolved SEE, being able to draw a band dispersion plot. We completed our analysis with band structure calculations using DFT, adapted to compute a k-projected density of states (k-DOS). We applied this method to graphite first, taking advantage of a vast amount of data available in the literature, and found a satisfactory agreement between our k-DOS calculations, capable of highlighting both the bulk and surface properties, and the experiments. Then, we applied the same technique to our measurements, finding a good agreement that allowed us to assign the investigated bands both to the Graphene overlayer and to the Nickel substrate. Our analysis highlighted an interesting property of the Nickel bands that are somehow hidden in the cascade of the clean Nickel spectrum, but are enhanced by presence of Graphene. This point will be investigated more deeply, both from the experimental and theoretical sides.

Finally, we turned our focus to electron energy loss spectroscopy (EELS) of freestanding Graphene and Graphene adsorbed on Nickel surfaces. We shortly reviewed an ab initio method to calculate the loss function, using DFT calculations and linear response theory. We calculated the energy loss function for freestanding Graphene, focusing on the loss function modifications induced by doping, i. e. the injection of electrons or holes in the system. We found that the increased charge carrier density leads to the appearance of two

intraband plasmon resonances in the loss function, with a prominent anisotropic behavior. This result is different from other loss function calculations on Graphene, which mainly dealt with the π and σ-π plasmon modes. In addition, only one of the two resonances has been detected by experimental EELS measurements on quasi-freestanding Graphene. We thus suggest to perform angle resolved EELS measurements on freestanding Graphene, which is still lacking, and to find the missing plasmon mode and the anisotropic behavior, that should be observable with specific doping conditions according to our calculations. We also studied the dielectric properties of Graphene adsorbed on Nickel (111), with particular care to the π plasmon of the Graphene overlayer. Our main predictions concern the broadening and blue-shift of this mode with respect to the freestanding Graphene case due to the Nickel substrate. The role of substrate electrons is, however, not fully understood, being a paradigmatic example of strong Graphene/metal interactions.

Appendix A

Two-electron matrix element of Auger CVV emission

In order to apply the FGR in calculating the Auger spectrum, we first need to compute the Coulomb integrals $V_{s\,v'}^{q\,v}$, introduced in Eq. (3.9), section 3.3, that involve: a core orbital (ϕ_s), two valence orbitals (ϕ_v and $\phi_{v'}$), and a plane-wave (ϕ_q). Most DFT approaches, like those presented in section 3.4, use core and valence pseudo-orbitals represented in a finite basis of spherically symmetric localized functions $\psi_i(\mathbf{r},\mathbf{R}) = \langle \mathbf{r}|i_{\mathbf{R}}\rangle$, of symmetry index i and center $\mathbf{R}$. Accordingly, each $V_{s\,v'}^{q\,v}$ becomes a linear combination of the three-center partial integrals:

$$\mathcal{V}_{s\,i'}^{q\,i}(\mathbf{R},\mathbf{R}',\mathbf{S}) = \int d^3r \int d^3r'\, e^{-i\mathbf{q}\cdot\mathbf{r}}\, \psi_i(\mathbf{r},\mathbf{R})\, \frac{1}{|\mathbf{r}-\mathbf{r}'|}\, \psi_s^*(\mathbf{r}',\mathbf{S})\, \psi_{i'}(\mathbf{r}',\mathbf{R}') \tag{A.1}$$

where we have chosen a unit volume in the normalization constant of the plane-wave.

In chapter 3 the Auger spectrum from a cluster of carbon atoms placed on a $(10,10)$ SWCNT has been described with a basis sets of Gaussian type orbitals. With such a basis, the partial integrals $\mathcal{V}_{s\,i'}^{q\,i}$ have complicated analytical expressions that we will show in details in section A.1. With more general basis sets the same terms are numerically demanding 6-dimensional integrals. However, the strong localized nature of the core-orbitals allows us to retain only the on-site contributions in Eq. (A.1), with $\mathbf{R} = \mathbf{R}' = \mathbf{S}$. This is because the core-functions ψ_s are so sharply peaked at the core-sites $\mathbf{S}$, that the off-site $\mathcal{V}_{s\,i'}^{q\,i}$-integrals contribute negligibly to $V_{s\,v'}^{q\,v}$. In section A.2, we will see how the on-site approximation let us reduce Eq. (A.1) to 2-dimensional radial integrals that are fastly computed with both numerical and analytical basis sets. Such an approximation has been crucial in calculating

the Auger spectrum from a periodic $(10, 10)$ SWCNT with the numerical basis introduced in section 3.4.

A.1 Gaussian basis function

Carbon based materials have a ground state that includes only s and p one-electron pseudo-orbitals. Using a Gaussian basis set, we can evaluate the partial integrals (A.1) with the following s-type and p_i-type orbitals ($p_i = p_x, p_y, p_z$):

$$\psi_{\zeta\, s}(\mathbf{r}, \mathbf{R}) = \left(\frac{2}{\pi}\right)^{3/4} \zeta^{3/4}\, e^{-\zeta|\mathbf{r}-\mathbf{R}|^2}, \tag{A.2}$$

$$\psi_{\zeta\, p_i}(\mathbf{r}, \mathbf{R}) = 2\left(\frac{2}{\pi}\right)^{\frac{3}{4}} \zeta^{5/4}\,(x_i - X_i)\, e^{-\zeta|\mathbf{r}-\mathbf{R}|^2}, \tag{A.3}$$

parametrized by an exponent ζ and centered at position $\mathbf{R}$. We, therefore, take a core state $\psi_{\gamma s}$, located at the site $\mathbf{C}$, and begin by using two s-Gaussians for the valence basis functions $\psi_{\alpha s_a}$ and $\psi_{\beta s_b}$, centered at positions $\mathbf{A}$ and $\mathbf{B}$, respectively. In other terms, we work on the partial integral

$$\mathcal{V}_{\gamma s\,\beta s}^{q\,\alpha s}(\mathbf{A}, \mathbf{B}, \mathbf{C}) = \left(\frac{2}{\pi}\right)^{9/4} \frac{\gamma^{3/4}\alpha^{3/4}\beta^{3/4}}{V_{\mathrm{OL}}^{1/2}} \int d^3r\, e^{-i\mathbf{q}\cdot\mathbf{r}}\, e^{-\alpha|\mathbf{r}-\mathbf{A}|^2} \times \int d^3r'\, e^{-\gamma|\mathbf{r}'-\mathbf{C}|^2}\, e^{-\beta|\mathbf{r}'-\mathbf{B}|^2}\, \frac{1}{|\mathbf{r}-\mathbf{r}'|},$$

where we have restored the volume in the normalization constant of the plane wave. Then, we replace the Coulomb potential with the Yukawa potential, that is we make the substitution:

$$\frac{1}{|\mathbf{r}-\mathbf{r}'|} \to \frac{e^{-\mu|\mathbf{r}-\mathbf{r}'|}}{|\mathbf{r}-\mathbf{r}'|}, \tag{A.4}$$

with the idea of letting the screening constant μ go to zero at the end of the integration procedure. Such a substitution allows us to Fourier transform the potential to the momentum space, i. e., to use the representation:

$$\frac{e^{-\mu|\mathbf{r}-\mathbf{r}'|}}{|\mathbf{r}-\mathbf{r}'|} = \int \frac{d^3p}{2\pi^2} \frac{e^{i\mathbf{p}\cdot(\mathbf{r}-\mathbf{r}')}}{p^2+\mu^2}, \tag{A.5}$$

which leads to the Yukawa potential matrix elements

$$\mathcal{V}_{\gamma s\,\beta s}^{q\mu\,\alpha s}(\mathbf{A},\mathbf{B},\mathbf{C}) = \frac{2^{5/4}\gamma^{3/4}\alpha^{3/4}\beta^{3/4}}{V_{\rm OL}^{1/2}\pi^{17/4}} \int \frac{d^3p}{p^2+\mu^2} \int d^3r\, e^{i(\mathbf{p}-\mathbf{q})\cdot\mathbf{r}}\, e^{-\alpha|\mathbf{r}-\mathbf{A}|^2} \times \int d^3r'\, e^{-\gamma|\mathbf{r}'-\mathbf{C}|^2}\, e^{-\beta|\mathbf{r}'-\mathbf{B}|^2}\, e^{-i\mathbf{p}\cdot\mathbf{r}'}. \quad (A.6)$$

Here, we can calculate separately the one-electron integrals

$$\begin{aligned} \langle \gamma s_{\mathbf{C}}|\, e^{-i\mathbf{p}\cdot\hat{\mathbf{r}}}\, |\beta s_{\mathbf{B}}\rangle &= \left(\frac{2}{\pi}\right)^{3/2} \gamma^{3/4}\beta^{3/4} \int d^3r\, e^{-\gamma|\mathbf{r}-\mathbf{C}|^2}\, e^{-\beta|\mathbf{r}-\mathbf{B}|^2}\, e^{-i\mathbf{p}\cdot\mathbf{r}} \\ &= \frac{2^{3/2}\beta^{3/4}\gamma^{3/4}}{(\beta+\gamma)^{3/2}} e^{-\frac{p^2}{4(\beta+\gamma)}} e^{-\frac{\beta\gamma}{\beta+\gamma}|\mathbf{B}-\mathbf{C}|^2} e^{-i\mathbf{p}\cdot\frac{\beta\mathbf{B}+\gamma\mathbf{C}}{\beta+\gamma}} \quad (A.7) \end{aligned}$$

and

$$\begin{aligned} \langle \mathbf{q}|e^{i\mathbf{p}\cdot\hat{\mathbf{r}}}\, |\alpha s_{\mathbf{A}}\rangle &= \frac{\alpha^{3/4}}{V_{\rm OL}^{1/2}} \left(\frac{2}{\pi}\right)^{3/4} \int d^3r\, e^{i(\mathbf{p}-\mathbf{q})\cdot\mathbf{r}}\, e^{-\alpha|\mathbf{r}-\mathbf{A}|^2} \quad (A.8) \\ &= \left(\frac{2\pi}{\alpha}\right)^{3/4} e^{-\frac{|\mathbf{p}-\mathbf{q}|^2}{4\alpha}} \frac{e^{i\mathbf{A}\cdot(\mathbf{p}-\mathbf{q})}}{V_{\rm OL}^{1/2}}, \quad (A.9) \end{aligned}$$

while we still need to perform the **p**-integral:

$$\mathcal{V}_{\gamma s\,\beta s}^{q\mu\,\alpha s}(\mathbf{A},\mathbf{B},\mathbf{C}) = \int \frac{d^3p}{2\pi^2} \frac{\langle \gamma s_{\mathbf{C}}|\, e^{-i\mathbf{p}\cdot\hat{\mathbf{r}}}\, |\beta s_{\mathbf{B}}\rangle\, \langle \mathbf{q}|e^{i\mathbf{p}\cdot\hat{\mathbf{r}}}\, |\alpha s_{\mathbf{A}}\rangle}{p^2+\mu^2}. \quad (A.10)$$

By (A.7) and (A.9), this last relation can be put in the form

$$\mathcal{V}_{\gamma s\,\beta s}^{q\mu\,\alpha s}(\mathbf{A},\mathbf{B},\mathbf{C}) = \mathcal{V}_0 e^{-\frac{\beta\gamma}{\beta+\gamma}|\mathbf{B}-\mathbf{C}|^2 - \frac{q^2}{4\alpha} - i\mathbf{q}\cdot\mathbf{A}} \int \frac{d^3p}{p^2+\mu^2} e^{-\xi\, p^2 - \mathbf{Z}\cdot\mathbf{p}}, \quad (A.11)$$

where we have introduced the following parameters:

$$\mathcal{V}_0 = \frac{2^{5/4}\beta^{3/4}\gamma^{3/4}}{\pi^{5/4}\alpha^{3/4}V_{\rm OL}^{1/2}(\beta+\gamma)^{3/2}}, \quad \xi = \frac{\alpha+\beta+\gamma}{4\alpha\,(\beta+\gamma)}, \quad \mathbf{W} = \mathbf{A} - \frac{\beta\mathbf{B}+\gamma\mathbf{C}}{\beta+\gamma} - \frac{i\mathbf{q}}{2\alpha}. \quad (A.12)$$

The integral (A.11) can be determined by using the following "trick": we introduce the auxiliary function:

$$f_{\rm INT}(\epsilon,\mu) = \mathcal{V}_0\, e^{-\frac{\beta\gamma}{\beta+\gamma}|\mathbf{B}-\mathbf{C}|^2 - \frac{q^2}{4\alpha} - i\mathbf{q}\cdot\mathbf{A}} \int d^3p\, e^{-\xi\, p^2 - \mathbf{W}\cdot\mathbf{p}} \frac{e^{-\epsilon\left(p^2+\mu^2\right)}}{p^2+\mu^2}, \quad (A.13)$$

satisfying $f_{\rm INT}(0) = \mathcal{V}_{\gamma s\,\beta s}^{q\mu\,\alpha s}$ and $f_{\rm INT}(\infty) = 0$, and we write:

$$\mathcal{V}_{\gamma s\,\beta s}^{q\mu\,\alpha s}(\mathbf{A},\mathbf{B},\mathbf{C}) = f_{\rm INT}(0,\mu) - f_{\rm INT}(\infty,\mu) = -\int_0^\infty d\epsilon \frac{d}{d\epsilon} f_{\rm INT}(\epsilon,\mu), \tag{A.14}$$

where

$$\begin{aligned}\frac{d}{d\epsilon} f_{\rm INT}(\epsilon,\mu) &= \mathcal{V}_0\, e^{-\frac{\beta\gamma}{\beta+\gamma}|\mathbf{B}-\mathbf{C}|^2 - \frac{q^2}{4\alpha} - i\mathbf{q}\cdot\mathbf{A}} \int d^3p\, e^{-\xi\, p^2 - \mathbf{W}\cdot\mathbf{p}} \\ &= \mathcal{V}_0\, e^{-\frac{\beta\gamma}{\beta+\gamma}|\mathbf{B}-\mathbf{C}|^2 - \frac{q^2}{4\alpha} - i\mathbf{q}\cdot\mathbf{A}} \frac{\pi^{3/2} e^{-\epsilon\mu^2}}{(\xi+\epsilon)^{3/2}} e^{\frac{W_x^2+W_y^2+W_z^2}{4(\xi+\epsilon)}}\end{aligned} \tag{A.15}$$

Now, the integral (A.14) can be evaluated analytically in the $\mu \to 0$ limit, yielding the final result:

$$\mathcal{V}_{\gamma s\,\beta s}^{q\,\alpha s}(\mathbf{A},\mathbf{B},\mathbf{C}) = \frac{2\,\mathcal{V}_0\,\pi^2}{i\sqrt{W_x^2+W_y^2+W_z^2}}\, e^{-\frac{\beta\gamma}{\beta+\gamma}|\mathbf{B}-\mathbf{C}|^2 - \frac{q^2}{4\alpha} - i\mathbf{q}\cdot\mathbf{A}} \mathrm{erf}\left(\frac{i\sqrt{W_x^2+W_y^2+W_z^2}}{2\sqrt{\xi}}\right), \tag{A.16}$$

where erf is the error function. In its form (A.16), the partial integral $\mathcal{V}_{\gamma s\,\beta s}^{q\,\alpha s}$ is very useful because it allows us to calculate any other partial integrals, in particular those involving p-type Gaussians, without repeating the above outlined procedure. Indeed, Eqs. (A.2) and (A.3) lead to the connection between p_i and s Gaussian functions:

$$\psi_{\zeta\, p_i}(\mathbf{r},\mathbf{R}) = \frac{1}{\sqrt{\zeta}} \frac{\partial}{\partial R_i} \psi_{\zeta\, s}(\mathbf{r},\mathbf{R}) \tag{A.17}$$

that allow us to define all possible partial integrals involving p states by differentiation of (A.16). For example, we have

$$\mathcal{V}_{\gamma s\,\beta p_x}^{q\mu\,\alpha s}(\mathbf{A},\mathbf{B},\mathbf{C}) = \frac{1}{\sqrt{\beta}} \frac{\partial}{\partial B_x} \mathcal{V}_{\gamma s\,\beta s}^{q\,\alpha s}(\mathbf{A},\mathbf{B},\mathbf{C}), \tag{A.18}$$

or

$$\mathcal{V}_{\gamma s\,\beta p_x}^{q\mu\,\alpha p_z}(\mathbf{A},\mathbf{B},\mathbf{C}) = \frac{1}{\sqrt{\beta\alpha}} \frac{\partial^2}{\partial B_x \partial A_z} \mathcal{V}_{\gamma s\,\beta s}^{q\,\alpha s}(\mathbf{A},\mathbf{B},\mathbf{C}), \tag{A.19}$$

On site integrals are straightforwardly obtained by letting $\mathbf{A} = \mathbf{B} = \mathbf{C}$.

A.2 Spherically symmetric basis functions

We let the core-hole be created at $\mathbf{S} = \mathbf{0}$, and work within the on-site approximation. Due to its spherical symmetry, each localized basis function may be factored as the product of a radial part and an angular part, i.e., a Spherical Harmonic:

$$\psi_i(\mathbf{r},\mathbf{0}) = f_i(r) Y_{l_i m_i}(\Omega), \tag{A.20}$$

with l_i and m_i being usual angular momentum quantum numbers. In our case, the core wavefunction is an s function, i. e. $l_s = 0$ and $m_s = 0$, then, the on-site $\mathcal{V}_{s\,i'}^{q\,i}$-integral (A.1) in spherical coordinates becomes:

$$\begin{aligned}\mathcal{V}_{s\,i'}^{q\,i} &= \int_0^\infty dr\, r^2\, f_i(r) \int d^2\Omega\, Y_{l_i m_i}(\Omega)\; e^{-i\mathbf{q}\cdot\mathbf{r}} \\ &\quad \times \int_0^\infty dr'\, r'^2\, f_s^*(r')\, f_{i'}(r') \int \frac{d^2\Omega'}{\sqrt{4\pi}}\, Y_{l_{i'} m_{i'}}(\Omega')\, \frac{1}{|\mathbf{r}-\mathbf{r}'|}. \end{aligned} \tag{A.21}$$

Next, we use the well known partial waves expansions[1]

$$\frac{1}{|\mathbf{r}-\mathbf{r}'|} = \sum_{l'=0}^{\infty} \sum_{m'=-l'}^{l'} \frac{4\pi}{2l'+1} \frac{\min(r,r')^{l'}}{\max(r,r')^{l'+1}} Y_{l'm'}(\Omega)\, Y_{l'm'}^*(\Omega'), \tag{A.22}$$

for the Coulomb potential, and

$$e^{-i\mathbf{q}\cdot\mathbf{r}} = 4\pi \sum_{l=0}^{\infty} \sum_{m=-l}^{l} i^l\, j_l(qr)\, Y_{lm}^*(\Omega_{-\mathbf{q}})\, Y_{lm}(\Omega), \tag{A.23}$$

for the plane wave, where j_l is the spherical Bessel function of the first kind. Substituting Eqs. (A.22) and (A.23) into Eq. (A.21), we get:

$$\begin{aligned}\mathcal{V}_{s\,i'}^{q\,i} &= \sum_{l,l'=0}^{\infty} \frac{(4\pi)^2\, i^l}{2l'+1} \sum_{m=-l}^{l} \sum_{m'=-l'}^{l'} Y_{lm}^*(\Omega_{-\mathbf{q}}) \\ &\quad \times \int_0^\infty dr\, r^2\, f_i(r)\, j_l(qr) \int_0^\infty dr'\, r'^2\, f_s^*(r')\, f_{i'}(r') \frac{\min(r,r')^{l'}}{\max(r,r')^{l'+1}} \\ &\quad \times \int d^2\Omega\, Y_{l_i m_i}(\Omega)\; Y_{lm}(\Omega)\, Y_{l'm'}(\Omega) \int \frac{d^2\Omega'}{\sqrt{4\pi}}\, Y_{l'm'}^*(\Omega')\; Y_{l_{i'} m_{i'}}(\Omega'). \end{aligned} \tag{A.24}$$

Now, we take advantage of the orthogonality relations between the spherical Harmonics

$$\int d^2\Omega'\, Y_{l'm'}^*(\Omega')\; Y_{l_{i'} m_{i'}}(\Omega') = \delta_{l' l_{i'}} \delta_{m' m_{i'}} \tag{A.25}$$

and of the relation between the integral of the products of three spherical harmonics and the Wigner 3-J symbol[2]

$$\int d^2\Omega\, Y_{l_i m_i}(\Omega)\; Y_{lm}(\Omega)\, Y_{l'm'}(\Omega) = \sqrt{\frac{(2l_i+1)(2l+1)(2l'+1)}{4\pi}} \begin{pmatrix} l_i & l & l' \\ 0 & 0 & 0 \end{pmatrix} \begin{pmatrix} l_i & l & l' \\ m_i & m & m' \end{pmatrix} \tag{A.26}$$

[1] See for instance J. D. Jackson, Classical Electrodynamics, Wiley, 1999

[2] For definition and properties of the Wigner 3-J symbol see A. Messiah, Quantum Mechanics, North Holland 1961.

to write

$$\mathcal{V}_{s\,i'}^{\mathbf{q}\,i} = 4\pi \sum_{l=0}^{\infty} i^l \sqrt{\frac{(2l_i+1)\,(2l+1)}{(2l_{i'}+1)}} \begin{pmatrix} l_i & l & l_{i'} \\ 0 & 0 & 0 \end{pmatrix} \mathrm{INT}_{ii'}\,(l,q) \times \sum_{m=-l}^{l} Y_{lm}^{*}\,(\Omega_{-\mathbf{q}}) \begin{pmatrix} l_i & l & l_{i'} \\ m_i & m & m_{i'} \end{pmatrix}. \tag{A.27}$$

Here, we used

$$\mathrm{INT}_{ii'}\,(l,q) = \int_0^{\infty} dr\, r^2\, f_i(r)\, j_l(qr) \int_0^{\infty} dr'\, r'^2\, f_s^{*}(r')\, f_{i'}(r') \frac{\min(r,r')^{l_{i'}}}{\max(r,r')^{l_{i'}+1}} \tag{A.28}$$

for the remaining double radial integral in Eq. (A.27) that can be either computed numerically or evaluated analytically, depending on the particular shape of the basis function. In both cases it is convenient to rewrite Eq. (A.28) as

$$\begin{aligned} \mathrm{INT}_{ii'}\,(l,q) = {} & \int_0^{\infty} dr'\, f_s^{*}(r')\, f_{i'}(r')\; (r')^{1-l_{i'}} \int_0^{r'} dr\, f_i(r)\, j_l(qr)\, r^{2+l_{i'}} \\ & + \int_0^{\infty} dr'\, f_s^{*}(r')\, f_{i'}(r')\; (r')^{2+l_{i'}} \int_{r'}^{\infty} dr\; f_i(r)\, j_l(qr)\, r^{1-l_{i'}}. \end{aligned} \tag{A.29}$$

We observe that the result is a function of the wavevector length q and the solid angle $\Omega_{-\mathbf{q}}$, corresponding to "emission" angles $\theta_{\mathbf{q}} = \theta_{-\mathbf{q}} + \pi$ and $\varphi_{\mathbf{q}} = \varphi_{-\mathbf{q}} - \pi$; moreover the angular dependence of the final integral is relatively simple, being a linear combination of Spherical Harmonics; this simple form allows analytical angular integration, as observed in section 3.4.2.

Bibliography

[1] R. M. Martin, *Electronic Structure: Basic Theory and Practical Methods* (Cambrige University Press, Cambridge, 2004).

[2] M. C. Payne, M. P. Teter, D. C. Allan, T. A. Arias and J. D. Joannopoulos, Rev. Mod. Phys. **64**, 1045 (1992).

[3] A. Sindona, M. Pisarra, P. Riccardi and G. Falcone, Nanosci. Nanotechnol. Lett. **in press**.

[4] E. Perfetto, M. Cini, S. Ugenti, P. Castrucci, M. Scarselli, M. De Crescenzi, F. Rosei and M. A. El Khakani, Phys. Rev. B **76**, 233408 (2007).

[5] P. Riccardi, A. Cupolillo, M. Pisarra, A. Sindona and L. S. Caputi, Appl. Phys. Lett. **97**, 221909 (2010).

[6] M. Pisarra, A. Cupolillo, L. S. Caputi, A. Sindona and P. Riccardi, J. Nanosci. Nanotechnol. **11**, 9256 (2011).

[7] M. Pisarra, A. Cupolillo, P. Riccardi, A. Sindona and L. S. Caputi, Nanosci. Nanotechnol. Lett. **in press**.

[8] P. Riccardi, A. Cupolillo, M. Pisarra, A. Sindona and L. S. Caputi, Appl. Phys. Lett. **in press**.

[9] F. Maeda, T. Takahashi, H. Ohsawa, S. Suzuki and H. Suematsu, Phys. Rev. B **37**, 4482 (1988).

[10] S. K. Mahatha, K. S. R. Menon and T. Balasubramanian, Phys. Rev. B **84**, 113106 (2011).

[11] A. Hoffman, G. L. Nyberg and S. Prawer, J. Phys.: Condens. Matter **2**, 8099 (2000).

[12] K. S. Novoselov, A. Geim, S. V. Morozov, D. Jiang, Y. Zhang, S. V. Dubonos, I. V. Grigorieva and A. A. Firsov, Science **306**, 666 (2004).

[13] A. H. Castro Neto, F. Guinea, N. M. R. Peres, K. S. Novoselov and A. K. Geim, Rev. Mod. Phys. **81**, 109 (2009).

[14] R. Saito, M. S. Dresselhaus and G. Dresselhaus, *Physical Properties of Carbon Nanotubes* (Imperial College Press, London, 1998).

[15] J. Wintterlin and M.-L. Bocquet, Surface Science **603**, 1841 (2009).

[16] A. Varykhalov, J. Sánchez-Barriga, A. M. Shikin, C. Biswas, E. Vescovo, A. Rybkin, D. Marchenko and O. Rader, Phys. Rev. Lett. **101**, 157601 (2008).

[17] G. Bertoni, L. Calmels, A. Altibelli and V. Serin, Phys. Rev. B **71**, 075402 (2004).

[18] M. Fuentes-Cabrera, M. I. Baskes, A. V. Melechko and M. L. Simpson, Phys. Rev. B **77**, 035405 (2008).

[19] M. S. Dresselhaus, G. Dresselhaus and P. Avouris, *Carbon Nanotubes: Synthesis, Structure, Properties, and Applications* (Springer, Berlin, 2001).

[20] M. Born and J. R. Oppenheimer, Annalen der Physik **389**, 2582 (1927).

[21] L. H. Thomas, Proc. Cambridge Phil. Soc **23**, 542 (1927).

[22] E. Fermi, Rend. Accad. Naz. Lincei **6**, 602 (1927).

[23] P. A. M. Dirac, Proc. Cambridge Phil. Roy. Soc. **26**, 376 (1930).

[24] P. Hohenberg and W. Kohn, Phys. Rev. **136**, B864 (1964).

[25] W. Kohn and L. J. Sham, Phys. Rev. **140**, A1133 (1965).

[26] B. H. Bransden and C. J. Joachain, *Physics of atoms and molecules*, Second ed. (Prentice Hall, Harlow, 1983).

[27] L. Hedin and B. I. Lundqvist, J. Phys. C: Solid State Phys. **4**, 2064 (1971).

[28] J. P. Perdew and A. Zunger, Phys. Rev. B **23**, 5048 (1981).

[29] S. Vosko, L. Wilk and M. Nusair, Can. J. Phys. **58**, 1200 (1983).

[30] D. M. Ceperley and B. J. Alder, Phys. Rev. Lett. **45**, 566 (1980).

[31] J. P. Perdew and K. Burke, Int. J. Quant. Chem. **57**, 309 (1996).

[32] O. Gunnarsson, M. Jonson and B. I. Lundqvist, Phys. Rev. B **20**, 3136 (1979).

[33] V. I. Anisimov, F. Aryasetiawan and A. I. Lichtenstein, J. Phys.:Condensed Matter **9**, 767 (1997).

[34] A. D. Becke, J. Chem. Phys. **98(2)**, 1372 (1993).

[35] N. W. Ashcroft and N. D. Mermin, *Solid State Physics* (Hault Saunders, Philadelphia, 1976).

[36] H. J. Monkhorst and J. D. Pack, Phys. Rev. B **13**, 5188 (1976).

[37] G. B. Bachelet, D. R. Hamann and M. Schlüter, Phys. Rev. B **26**, 4199 (1982).

[38] D. Vanderbilt, Phys. Rev. B **41**, 7892 (1990).

[39] J. C. Slater, Phys. Rev. **36**, 57 (1930).

[40] S. F. Boys, Proc. Roy. Soc. London, series A **200**, 542 (1950).

[41] J. M. Soler, E. Artacho, J. Gale, A. Garcia, J. Junquera, P. Ordejon and D. Sanchez-Portal, J. Phys.: Condens. Matter **14**, 2745 (2002).

[42] J. J. Sakurai, *Modern Quantum Mechanics* (Addison-Wesley, Reading, 1994).

[43] A. L. Fetter and J. D. Walecka, *Quantum Theory of Many Particle System* (McGraw-Hill, New York, 1971).

[44] G. D. Mahan, *Many-particle physics* (Plenum Press, New York, 1981).

[45] A. Sindona, M. Pisarra, S. Maletta, M. Commisso, P. Riccardi, A. Bonanno, P. Barone and G. Falcone, J. Nanosci. Nanotechnol. **11**, 9143 (2011).

[46] A. Sindona, M. Pisarra, P. Riccardi and G. Falcone, Nanosci. Nanotechnol. Lett. **3**, 835 (2011).

[47] M. W. Schmidt *et al.*, Journal of Computational Chemistry **14**, 1347 (1993).

[48] E. B. S. Library, http://bse.pnl.gov/bse/portal.

[49] J. P. Perdew, K. Burke and M. Ernzerhof, Phys. Rev. Lett. **77**, 3865 (1996).

[50] C. Heske, R. Treusch, F. J. Himpsel, S. Kakar, L. J. Terminello, H. J. Weyer and E. L. Shirley, Phys. Rev. B **59**, 4680 (1999).

[51] T. Ohta, A. Bostwick, J. L. McChesney, T. Seyller, K. Horn and E. Rotenberg, Phys. Rev. Lett. **98**, 206802 (2007).

[52] W. Zhang, Z. Xi, G. Zhang, S. Wang, M. Wang, J. Wang and Z. Xue, Applied Physics A **86**, 171 (2007).

[53] A. Rochefort, D. R. Salahub and P. Avouris, J. Phys. Chem. B **103**, 641 (1999).

[54] N. Troullier and J. L. Martins, Phys. Rev. B **43**, 1993 (1991).

[55] G. D. Mahan, Phys. Rev. **163**, 612 (1967).

[56] P. Nozières and C. T. De Dominicis, Phys. Rev. **178**, 1097 (1969).

[57] A. Sindona, R. A. Baragiola, G. Falcone, A. Oliva and P. Riccardi, Phys. Rev. A **71**, 052903 (2005).

[58] A. Sindona, S. A. Rudi, S. Maletta, R. A. Baragiola, G. Falcone and P. Riccardi, Surf. Sci. **601**, 1205 (2007).

[59] A. Sindona, F. Plastina, A. Cupolillo, C. Giallombardo, G. Falcone and L. Papagno, Surf. Sci. **601**, 2805 (2007).

[60] J. E. Houston, J. W. Rogers, R. R. Rye, F. L. Hutson and D. E. Ramaker, Phys. Rev. B **34**, 1215 (1986).

[61] M. Cini, Solid State Comm **20**, 605 (1976).

[62] M. Cini, Solid State Comm **24**, 681 (1976).

[63] E. J. Mele and J. J. Ritsko, Phys. Rev. Lett. **43**, 68 (1979).

[64] R. D. Kelley and D. W. Goodman.

[65] Y. S. Dedkov, M. Fonin and C. Laubschat, Appl. Phys. Lett. **92**, 052506 (2006).

[66] A. Nagashima, N. Tejima and C. Oshima, Phys. Rev. B **50**, 17487 (1994).

[67] J. J. Lawton, A. Pulischiano and R. E. Palmer, J. Phys.: Condens. Matter **21**, 474206 (2009).

[68] P. E. Best, Phys. Rev. Lett. **34**, 674 (1975).

[69] L. S. Caputi, G. Chiarello, A. Santaniello, E. Colavita and L. Papagno, Phys. Rev. B **34**, 6080 (1986).

[70] J. Cazaux, Appl. Phys. Lett. **98**, 013109 (2011).

[71] P. Riccardi, M. Pisarra, A. Cupolillo, M. Commisso, A. Sindona, R. A. Baragiola and C. A. Dukes, J. Phys.: Condens. Matter **22**, 305004 (2010).

[72] H. J. Hopman and J. Verhoeven, Appl. Surf. Sci **150**, 1 (1999).

[73] R. A. Baragiola, S. M. Ritzau, R. C. Monreal, C. A. Dukes and P. Riccardi, Nucl. Instrum. Meth. B **157**, 110 (1999).

[74] S. Goedecker, M. Teter and J. Huetter, Phys. Rev. B **54**, 1703 (1996).

[75] X. Gonze, dum, dum, dum, dum, dum, dum, dum, dum and dum, Computer Phys. Commun. **180**, 2582 (2009).

[76] X. Gonze, dum, dum, dum, dum, dum, dum, dum, dum and dum, Z. Kristallogr. **220**, 558 (2005).

[77] S. Latil and L. Henrard, Phys. Rev. Lett. **97**, 036803 (2006).

[78] E. Kogan and V. U. Nazarov, Phys. Rev. B **85**, 115418 (2012).

[79] A. Bianconi, S. B. M. Hagström and R. Z. Bachrach, Phys. Rev. B **16**, 5543 (1977).

[80] A. R. Law, J. J. Barry and H. P. Hughes, Phys. Rev. B **28**, 5332 (1983).

[81] L. Papagno, L. S. Caputi, M. De Crescenzi and R. Rosei, Phys. Rev. B **26**, 2320 (1982).

[82] R. Claessen, H. Carstensen and M. Skibowski, Phys. Rev. B **38**, 12582 (1988).

[83] I. Schäfer, M. Schlüter and M. Skibowski, Phys. Rev. B **35**, 7663 (1987).

[84] V. N. Strocov, P. Blaha, H. I. Starnberg, M. Rohlfing, R. Claessen, J. M. Debever and J. M. Themlin, Phys. Rev. B **61**, 4994 (2000).

[85] S. Tatar, R. C.and Rabii, Phys. Rev. B **25**, 4126 (1981).

[86] H. Hibino, H. Kageshima, F.-Z. Guo, F. Maeda, M. Kotsugi and Y. Watanabe, Appl. Surf. Sci. **254**, 7596 (2008).

[87] D. Pines and P. Nozieres, *The Theory of Quantum Liquids* (Addison-Wesley, New York, 1989).

[88] J. M. Pitarke, V. M. Silkin, E. V. Chulkov and P. M. Echenique, rep. Prog. Phys. **70**, 1 (2007).

[89] G. Giovannetti, P. A. Khomyakov, G. Brocks, V. M. Karpan, J. van den Brink and P. J. Kelly, Phys. Rev. Lett. **101**, 026803 (2008).

[90] J. L. McChesney, A. Bostwick, T. Ohta, T. Seyller, K. Horn, J. González and E. Rotenberg, Phys. Rev. Lett. **104**, 136803 (2010).

[91] J.-H. Chen, M. Ishigami, C. Jang, D. R. Hines, M. S. Fuhrer and E. D. Williams, Adv. Mater. **19**, 3623 (2007).

[92] T. Langer, D. F. Förster, C. Busse, T. Michely, H. Pfnür and C. Tegenkamp, New J. Phys **13**, 053006 (2011).

[93] A. Politano, A. R. Marino, V. Formoso, D. Farías, R. Miranda and G. Chiarello, Phys. Rev. B **84**, 033401 (2011).

[94] C. Tegenkamp, H. Pfnür, T. Langer, J. Baringhaus and H. W. Schumacher, J. Phys: Condens Matter **23**, 012001 (2011).

[95] Y. Liu, R. F. Willis, K. V. Emtsev and T. Seyller, Phys. Rev. B **78**, 201403 (2008).

[96] S. Y. Shin, C. G. Hwang, S. J. Sung, N. D. Kim, H. S. Kim and J. W. Chung, Phys. Rev. B **83**, 161403 (2011).

[97] K. W. K. Shung, Phys. Rev. B **34**, 979 (1986).

[98] E. H. Hwang and S. Das Sarma, Phys. Rev. B **75**, 205418 (2007).

[99] B. Wunsch, T. Stauber, F. Sols and F. Guinea, New J. Phys. **8**, 318 (206).

[100] A. Generalov and Y. Dedkov, Carbon **50**, 183 (2012).

[101] A. Cupolillo, N. Ligato and L. Caputi, Carbon **50**, 2588 (2012).

[102] H. Bruus and K. Flensberg, *Many-Body Quantum Theory in Condensed Matter Physics: An Introduction* (Oxford University Press, Oxford, 2004).

[103] W. Nolting, *Foundamentals of Many-Body Physics* (Springer-Verlag, 2009).

[104] M. A. Morrison, T. L. Estle and N. F. Lane, *Quantum States of atoms, molecules, and solids* (Prentice-Hall, Englewood Cliffs, 1976).

[105] J. Lindhard, K. Dan. Vidensk. Selsk. Mat.-Fis. Medd. **28**, 8 (1954).

[106] A. Zangwill and P. Soven, Phys. Rev. A **21**, 1561 (1980).

[107] L. Reining, V. Olevano, A. Rubio and G. Onida, Phys. Rev. Lett. **88**, 066404 (2002).

[108] S. L. Adler, Phys. Rev. **126**, 413 (1962).

[109] N. Wiser, Phys. Rev. **129**, 62 (1963).

[110] E. A. Taft and H. R. Philipp, Phys. Rev. **138**, A197 (1965).

[111] V. N. Kotov, B. Uchoa, V. M. Pereira, F. Guinea and A. H. Castro Neto, Rev. Mod. Phys. **84**, 1067 (2012).

[112] C. Kramberger *et al.*, Phys. Rev. Lett. **100**, 196803 (2008).

[113] M. K. Kinyanjui, C. Kramberger, T. Pichler, J. C. Meyer, P. Wachsmuth, G. Benner and U. Kaiser, EPL **97**, 57005 (2012).

[114] J. Yan, K. S. Thygesen and K. W. Jacobsen, Phys. Rev. Lett. **106**, 146803 (2011).

[115] T. Ando, A. B. Fowler and F. Stern, Rev. Mod. Phys. **54**, 437 (1982).